DISCLAIMER

This report was prepared as an account of work sponsored by an agency of the United States Government. Neither the United States Government nor any agency thereof, nor any of their employees, makes any warranty, express or implied, or assumes any legal liability or responsibility for the accuracy, completeness, or usefulness of any information, apparatus, product, or process disclosed, or represents that its use would not infringe privately owned rights. Reference herein to any specific commercial product, process, or service by trade name, trademark, manufacturer, or otherwise does not necessarily constitute or imply its endorsement, recommendation, or favoring by the United States Government or any agency thereof. The views and opinions of authors expressed herein do not necessarily state or reflect those of the United States Government or any agency thereof. Reference herein to any social initiative (including but not limited to Diversity, Equity, and Inclusion (DEI); Community Benefits Plans (CBP); Justice 40; etc.) is made by the Author independent of any current requirement by the United States Government and does not constitute or imply endorsement, recommendation, or support by the United States Government or any agency thereof.

ANL/NSE-22/17 Rev. 2

Argonne NATIONAL LABORATORY

SAS4A/SASSYS-1 Validation with FFTF Tests

Nuclear Science and Engineering Division

ANL/NSE-22/17 Rev. 2

SAS4A/SASSYS-1 Validation with FFTF Tests

prepared by
R. Thomas, T. Sumner, and A. Moisseytsev
Nuclear Science and Engineering Division, Argonne National Laboratory

April 30, 2025

ABSTRACT

The FFTF liquid sodium cooled test reactor was built to assist the development and testing of advanced fuels and material for fast reactors. The goals of the FFTF Passive Safety Testing program included confirming the safety margins of FFTF as a liquid metal reactor, providing data for computer code validation, and demonstrating the inherent and passive safety benefits of its specific design features. The program included thirteen unprotected loss of flow without scram tests. In preparation for the Passive Safety Testing program, a series of individual reactivity feedback tests were performed which were designed to simulate and validate specific features and reactivity feedbacks of the FFTF core.

The results of modeling and simulation of LOFWOS Tests #10, #11, and #12, and a selection of individual reactivity feedback tests are presented in this report to support validation of Argonne's SAS4A/SASSYS-1 fast reactor safety analysis code. The three LOFWOS tests did not use the primary loop pony motors and thus transitioned to natural circulation flow rates from varying initial power levels. This validation activity leverages modeling and simulation efforts that originated under an International Atomic Energy Agency Coordinated Research Project (CRP) for benchmark analysis of the FFTF LOFWOS Test #13. The SAS4A/SASSYS-1 model originally developed for the CRP has been extended to include LOFWOS Tests #10-12 and the individual reactivity feedback tests. The model has also been modernized to utilize new code features and modeling practices.

Predicted results from SAS4A/SASSYS-1 were compared to measured test data and differences were investigated. Overall, it was concluded that, for LOFWOS Tests #10-12, there was good agreement between the flow, power, and temperature predictions and the measured data. For the individual reactivity feedback tests, there was good agreement between net reactivity predictions and the measured data.

TABLE OF CONTENTS

LIST OF FIGURES

LIST OF TABLES

1 Introduction

The Fast Flux Test Facility (FFTF) at the Hanford site in Washington was designed by Westinghouse Electric Corporation for the U.S. Department of Energy. FFTF was a 400 MW-thermal oxide-fueled liquid sodium cooled test reactor built to assist the development and testing of advanced fuels and material for fast reactors. The reactor did not generate electricity, instead discharging heat to the atmosphere via air-cooled dump heat exchangers (DHX). After reaching criticality in 1980, FFTF operated until 1992, providing the means to test fuels, materials, and other components in a high fast neutron flux environment [1].

In July 1986, a series of unprotected transients were performed in FFTF as part of the Passive Safety Testing program. Among these were thirteen unprotected (with the plant protection system intentionally disabled) loss of flow without scram (LOFWOS) tests, which were performed during Cycle 8C. The different tests were initiated at varying power levels ranging from 10%-50% of the nominal full power level. The first set of tests used the primary loop pony motors to maintain flow rates of approximately 9% of the nominal full flow, while the second set did not, allowing the primary system to transition to natural circulation flow rates without pony motor assistance. The goals of this program included confirming the safety margins of FFTF as a liquid metal reactor, providing data for computer code validation, and demonstrating the inherent and passive safety benefits of its specific design features.

In preparation for the Passive Safety Testing program, a series of individual reactivity feedback tests were performed [2]. The primary goal of these tests was to evaluate and confirm the core reactivity feedbacks in a systematic fashion by subjecting the core to various power, flow, and core inlet temperature conditions. These tests were carried out prior to the LOFWOS tests, during Cycle 8A. Unlike the integral LOFWOS reactor tests, each step in Cycle 8A was designed to simulate and validate specific features and reactivity feedbacks of the FFTF core.

The SAS4A/SASSYS-1 design and safety analysis code is developed and maintained by Argonne National Laboratory. The code provides the capability for transient simulation of anticipated operational occurrences, design basis accidents, and beyond design basis accidents in liquid-metal cooled fast reactors. SAS4A/SASSYS-1 has unique capabilities to account for inherent fast spectrum feedback effects and passive safety features, which are key elements of the sodium-cooled fast reactor (SFR) safety basis. The software facilitates the assessment of key safety basis metrics, including margins for structural thermal limits, metallic fuel failure, sodium boiling, and fission product release [3].

The results of modeling and simulation of LOFWOS Tests #10, #11, and #12, as well as several Cycle 8A tests of each type, are presented in this report to support validation of SAS4A/SASSYS-1. The three LOFWOS tests did not use the primary loop pony motors and thus transitioned to natural circulation flow rates, and were initiated from 40%, 45%, and 50% of the nominal power level, respectively.

This validation activity leverages modeling and simulation efforts that originated under an International Atomic Energy Agency (IAEA) Coordinated Research Project (CRP) for benchmark analysis of the FFTF LOFWOS Test #13 [1]. Several Cycle 8A individual reactivity feedback tests were modeled to inform and improve the benchmark analysis of LOFWOS Test #13 [4]. In addition to being the lead technical organization for the CRP, Argonne was also a participant in the benchmark. The SAS4A/SASSYS-1 models of Cycle 8C originally developed for the CRP have been extended to include LOFWOS Tests #10-12 and additional Cycle 8A individual reactivity feedback tests. The models have also been modernized to utilize new code features and modeling practices.

2 FFTF Description

FFTF was a 400 MW-thermal loop type SFR prototype with mixed oxide fuel. Heat was removed from the reactor core by liquid sodium circulating under low pressure. Figure 2.1 [1] illustrates the reactor vessel and its major components. Sodium exited the reactor vessel into one of three primary sodium loops. Intermediate heat exchangers (IHX) separated activated sodium coolant in the primary loops from nonradioactive sodium in the secondary loops. FFTF did not generate electricity, instead rejecting all heat to the environment via twelve air dump heat exchangers (DHX). Figure 2.2 [1] illustrates the major components in each of the three coolant systems. Complete detailed information necessary for modeling FFTF is available in Reference 1. The following sub-sections provide a summary of this information.

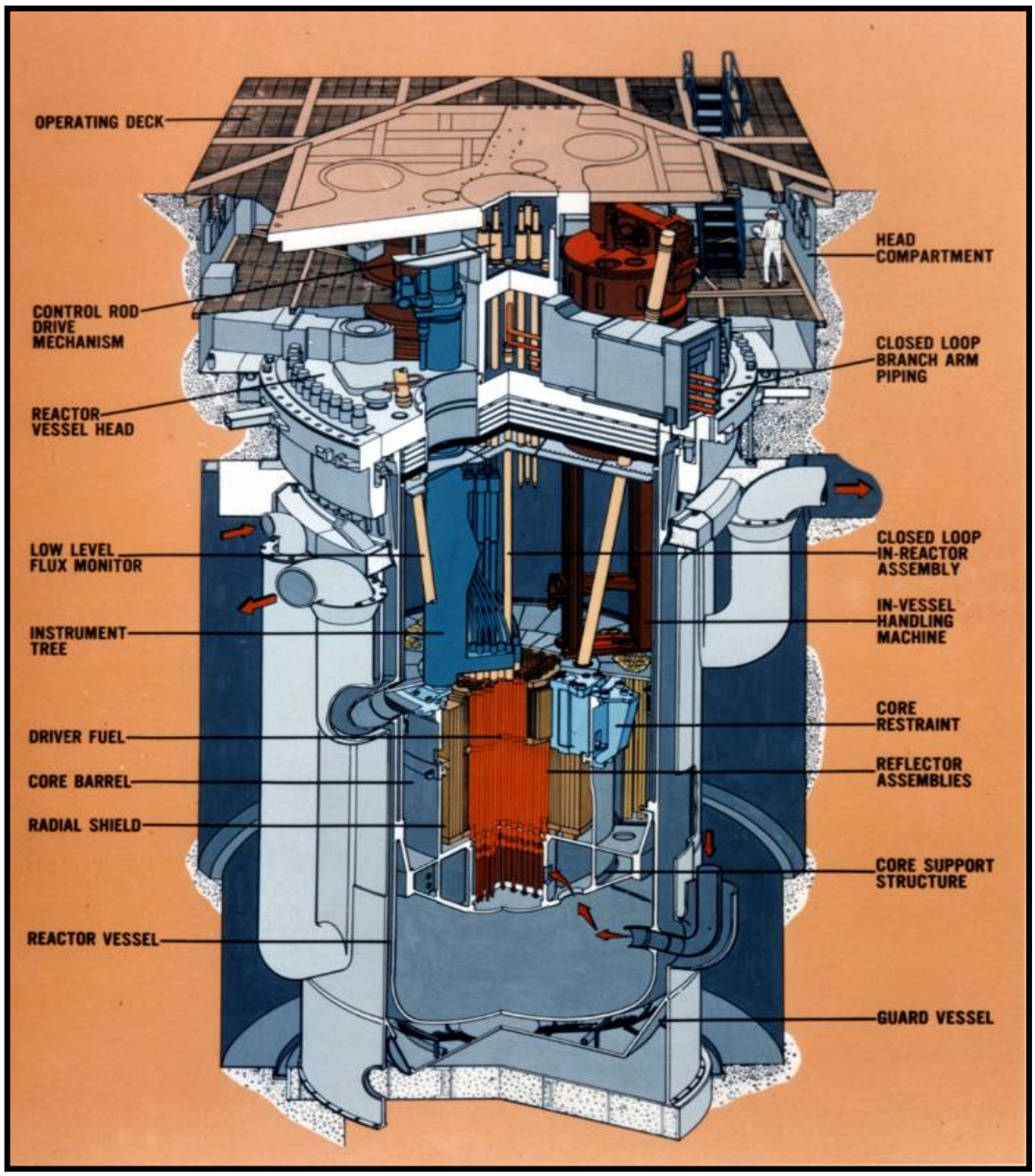

Figure 2.1. Reactor Vessel Overview [1]

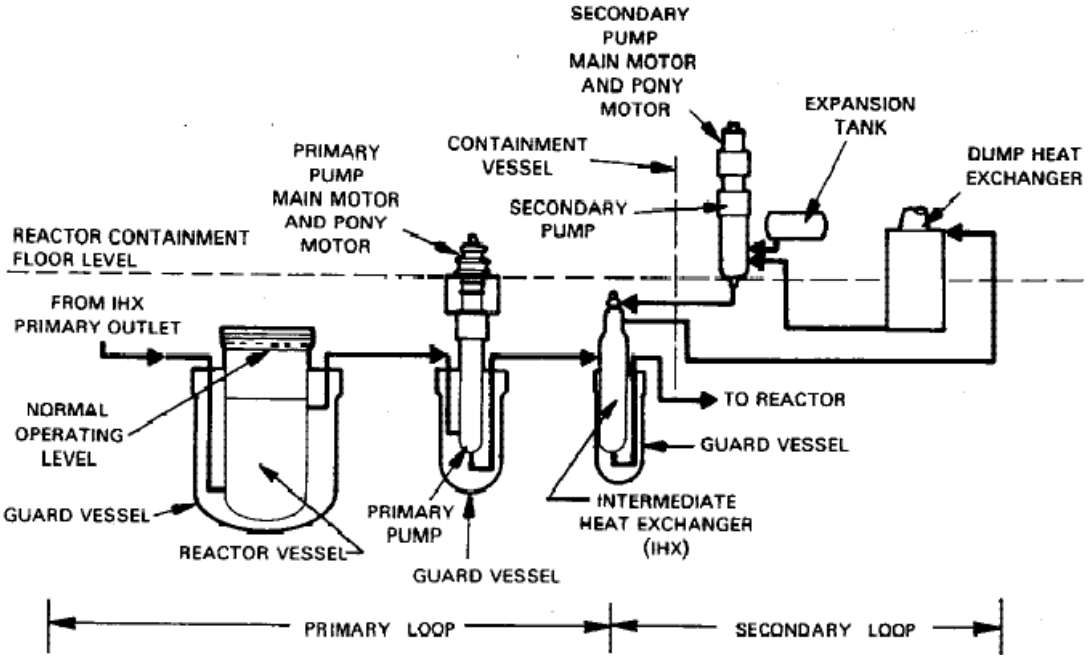

Figure 2.2. Coolant System Overview [1]

2.1 Core

The FFTF core contained 199 hexagonal assembly positions. The LOFWOS tests were performed during Cycle 8C. Figure 2.3 illustrates the Cycle 8C core loading pattern, which included 8 different types of assemblies. The individual reactivity feedback tests were performed during Cycle 8A. Figure 2.4 illustrates the Cycle 8A core loading pattern, which included 12 different types of assemblies. Assemblies labeled with red letters contain instrumentation which is discussed in more detail in Section 2.5.2. The abbreviations in the list below are consistent with labeling in Figure 2.3 and Figure 2.4:

- Driver Fuel Assemblies (DF)
    - Series 1 drivers (3.1DF and 3.2DF)
    - Series 2 drivers (4.1DF and 4.2DF)
- In Core Shim Assembly (ICSA)
- Reflector Assemblies (REFL)
- Control Rods (CR1 and CR2) and Safety Rods (SR)
- Materials Open Test Assembly (MOTA)
- Advanced Oxide Test Assemblies (ACO, FO)
- Advanced Oxide Fuel Test Assemblies (PO)
- Mixed Carbide Fuel Test Assembly (FC)
- D9 Alloy Test Assembly (D9)
- High Enrichment High Burnup Absorber Test Assembly (HEHB)
- Fracture Mechanics Assembly (FMA)
- Gas Expansion Modules (GEM)

There were several variations of driver assemblies, reflector assemblies, and control rods. The differences are summarized in Sections 2.1.1 – 2.1.3, and more detailed information is provided in Reference 1.

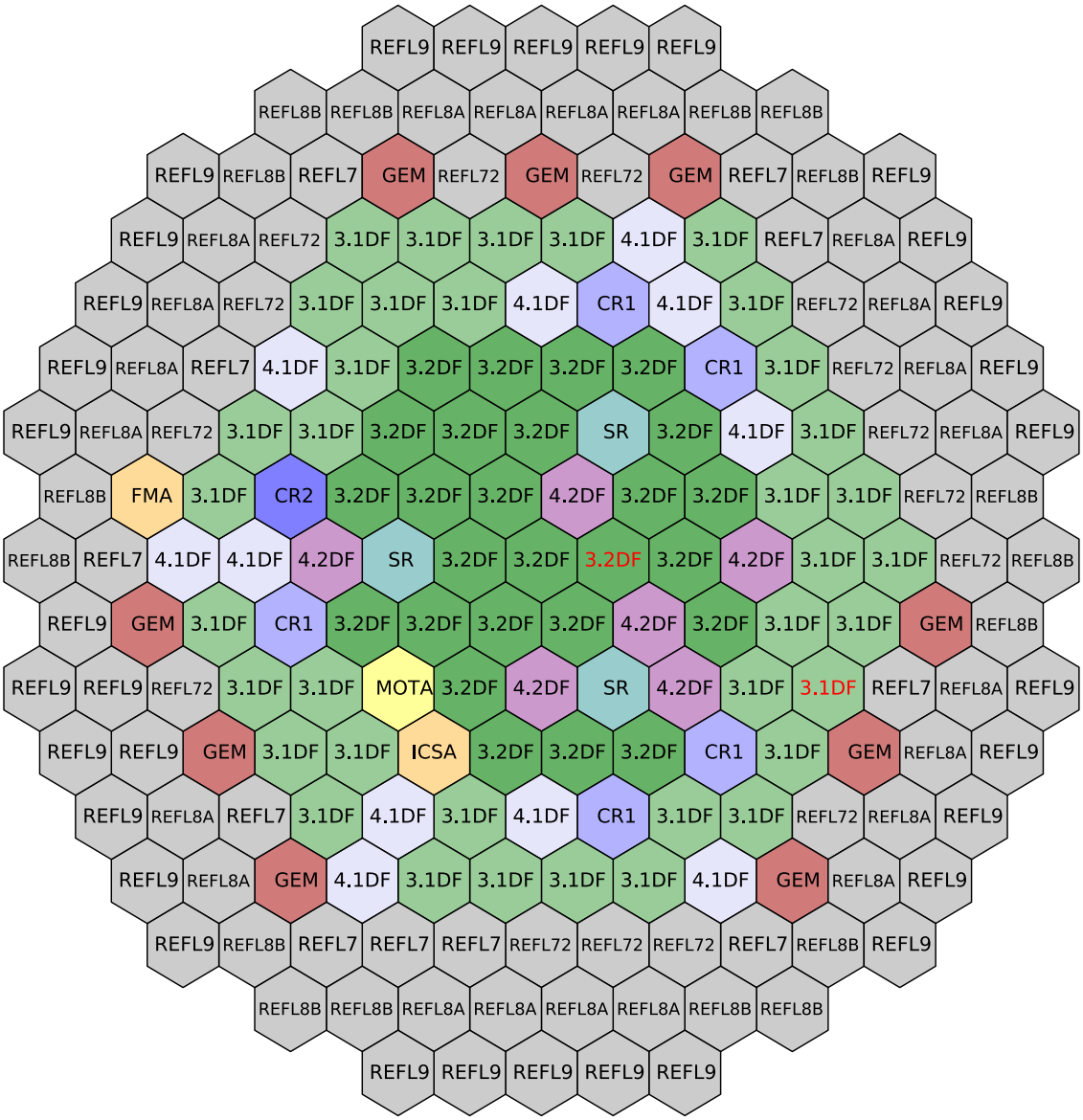

Figure 2.3. Cycle 8C Core Loading

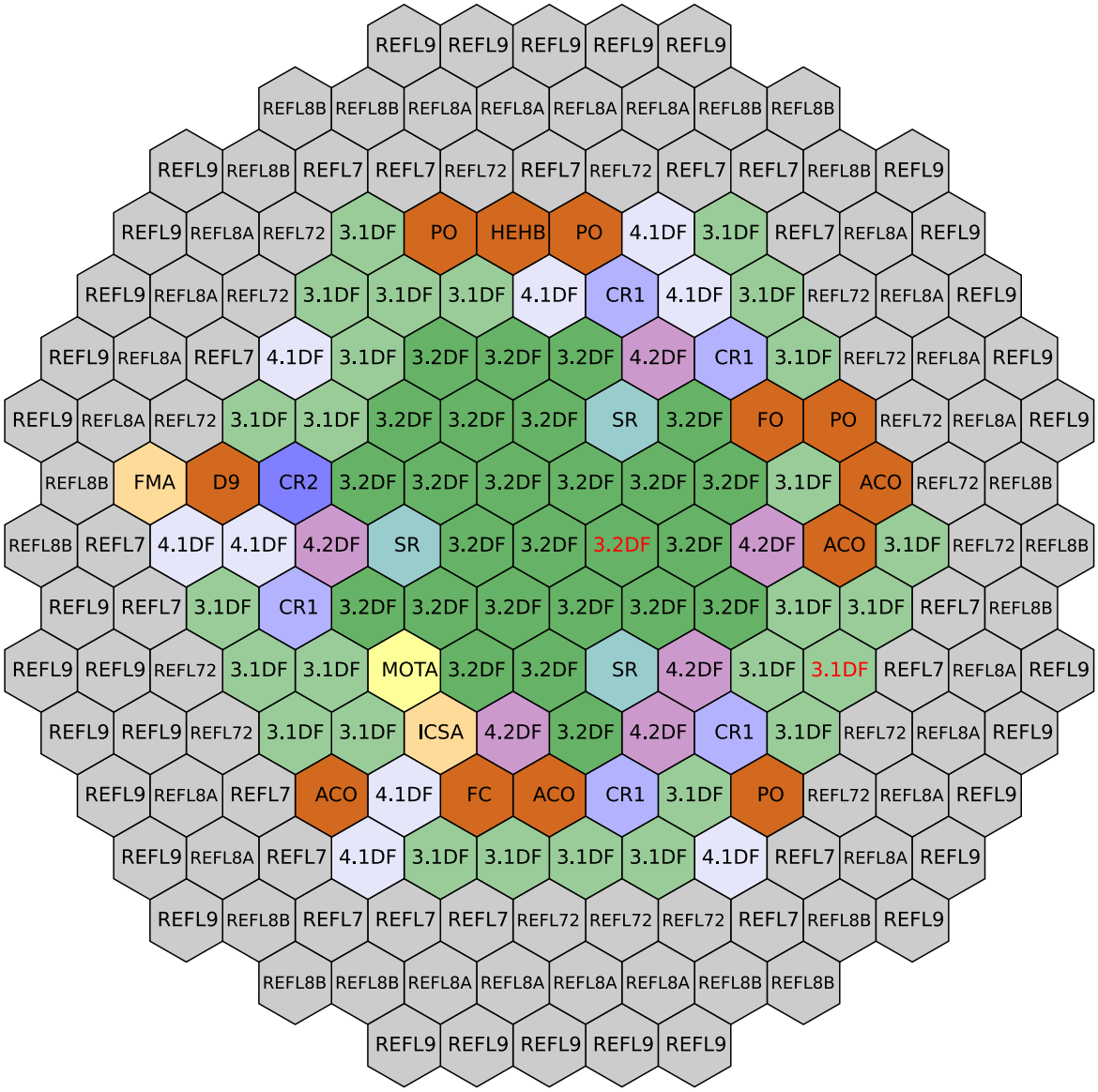

Figure 2.4. Cycle 8A Core Loading

2.1.1 Driver Fuel Assemblies

Each hexagonal driver fuel assembly consisted of an inlet nozzle, shield/orifice block, duct, load bearing pads, handling socket, and a fuel pin bundle of 217 wire-wrapped fuel pins. Figure 2.5 [1] and Figure 2.6 [1] present the internal configuration and axial dimensions of the driver fuel assembly, and Table 2.1 lists key dimensions and parameters.

One of the primary functions of the shield/orifice block was to control the sodium flow rate. This was accomplished by redirecting sodium flow through multiple channels in a series of sections. Different flow rates for Series 1 (3.1DF and 3.2DF) and Series 2 (4.1DF and 4.2DF) drivers were accomplished by using different flow hole sizes. Additional information about the different series of driver assemblies is provided in Reference 1.

Table 2.1. Driver Fuel Assembly Key Dimensions and Parameters

	Parameter	Value
Pin	Fuel Material	UO_2-PuO_2
	Pu Content (Pu/(Pu+U))	3.1DF: 27.37 wt% 3.2DF: 22.43 wt% 4.1DF: 29.28 wt% 4.2DF: 25.14 wt%
	U Specification	3.1 and 3.2 DF: Natural UO_2 4.1 and 4.2 DF: Depleted UO_2
	Fuel Outer Diameter	0.4940 cm
	Clad Material	Stainless Steel Type 316
	Clad Inner Diameter	0.5080 cm
	Clad Outer Diameter	0.5842 cm
	Pin Pitch	0.726 cm
Wire Wrap	Material	Stainless Steel Type 316
	Outer Diameter	0.1445 cm
	Pitch	30.2 cm
Assembly	Number of Pins	217
	Duct Wall Material	Stainless Steel Type 316
	Duct Wall Thickness	0.305 cm
	Duct Wall Flat-to-Flat	11.621 cm
	Assembly Pitch	12.014 cm

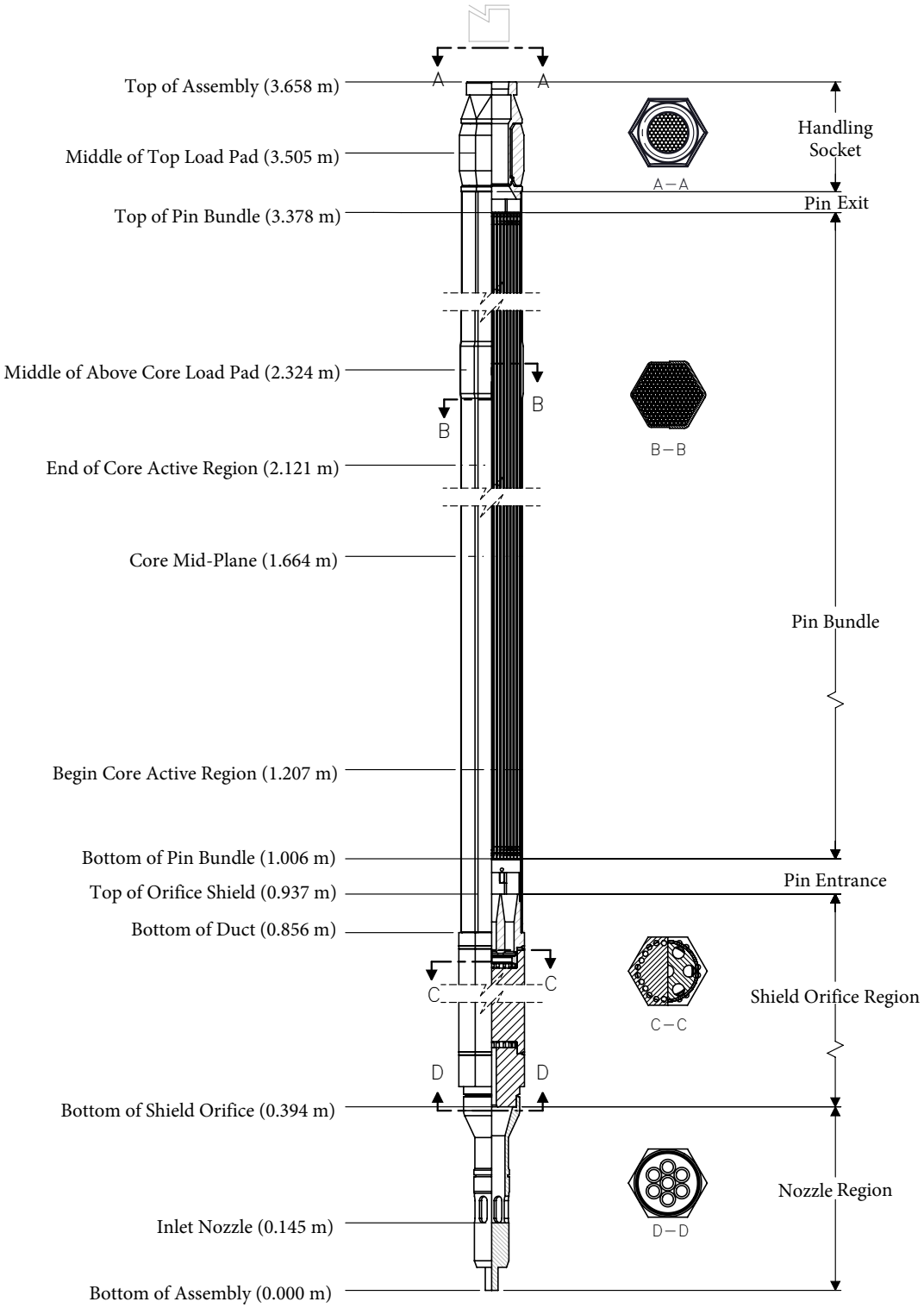

Figure 2.5. Driver Fuel Assembly [1]

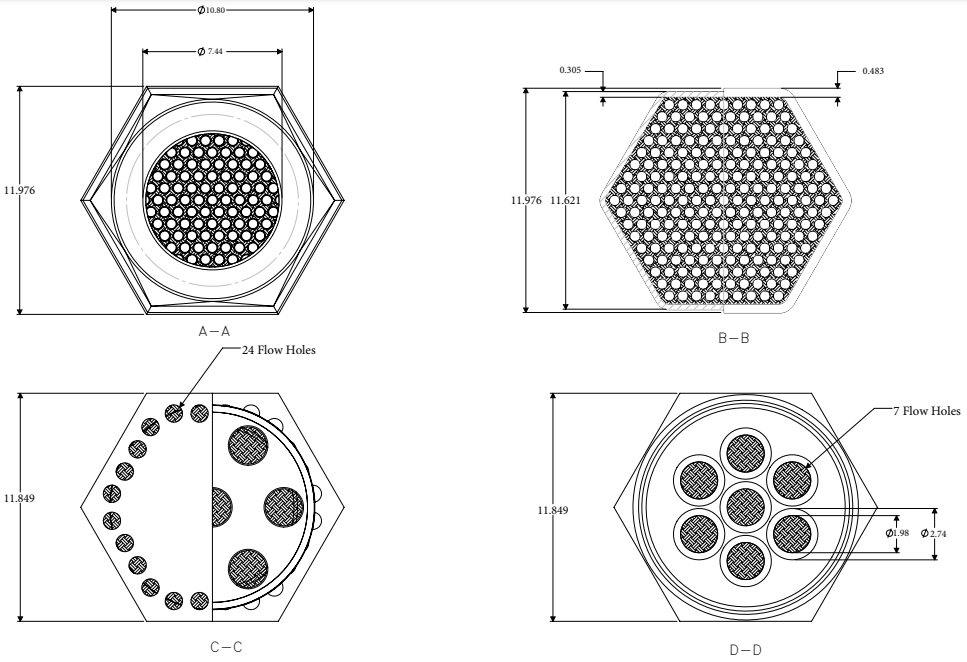

Figure 2.6. Driver Fuel Assembly Cross-Section Views (Dimensions in cm) [1]

2.1.2 Reflector Assemblies

The reflector assemblies consisted of an inlet nozzle, lower shield/orifice region, reflector section, load pads, upper shield section, and a handling socket. The reflector sections were block-type, containing a stack of hexagonal reflector blocks made of Inconel 600. The upper shield also consisted of hexagonal blocks, while the lower shield consisted of a single stainless steel block.

There were five types of reflector assemblies. Two were in Row 7 (REFL7 and REFL72), two were in Row 8 (REFL8A and REFL8B) and one was in Row 9 (REFL9). The main differences between the types of reflectors were their length and the characteristics of the flow channels through the assembly. Figure 2.7 [1] illustrates the components of the reflector assemblies. Figure 2.8 [1] shows the reflector cross section in the reflector region. Table 2.2 lists key dimensions and parameters of the different reflector assembly types. Additional information about the different types of reflector assemblies is provided in Reference 1. All five types of reflector assemblies were not explicitly modeled in the SAS4A/SASSYS-1 core model described in Section 4.1 and instead they were all treated as type REFL8A.

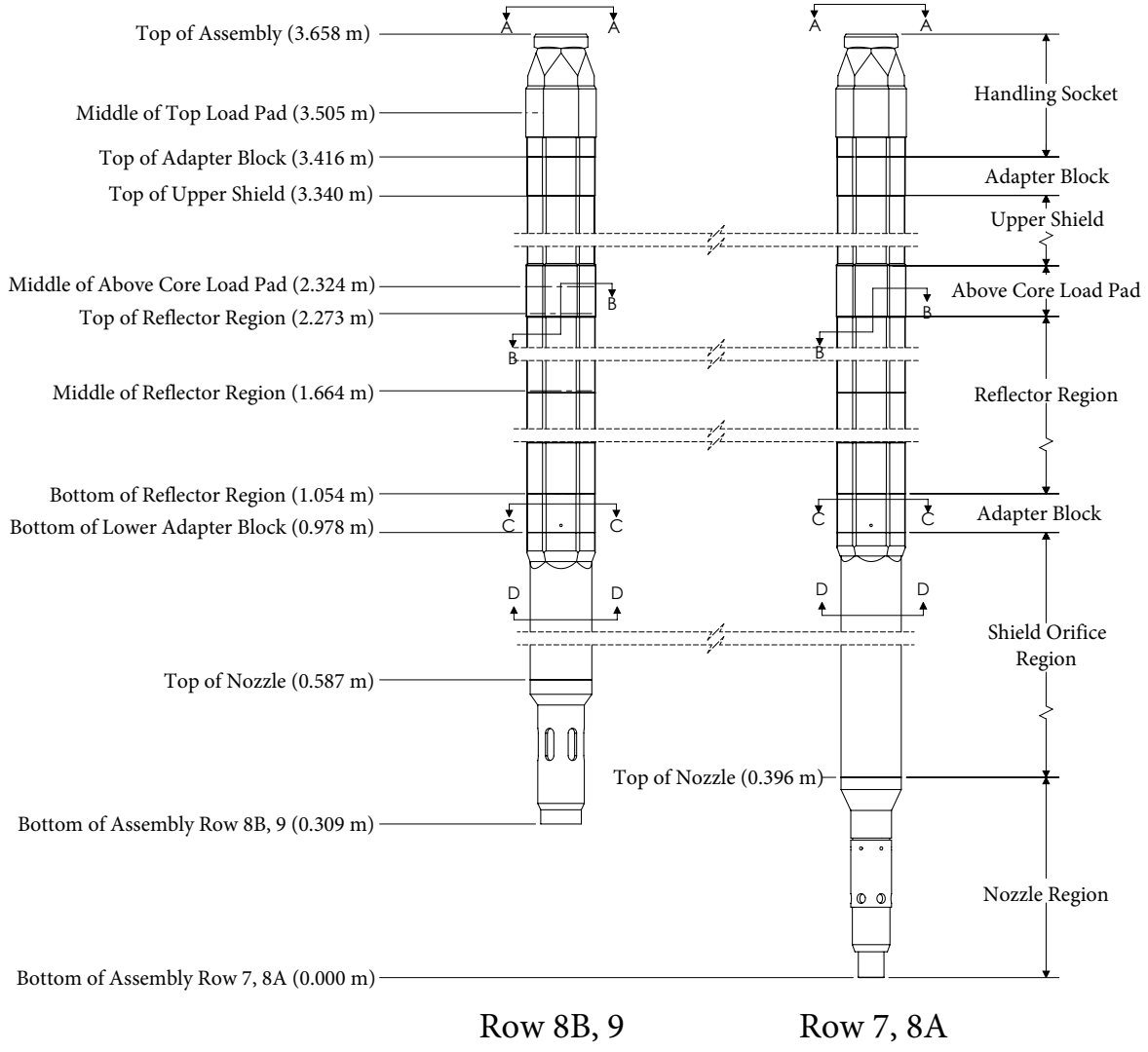

Figure 2.7. Reflector Assemblies [1]

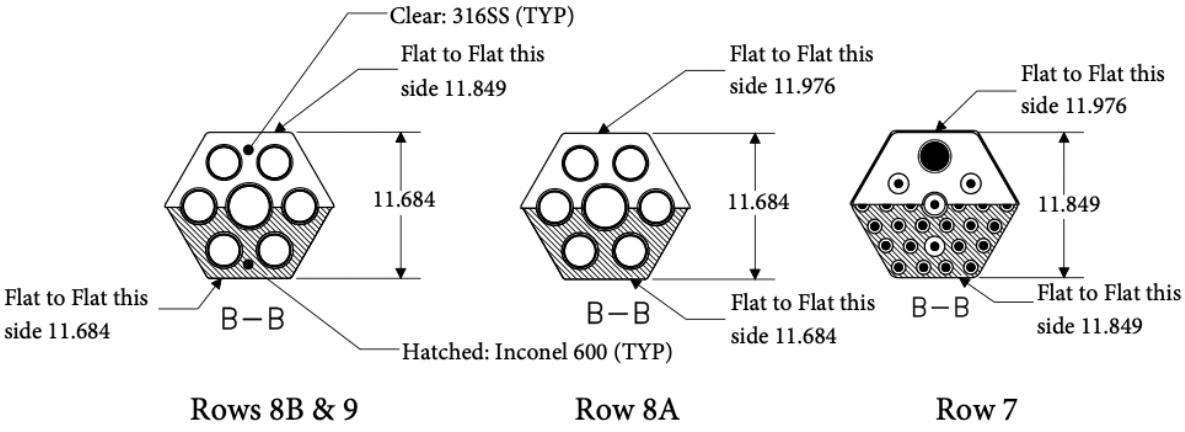

Figure 2.8. Reflector Region Cross Section [1]

Table 2.2. Reflector Assembly Key Dimensions and Parameters

Parameter	REFL7	REFL72	REFL8A	REFL8B	REFL9
Inlet Plenum	Core Basket			Annular Plenum	
Flow Channel Type	Circular		Annular		
Number of Flow Channels	37		7		
Flow Channel Inner Diameter in Reflector Section (cm)	-		1 channel – 2.731 6 channels – 2.248		
Flow Channel Outer Diameter in Reflector Section (cm)	All channels – 0.635		1 channel – 3.040 6 channels – 2.563		
Outer Flat-to-Flat in Reflector Section (cm)	11.849		11.684		

2.1.3 Control and Safety Rods

Reactivity was controlled using nine control rods. Three control rod positions were designated as safety rods (SR) and were typically fully withdrawn during normal reactor operation. Six control rods of two different types (CR1 and CR2) were used to compensate for power defects and burnup reactivity loss. The safety rods and the control rods were geometrically identical. Each control and safety rod consisted of a control rod drive mechanism, control rod disconnect driveline, and an absorber assembly.

Temperature changes of the sodium within the upper internal structure (UIS) caused the control rod drivelines to thermally expand and contract. It is estimated that the sodium volume in the upper internal structure was approximately 10 m^3 with a time constant for the drivelines of 22 seconds.

The absorber assembly portion of the control rod system (shown in Figure 2.9 [1]) contained 61 sealed absorber pins containing natural B_4C pellets, arranged in a hexagonal perforated steel inner duct. The inner duct and pin bundle were contained within an outer duct of the same dimensions as the driver fuel assembly duct (Section 2.1.1). The absorber pin bundle moved axially within the outer duct assembly. When the control rods were fully inserted, the midplane of the control rods were aligned with the midplane of the fuel columns in the driver fuel assemblies. Key dimensions of the absorber assembly are provided in Table 2.3.

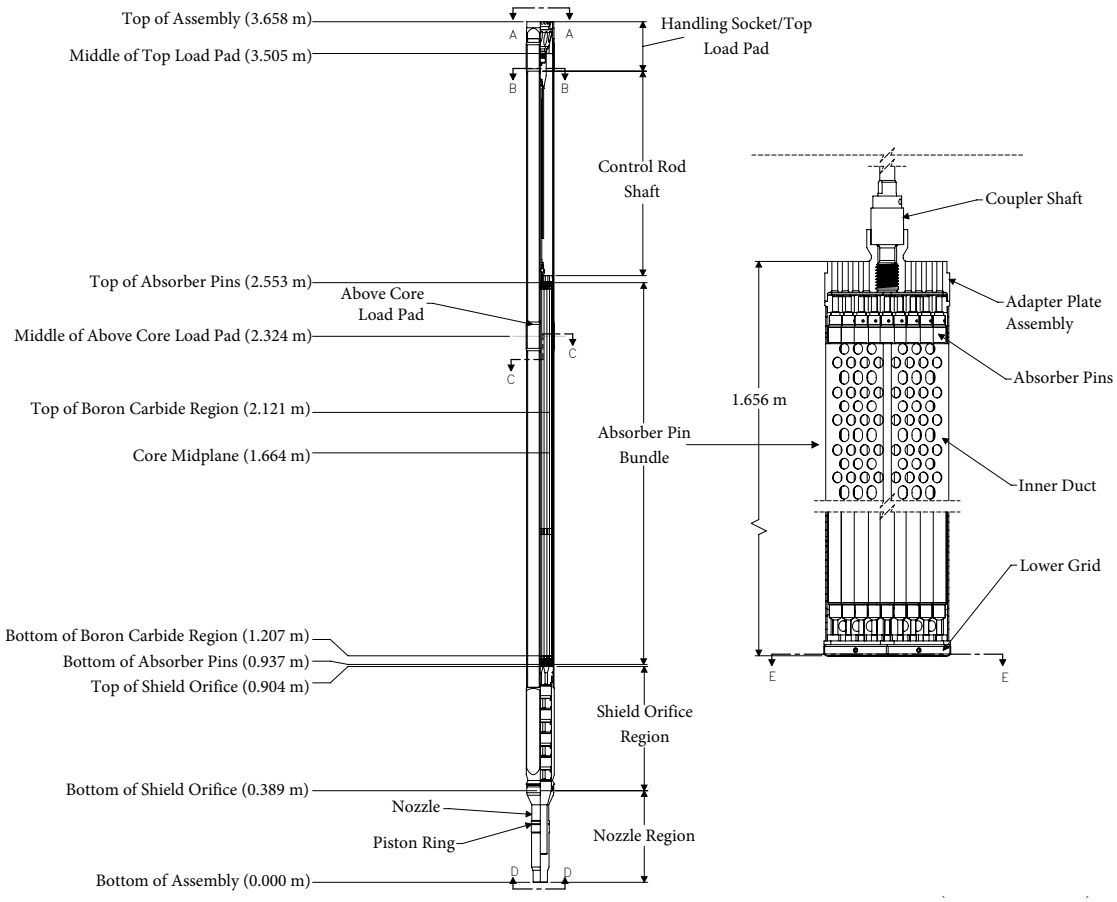

Figure 2.9. Control Rod Absorber Assembly [1]

Table 2.3. Control Rod Assembly Key Dimensions and Parameters

Parameter	Value
Pellet Material	B_4C
Pellet Diameter	Series 1 (CR1): 0.909 cm Series 2 (CR2): 0.919 cm
Cladding Material	Type 316 Stainless Steel
Cladding Diameter	1.204 cm
Cladding Wall Thickness	Series 1 (CR1): 0.130 cm Series 2 (CR2): 0.117 cm
Pin Pitch-to-Diameter Ratio	1.05
Wire Wrap Material	Type 316 Stainless Steel
Wire Wrap Diameter	0.061 cm
Wire Wrap Pitch	49.78 cm

2.1.4 Gas Expansion Modules

A gas expansion module (GEM) was a 4-inch diameter Type 304 stainless steel pipe that was sealed at the top and open at the bottom, as shown in Figure 2.10 [1]. The internal volume of the GEM, which was approximately 0.0283 m^3, was filled with sodium and an argon cover gas bubble.

At full flow conditions, the pressure of the sodium compressed the gas to a level above the top of the active fuel column. During a loss-of-flow transient, the primary pump pressure exerted on the gas by the sodium decreased, allowing the gas to expand and the sodium-gas interface level to decrease. At low flow rates, the sodium-gas interface level would be below the bottom of the fuel column. The displaced sodium at the periphery of the core led to increased neutron leakage and reduced the core reactivity. The exact interface level, and the amount of negative reactivity feedback, depended on the inlet sodium pressure, which was a function of the primary system flow rate and the temperature of the gas, both affected by the reactor power level and core inlet temperature.

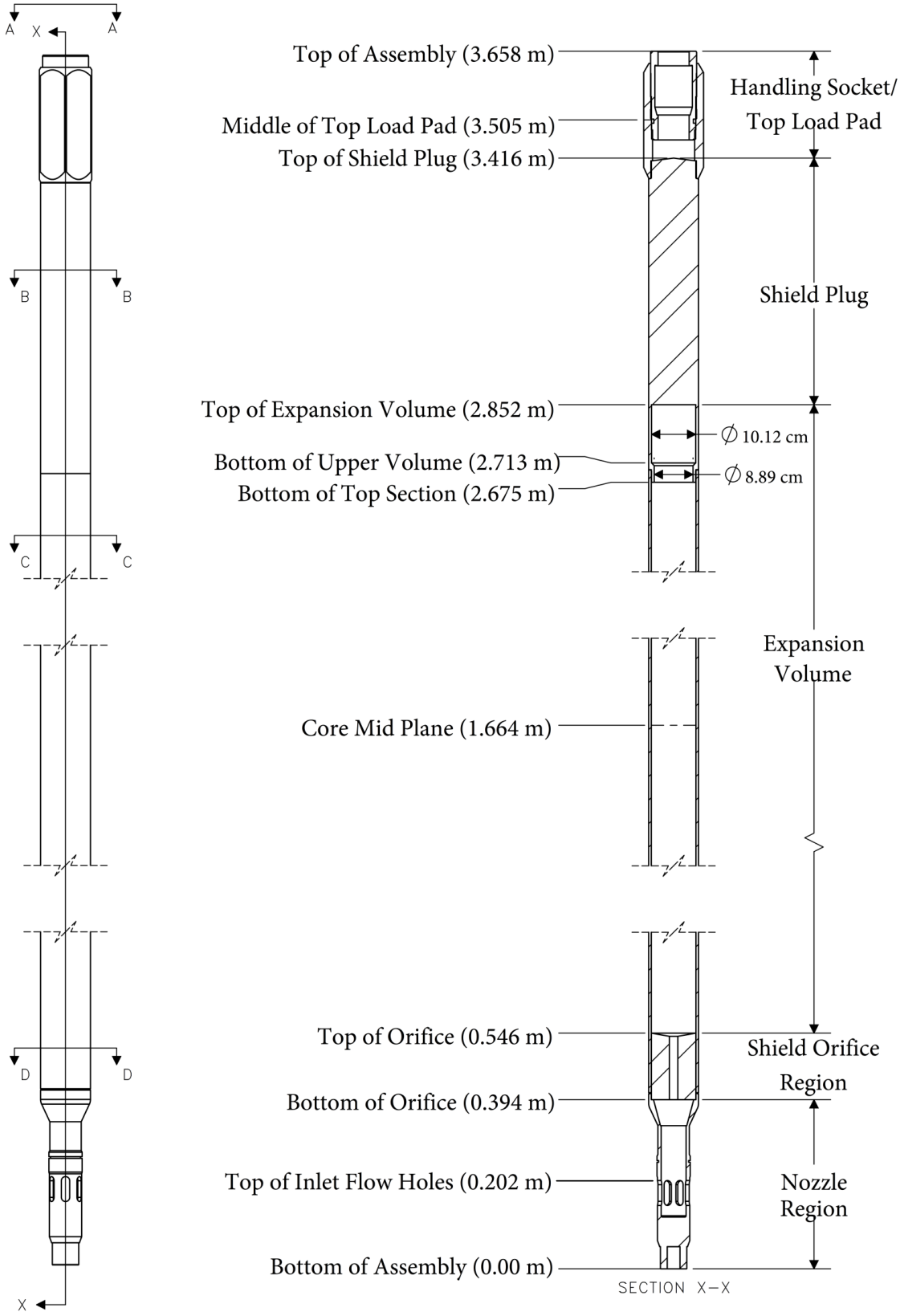

Figure 2.10. Gas Expansion Module Assembly [1]

2.1.5 In-Core Shim Assembly

The in-core shim assembly (ICSA) was a non-fueled assembly installed in the core as a substitute for fuel or test assemblies during reactor operation to reduce the fissile material inventory in the core. The external configuration of the ICSA was identical to the driver fuel assembly described in Section 2.1.1. The ICSA used simulated fuel pins made of Type 316 Stainless Steel. The ICSA was not explicitly modeled in the SAS4A/SASSYS-1 core model described in Section 4.1, and was instead treated as a reflector assembly.

2.1.6 Test Assemblies

The Materials Open Test Assembly (MOTA) was an instrumented open test assembly. The duct contained nine tiers. Five of the tiers were located within the elevation of the core region, three tiers were located above the elevation of the core region, and one tier was located below the elevation of the core region. There were a total of 48 specimen canisters distributed across the different tiers.

The primary purpose of the Fracture Mechanics Assembly (FMA) was to irradiate the FFTF Archives and Surveillance program specimens. Specimens could be positioned along a length inside the outer duct in containers that consisted of different size canisters. The canisters exposed specimens to hot sodium and were designed to accommodate relatively large fracture mechanics specimens plus associated tensile pull specimens, dosimeter, and thermal expansion devices.

The MOTA and FMA were not explicitly modeled in the SAS4A/SASSYS-1 core model described in Section 4.1, and were instead treated as reflector assemblies.

The Cycle 8A core contained several fueled test assemblies. The purpose of these was to test different fuel types, cladding, and duct materials.

The Advanced Oxide Test assemblies (ACO and FO) were a series of advanced oxide fuel tests. Most of these contained larger diameter test pins with annular fuel and blanket pellets clad with HT-9 alloy in an HT-9 duct, while some had solid fuel and blanket pellets clad with D9 alloy in an HT-9 duct. Similarly, the Advanced Oxide Fuel Test assemblies (PO) contained test pins with cladding, wire-wrap, and duct fabricated from alloy D9. The Mixed Carbide Fuel Test assembly (FC) consisted of larger diameter D9 clad, wire wrapped, helium bonded enriched carbide fuel pins. Carbide fuel properties are not explicitly modeled in the SAS4A/SASSYS-1 core model described in Section 4.1.

The D9 Alloy Test assembly (D9) was similar to the standard driver assemblies described in Section 2.1.1, but fabricated with D9 advanced alloy ducts, cladding, wire wrap, and fuel pin end caps. The D9 assembly was not explicitly modeled in the SAS4A/SASSYS-1 core model described in Section 4.1, and was instead treated as a standard driver assembly.

The High Enrichment High Burnup Absorber Test assembly (HEHB) did not have any fuel, but had differing pin diameters, axial heights, and enrichments of B_4C absorber segments. The HEHB was not explicitly modeled in the SAS4A/SASSYS-1 core model described in Section 4.1, and was instead treated as a control assembly.

2.1.7 Core Restraint System

A core restraint system was incorporated into the FFTF design to ensure that core radial motion during power transients would result in an overall negative reactivity feedback. The peripheral reflector assemblies were restrained at two elevations above the active core. The assemblies were restrained below the active core only by the core support plate.

A schematic diagram of the above core load pad (ACLP) and top load pad (TLP) restraint system is presented in Figure 2.11 [1]. The ACLP restraint was made up of two components - the ACLP yoke and the static ring. The ACLP yoke was pinned to the static ring, and the static ring rested on top of the inner shield, thus providing a fixed boundary to the core. The TLP restraint was made up of three components – the TLP yoke, the core restraint module (CRM), and the core barrel. The TLP yoke was attached to six CRMs, which were mounted on the core barrel equally spaced around the periphery of the core. The CRMs held the load pads of the core assemblies in position during operation. Differential expansion of each of the components due to different environments or different thermal time constants determined the net movement of the ACLP and TLP yoke faces.

Estimated thermal time constants for the core restraint system components are provided in Table 2.4 [1]. Estimated steady-state temperature of the components, expressed in fraction of the nominal coolant temperature rise through the core above the core inlet temperature, are also provided.

Table 2.4. Core Restraint Thermal Response Parameters [1]

Component	Percent of Core Temperature Rise (%)	Time Constant (seconds)
Static Ring	39.0	270
ACLP Yoke	39.0	420
Core Barrel Ring	9.3	900
TLP Yoke	20.0	480

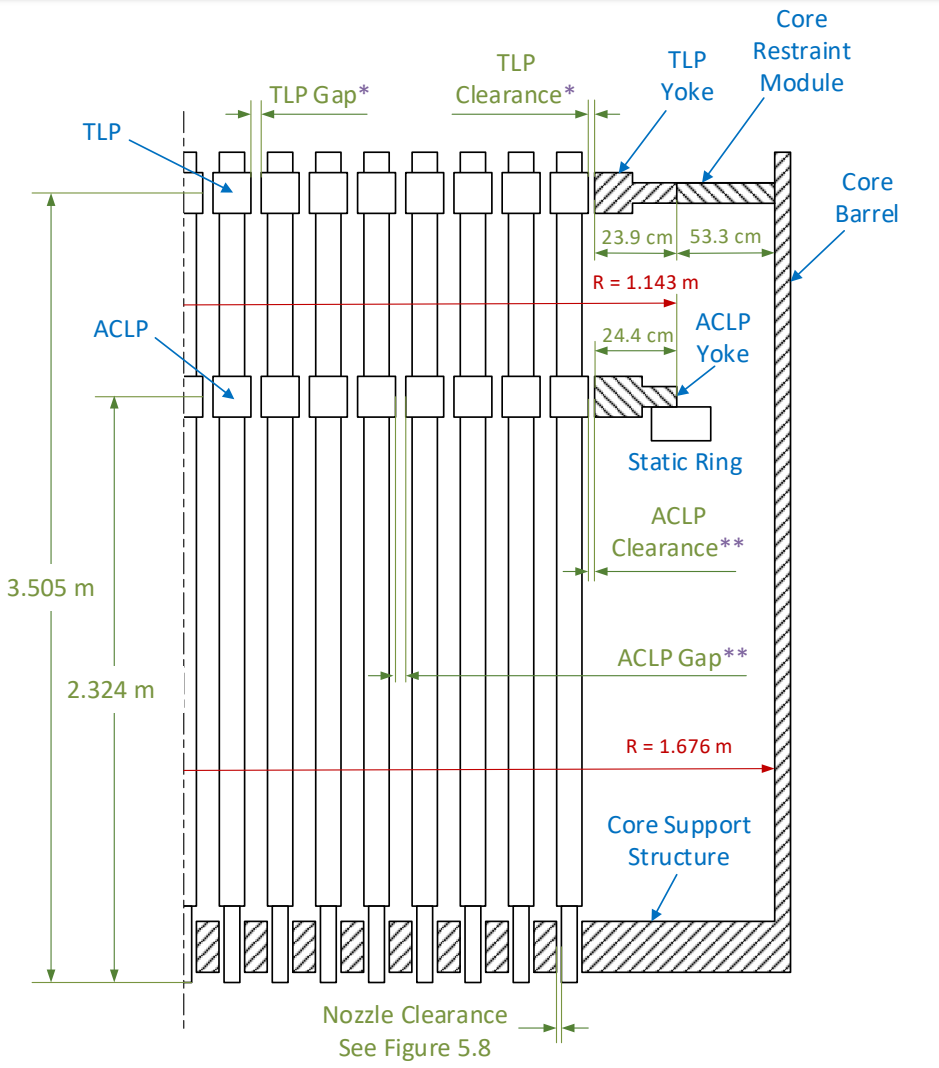

Figure 2.11. Core Restraint Elements and Dimensions [1]

2.2 Reactor Vessel

The FFTF reactor vessel, shown in Figure 2.12 [1], was cylindrical with a torispherical head at the bottom and made of Type 304 stainless steel. Cold sodium discharged from the three primary loop inlet pipes flowed into an inlet plenum at the bottom of the reactor vessel. Sodium was then drawn up into holes on the underside of the core support structure and distributed to the core assemblies and radial shields, as well as to leakage and bypass flow paths that provided sodium flow to the in-vessel storage region, the gap between the reactor vessel and vessel thermal liner, and the gaps between assemblies. Discharge sodium from these flow paths mixed in a common outlet plenum before exiting the reactor vessel through one of three primary loop outlet pipes.

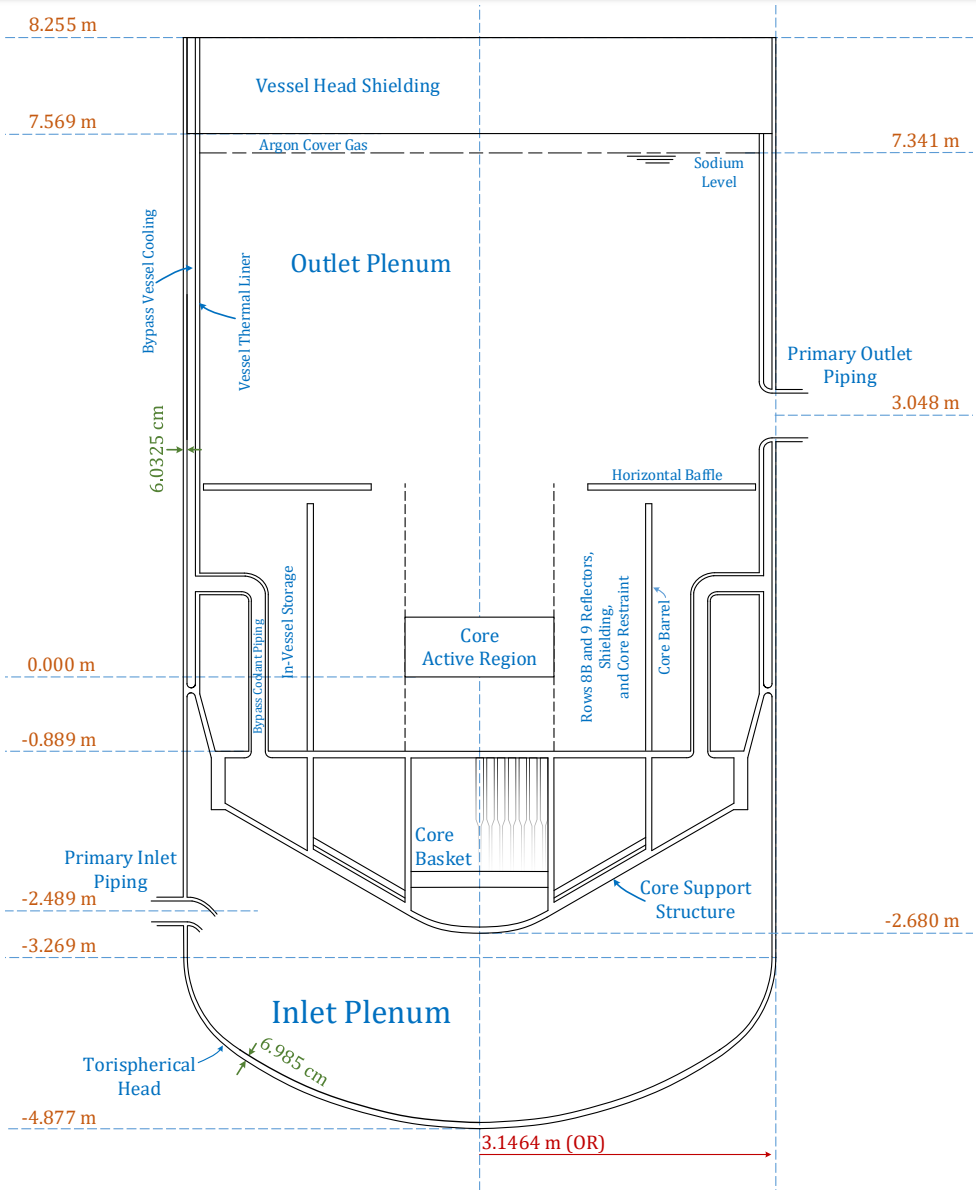

Figure 2.12. Reactor Vessel [1]

Figure 2.13 shows a more detailed view of the flow paths through the reactor vessel. Sodium entered the inlet plenum from one of three primary loop inlet pipes. Flow deflector elbows at the end of these pipes guided the sodium to the bottom of the inlet plenum to encourage mixing. Most of the sodium exited the inlet plenum through holes on the underside of the core support structure into an annular plenum and was distributed through and around the core. The remaining sodium flowed through bypass flow paths.

Most of the sodium that entered the annular plenum flowed inward into the core basket. The remaining sodium flowed up into the radial shield blocks or through the reflector assemblies in Rows 8B and 9. Almost all of the sodium that entered the core basket region provided sodium to the core assemblies. A small amount of sodium that entered the core basket bypassed the core by leaking through the gaps between the assemblies. The final flow path from the core basket bypassed the core down into a low-pressure plenum. Sodium then flowed from the low-pressure plenum to an outer annular region, referred to as the peripheral plenum.

Sodium exited the peripheral plenum through one of two flow paths. Some sodium flowed out through one of three bypass pipes to cool the reactor vessel thermal liner and ultimately discharged in the outlet plenum. The remaining sodium from the peripheral plenum flowed into the in-vessel storage region before discharging into the outlet plenum. More information about leakage and bypass flow rates is available in Reference 1 and Table 3.2.

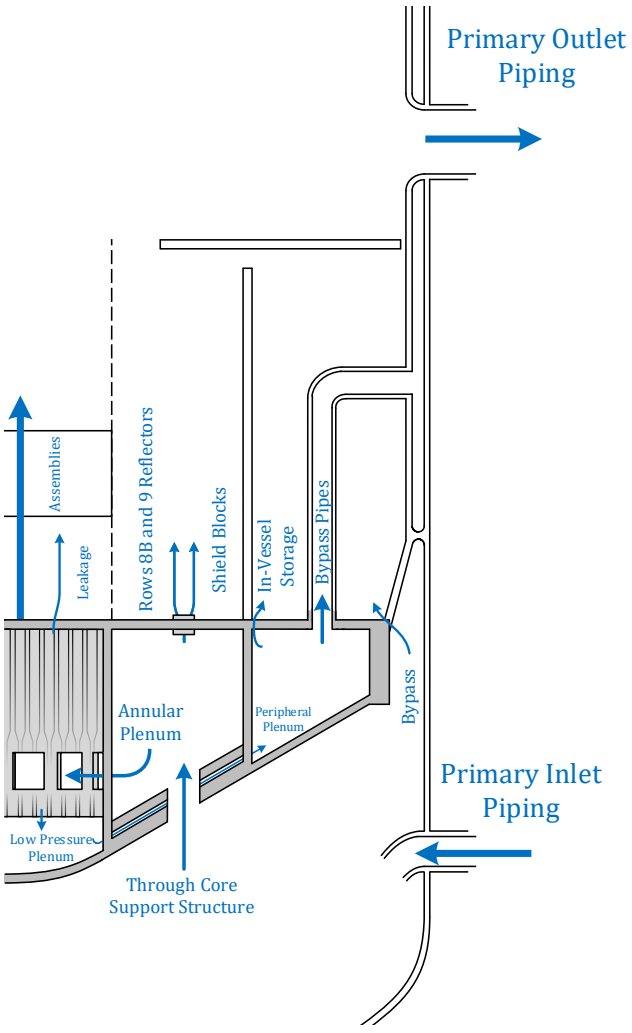

Figure 2.13. Reactor Vessel Flow Paths

2.3 Primary Loops

Three primary loops transported heat generated within the reactor core to the intermediate heat exchangers and back to the reactor vessel. Figure 2.14 [1] illustrates the general arrangement of a single primary loop, and each primary loop contained the same components and had similar geometry. Hot leg piping ran from the reactor vessel to a primary centrifugal pump and into an intermediate heat exchanger. Cold leg piping returned sodium from the IHX to the reactor vessel, discharging into the inlet plenum. More detailed dimensions of the benchmark geometry of the primary loop are provided in Reference 1.

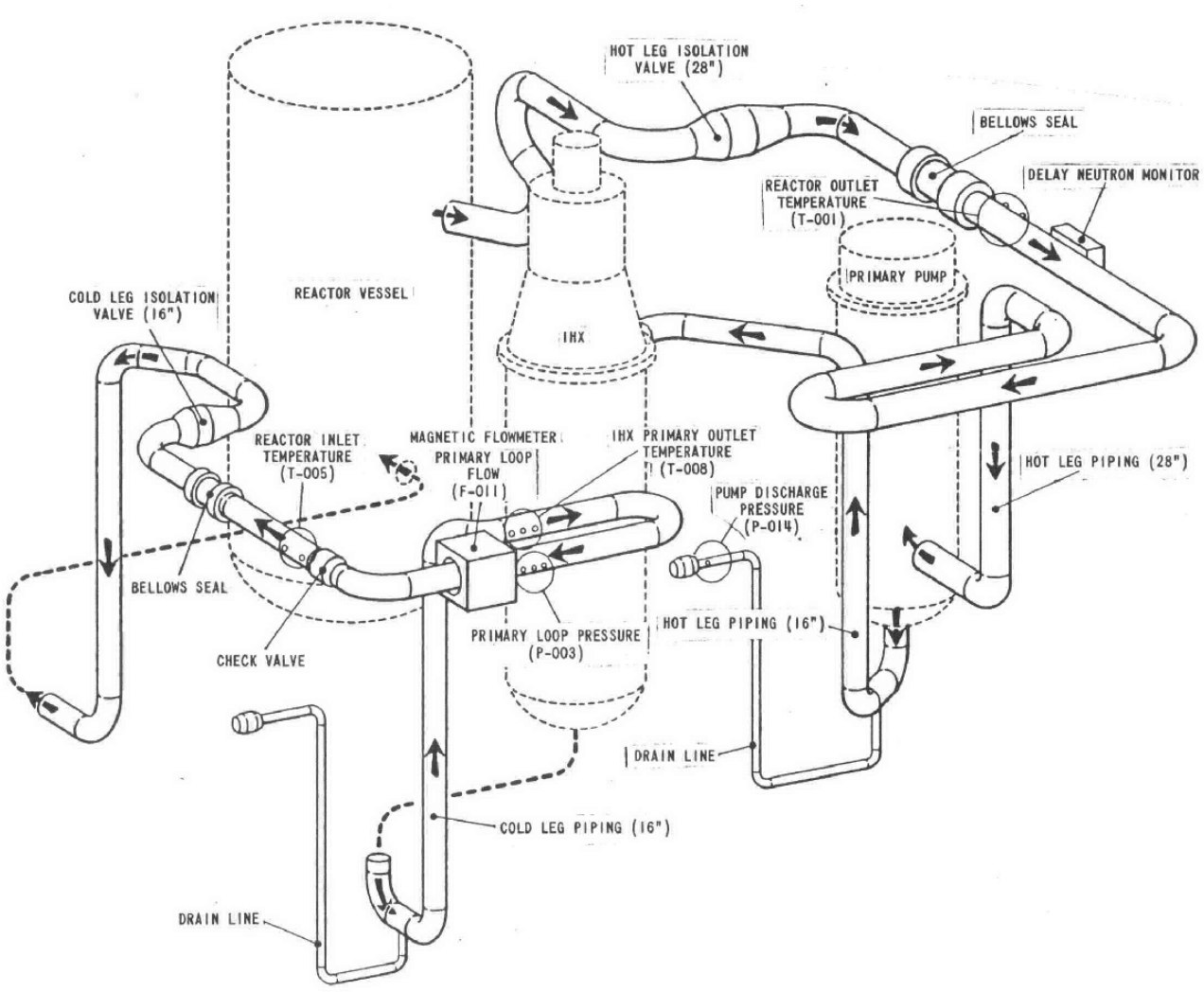

Figure 2.14. Primary Loop Schematic [1]

The intermediate heat exchangers in each primary loop were vertically mounted counterflow shell and tube designs. Primary sodium flowed down through the shell side transferring heat to the secondary sodium flowing up through the IHX tubes, which were installed in concentric rings. The geometry of the IHX is illustrated in Figure 2.15 [1]. Important dimensions and parameters are provided in Table 2.5.

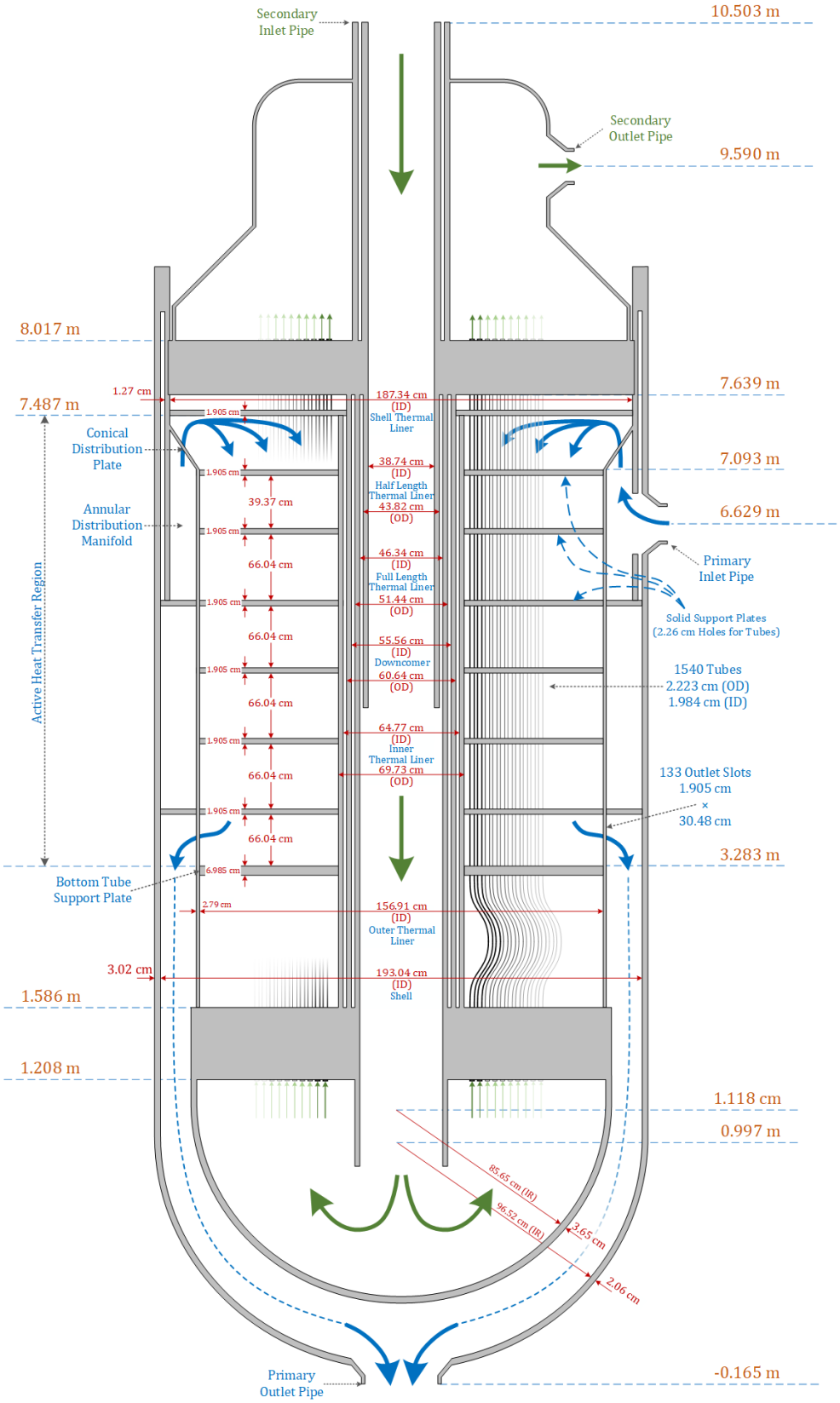

Figure 2.15. Intermediate Heat Exchanger [1]

Table 2.5. Intermediate Heat Exchanger Key Dimensions and Parameters

Parameter	Value
Material	SS-304H
Number of Tubes	1540
Tube Inner Diameter	1.984 cm
Tube Outer Diameter	2.223 cm
Tube Radial Pitch[1]	2.906 cm
Tube Circumferential Pitch[2]	3.650 cm

[1] – Distance between center of tubes in one ring and center of tubes in a neighboring ring

[2] – Center-to-center distance between tubes within the same ring

2.4 Secondary Loops

Each primary loop was connected to a secondary loop by an intermediate heat exchanger. Figure 2.16 [1] illustrates a simplified layout of a single secondary loop, and each of the three secondary loops were very similar. Within each secondary loop, hot leg piping ran from the IHX outlet to a dump heat exchanger unit, which discharged heat to the environment. The cold leg sodium ran from the DHX unit to a centrifugal pump and back to the IHX. More detailed dimensions of the benchmark geometry of the secondary loop are provided in Reference 1.

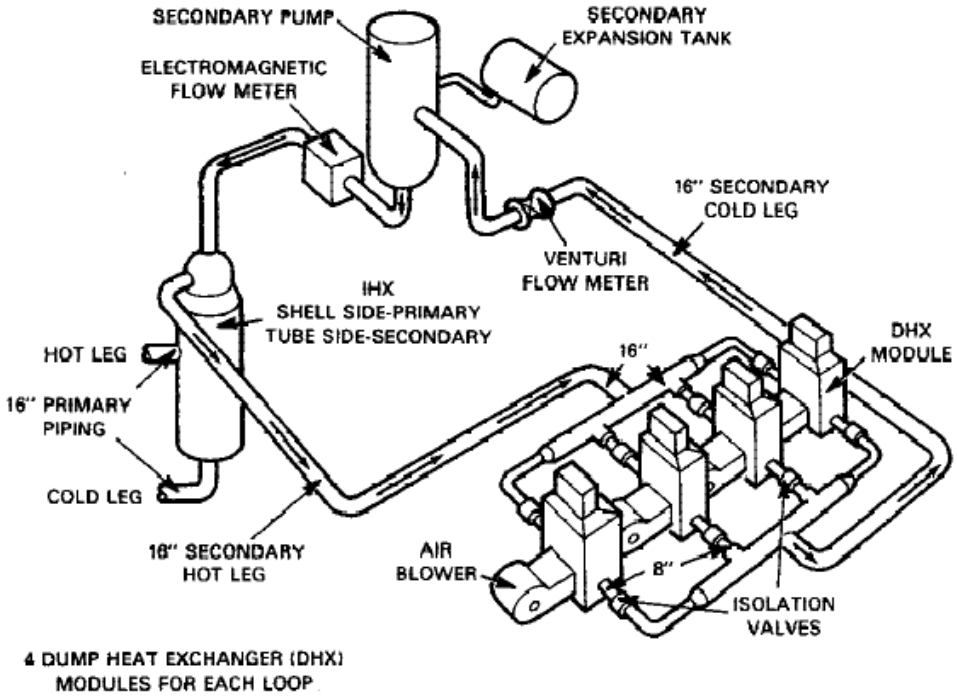

Figure 2.16. Secondary Loop Schematic [1]

Each DHX unit contained four individual dump heat exchanger modules. Secondary sodium flowed through the DHX module finned tubes and rejected heat to ambient air flowing along the outside of the tubes. Figure 2.17 [1] illustrates the geometry of the DHX tubes. Table 2.6 provides important dimensions and parameters for the DHX modules.

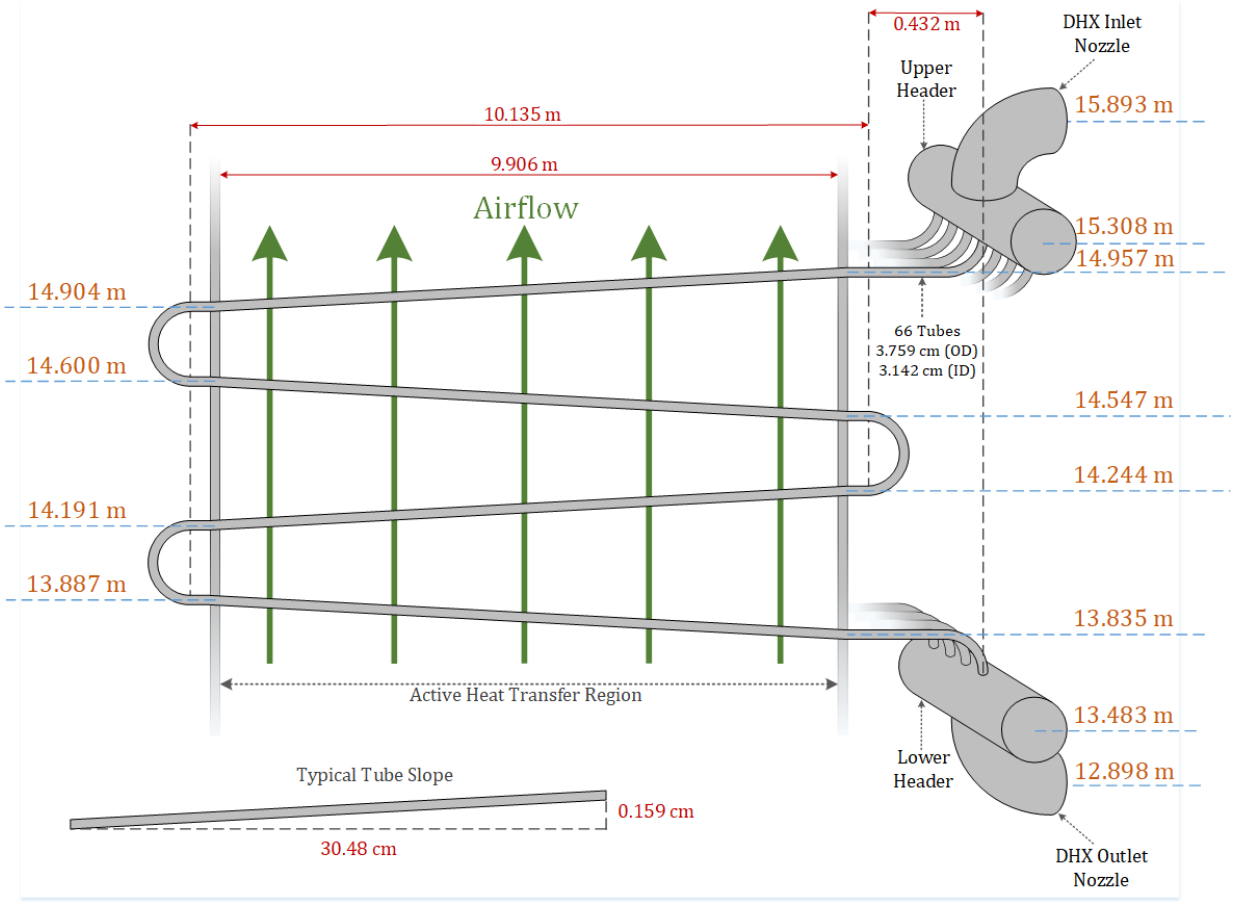

Figure 2.17. Dump Heat Exchanger Tube Bundle [1]

Table 2.6. Dump Heat Exchanger Key Dimensions and Parameters

Parameter	Value
Material	SS-304H
Number of Tubes Per Module	66
Tube Inner Diameter	3.142 cm
Tube Outer Diameter	3.759 cm

2.5 Instrumentation

Plant data was collected at frequencies of up to once per second. To reduce the volume of recorded data, measurements were only recorded if the percent difference between the sampled value and the last recorded value was larger than a preset size. Measurements of power, temperatures, and mass flow rates were taken at various locations.

2.5.1 Power

Neutron flux was monitored by three independent and redundant fission counters located in cooled thimbles at the core midplane, equally spaced around the periphery of the shield. The initial total equilibrium power of the reactor was obtainable through heat balance calculations. The initial fraction of decay heat was calculated using the Cycle 8C power history, which is available in Reference 1, and the ANS decay heat standard [5]. Prompt power was calculated by reducing the total power by the calculated initial decay heat. No information on uncertainties for measured power was available.

2.5.2 Temperature

Fast response thermocouple packages were utilized for a selection of assemblies to record accurate core outlet temperatures during transient conditions. These assemblies were referred to as Proximity Instrumented Open Test Assemblies (PIOTA). The locations of these assemblies are labeled with red letters in Figure 2.3. Above each PIOTA, a separate duct assembly with multiple thermocouples was installed. The instrument duct was in direct contact with the assembly duct such that sodium discharged from PIOTAs flowed along thermocouples just above the assembly outlets. The fast response PIOTAs had an expected response time of 3 seconds. No information on uncertainties for the PIOTAs was available.

Beyond the reactor vessel, temperatures were measured in the hot and cold legs of all primary and secondary loops by resistance temperature detectors (RTD). In the primary loops, RTDs were installed in each hot leg between the isolation valve and the primary pump inlet. Two RTDs were installed in each primary loop cold leg between the IHX outlet and the check valve. The primary loop RTDs are shown in Figure 2.14, and more detailed information about their location is available in Reference 1. The secondary loop hot leg RTDs were installed just before the inlet of the DHXs. Secondary cold leg RTDs were installed in two different locations. The first was in the outlet piping of the individual DHX modules, and the second was after the pump. More detailed information about the location of the secondary loop RTDs is available in Reference 1. The RTDs were assumed to be accurate to within +/- 2.8°F with a response time of 5 seconds.

2.5.3 Mass Flow Rate

Sodium mass flow rates in each loop were measured by permanent magnet flow meters installed in the cold leg piping. The locations of the primary and secondary permanent magnet flow meters are shown in Figure 2.14 and Figure 2.16, respectively, and more detailed information about their location is available in Reference 1. The secondary loops also contained Venturi flow meters. Venturi flow meters are much less accurate at low flow rates, so they were used along with pulsed neutron activation flow meters to calibrate the permanent magnet flow meters. Above 2.27 m^3/min, the permanent magnet flow meters were assumed to be accurate to within +/- 2.8%. Below 1.14 m^3/min, the permanent magnet flow meters were assumed to be accurate to within +/- 0.114 m^3/min.

3 Test Descriptions

3.1 LOFWOS Tests #10-12

Table 3.1 summarizes the set of thirteen LOFWOS tests that were performed during Cycle 8C. For the first set of tests, the primary system pony motors were left on to maintain a minimum primary sodium flow rate of approximately 9% of the nominal full flow. The pony motors were turned off for the remaining LOFWOS tests so that the primary system transitioned to natural circulation without the pony motor assistance.

Table 3.1. Summary of LOFWOS Tests

LOFWOS Test	Date	Initial Power	Initial Flow	Pony Motor
Test #1	7/2/86	10%	100%	On
Test #2	7/3/86	20%	100%	On
Test #3	7/7/86	30%	100%	On
Test #4	7/8/86	40%	100%	On
Test #5	7/9/86	50%	100%	On
Test #6	7/15/86	50%	100%	On
Test #7	7/10/86	10%	100%	Off
Test #8	7/11/86	20%	100%	Off
Test #9	7/11/86	30%	100%	Off
Test #10	7/14/86	40%	100%	Off
Test #11	7/16/86	45%	100%	Off
Test #12	7/17/86	50%	100%	Off
Test #13	7/18/86	50%	100%	Off

Starting from 100% flow and test-specific initial power levels, LOFWOS Tests #10-12 were initiated when the three primary sodium pumps were simultaneously tripped. The secondary loop sodium pumps remained operational throughout the tests. The reactor was maintained at the test initial power level for several hours prior to the test to allow the system to reach an equilibrium state. The conditions for Tests #10-12 are defined below.

3.1.1 Initial Conditions

Table 3.2 summarizes the initial plant conditions for LOFWOS Tests #10-12. The initial power and flow per assembly for each test were determined by scaling the power and flow distributions from Reference 1 to the test initial conditions shown in Table 3.2. Figure 3.1 and Figure 3.2 present the steady-state power and flow of each assembly for LOFWOS Test #12, respectively.

Table 3.2. LOFWOS Tests #10-12 Initial Conditions

	Parameter	Units	Value		
			Test #10	Test #11	Test #12
Core	Power	MWt	160.5	178.4	197.8
	Core Inlet Temperature	K	589.7	590.2	590.1
	Core Flow Rate	kg/s	2062.9	2063.0	2038.2
	Bypass/Shield/Leakage Flow Rate	kg/s	148.7	148.6	146.9
	GEM Sodium Level[1]	cm	221.6	221.6	221.6
Primary Loops	Primary Loop #1 Flow Rate	kg/s	747.0	742.4	738.6
	Primary Loop #2 Flow Rate	kg/s	730.7	725.0	723.7
	Primary Loop #3 Flow Rate	kg/s	733.9	744.2	722.8
Secondary Loops	Secondary Loop #1 Flow Rate	kg/s	729.9	729.9	735.5
	Secondary Loop #2 Flow Rate	kg/s	738.6	736.6	736.6
	Secondary Loop #3 Flow Rate	kg/s	735.8	730.9	731.9
	Average Loop #1 DHX Outlet Temperature	K	578.0	577.4	575.5
	Average Loop #2 DHX Outlet Temperature	K	575.5	575.5	572.7
	Average Loop #3 DHX Outlet Temperature	K	578.1	575.2	575.6

[1]- Elevation relative to top of inlet nozzle holes

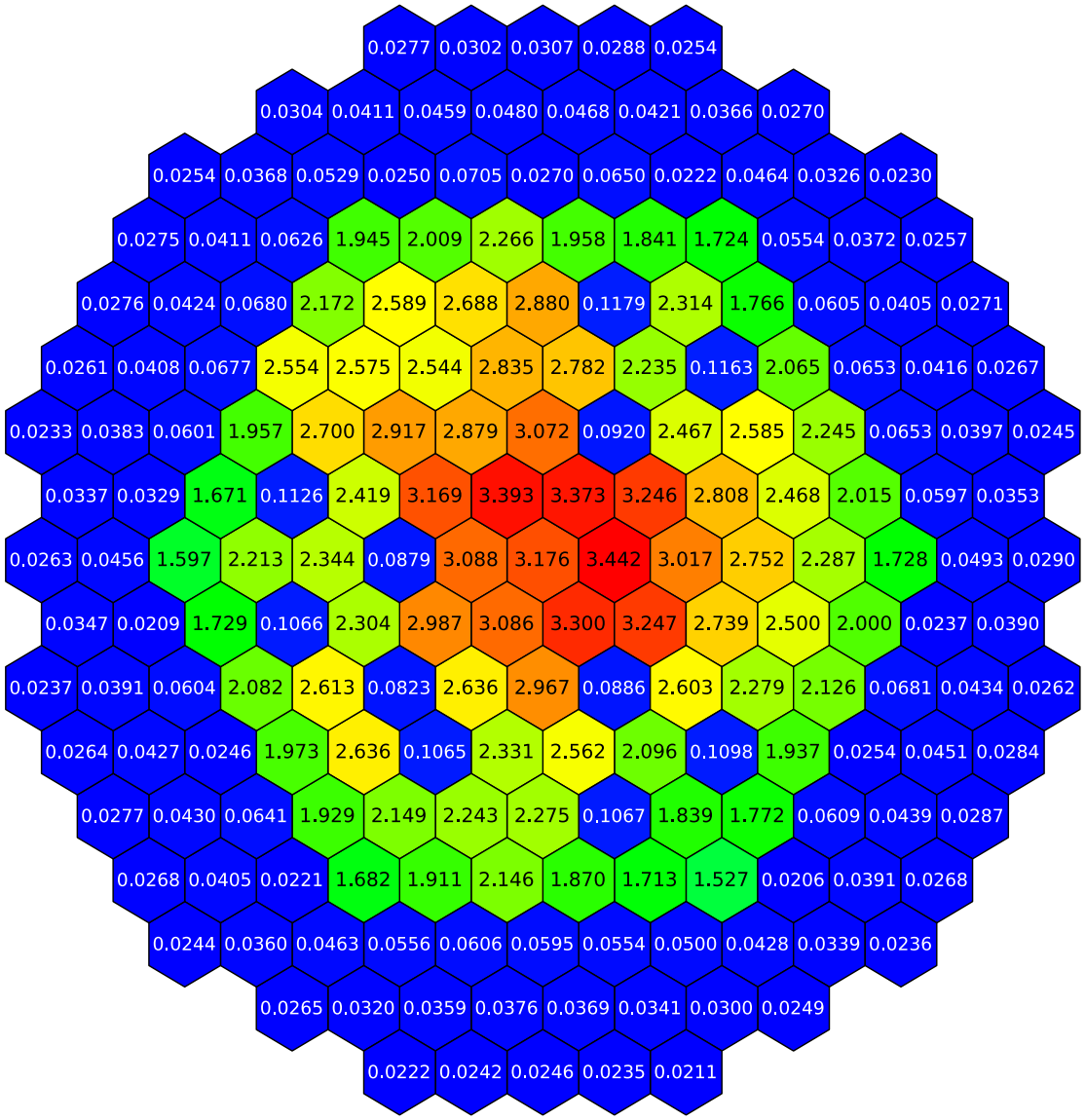

Figure 3.1. Initial Power Per Assembly for LOFWOS Test #12 (MW)

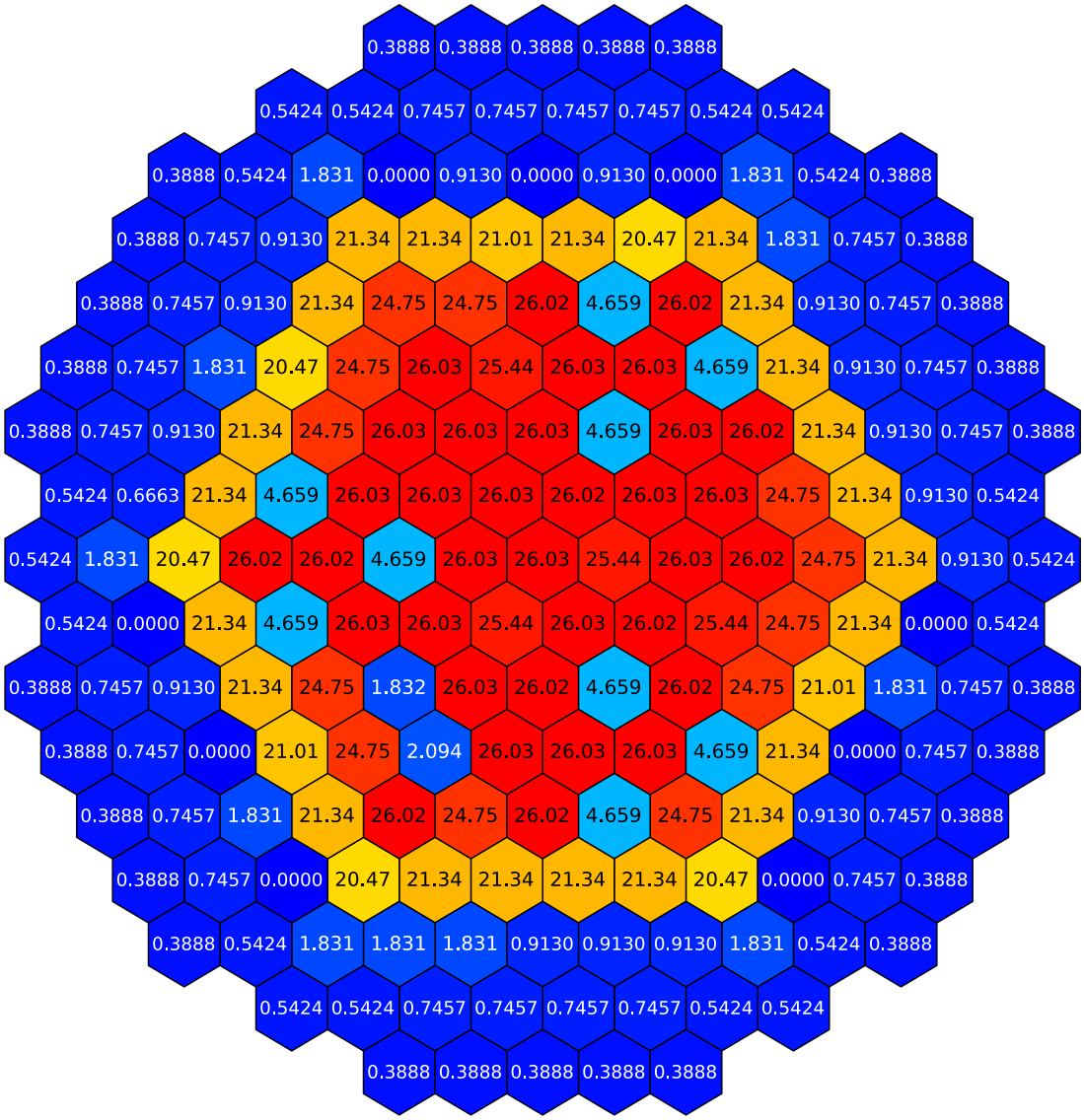

Figure 3.2. Initial Flow Per Assembly for LOFWOS Test #12 (kg/s)

3.1.2 Transient Boundary Conditions

The LOFWOS transients are defined by boundary conditions for primary pump speeds, secondary loop flow rates, and DHX sodium outlet temperatures. Figures 3.3 – 3.5 present these boundary conditions.

Below approximately 100 rpm, the uncertainty of the pump speed measurements was too high to be used reliably. For that reason, measured pump speeds are shown for the first 90 seconds of the transient only. The tests were initiated with the tripping of the three primary pumps, which corresponds to a time of zero seconds in Figures 3.3 – 3.5 . However, the DHX fan speeds were reduced approximately one minute earlier, resulting in higher DHX sodium outlet temperatures. This was done to maintain relatively stable IHX primary-side outlet temperatures during each test. Table 3.2 lists the initial DHX sodium outlet temperatures before the fan speed was reduced, and the increase in sodium outlet temperatures can be seen prior to a time of zero seconds in Figures 3.3 – 3.5.

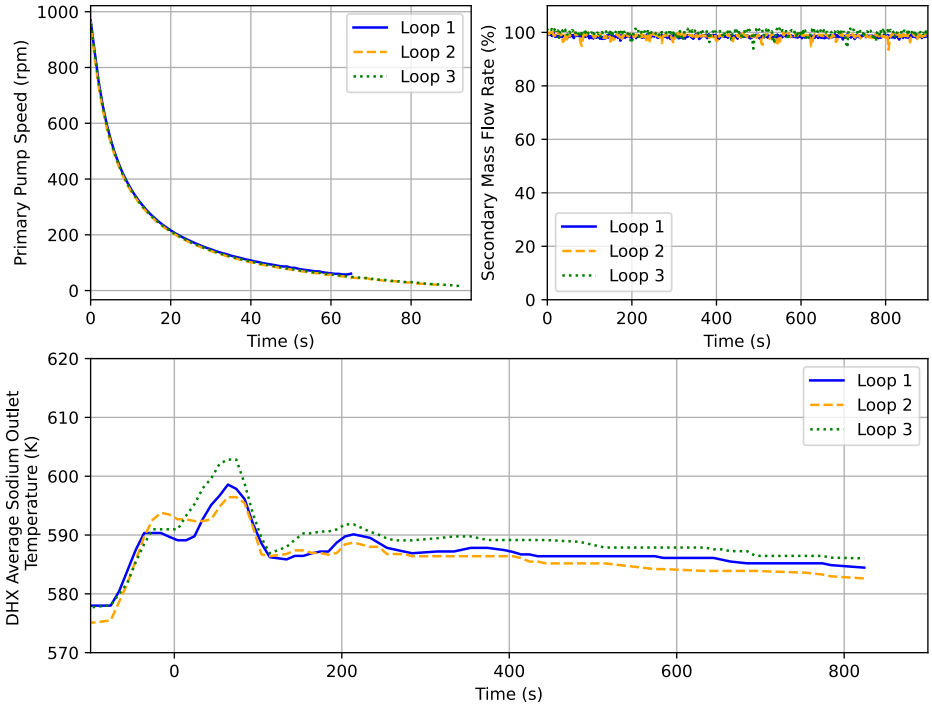

Figure 3.3. LOFWOS-10 Transient Boundary Conditions

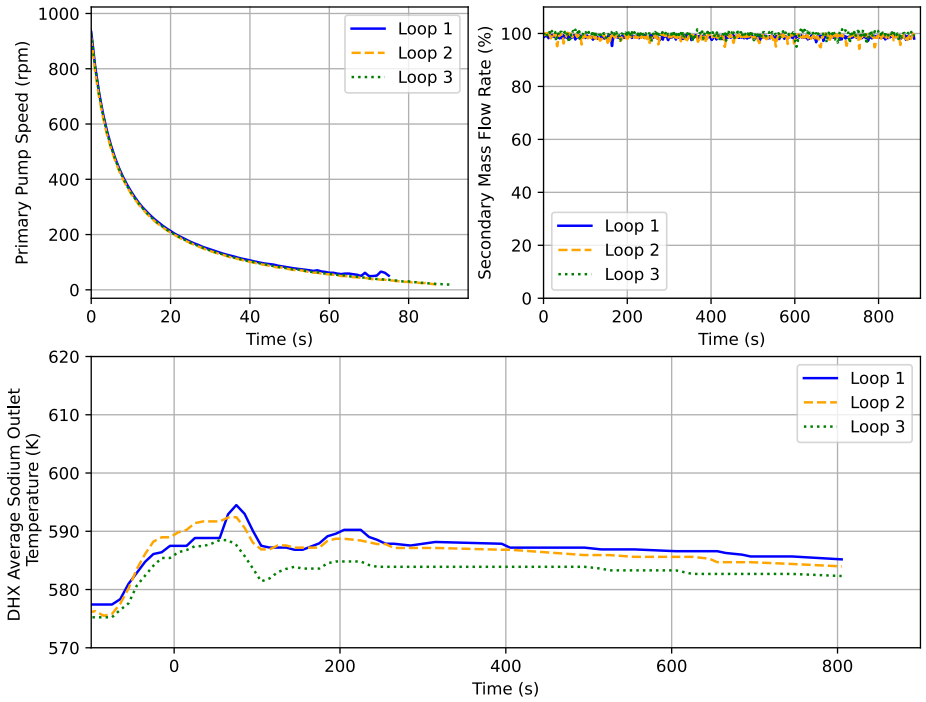

Figure 3.4. LOFWOS-11 Transient Boundary Conditions

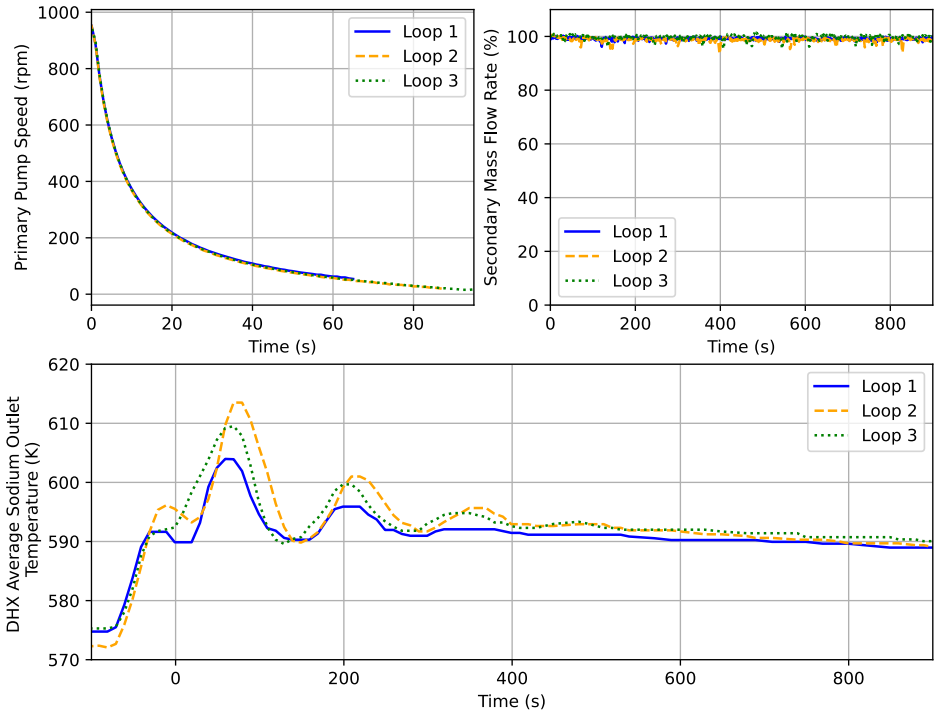

Figure 3.5. LOFWOS-12 Transient Boundary Conditions

3.2 Individual Reactivity Feedback Tests

The individual reactivity feedback tests carried out during Cycle 8A consisted of quasi-static steps where the core was subjected to various power, flow, and inlet temperature conditions. The reactor power was varied between 10% - 100% while coolant conditions covered a range of 67% - 100% flow and 576K – 633K core inlet temperatures. After each change of conditions, the reactor conditions were held constant for a period of about one hour to adjust to new steady-state conditions. Measurements of changes in control rod positions were converted to reactivity using rod worth information to determine the magnitude of the associated reactivity feedbacks between test states. Reactivity change from fuel burnup was also calculated and accounted for in the calculation of reactivity feedback.

The Cycle 8A test campaign consisted of approximately 200 steps of seven different types, each type targeting a different reactivity feedback or group of reactivity feedbacks. Table 3.3 summarizes the types of individual reactivity feedback tests that were performed during Cycle 8A.

Table 3.3. Summary of Individual Reactivity Feedback Test Types [4]

Type Number	Test Type	Description
1	Fuel Temperature	Core inlet temperature was fixed, power and flow rate were varied such that the power-to-flow ratio remained constant. As a result, coolant and structure temperatures remained fairly constant, and the majority of reactivity feedbacks come from the fuel (Doppler and axial expansion).
2	Constant Average Temperature	Power was fixed, core inlet temperature and flow rate were varied such that coolant average temperature in the core remained constant. As a result, the average coolant, cladding, and fuel temperatures did not change, but temperatures for core restraint components were affected.
3	Constant Outlet Temperature	Core inlet temperature and flow rate were varied such that the core outlet temperature remained constant. Power was selected to preserve average fuel temperature. The dominant reactivity feedbacks are the grid plate expansion as well as coolant and structure density effects.
4	Temperature Coefficient	Core inlet temperature was varied, while both power and flow remained fixed, resulting in a uniform change of all core temperatures.
5	Flow Coefficient	Core inlet temperature and power were fixed, while the coolant flow rate was varied. All temperatures changed, except for core grid plate.
6	Static Loss of Flow	Core inlet temperature was fixed, while flow rate was decreased. Control rods were not moved in order to allow power to adjust from reactivity feedbacks only.
7	Power Coefficient	Core inlet temperature and flow rate were fixed, while power was varied. Reactivity feedbacks are dominated by the Doppler and axial expansion in fuel.

Several groups of the Cycle 8A steps were simulated in SAS4A/SASSYS-1. These groups of steps and their corresponding type are listed in Table 3.4. The test types for the analyzed steps were determined by comparing the data to the descriptions of the test types in Table 3.3. The steps were named in a chronological order (1, 2, …), with some steps split in two sub-steps (e.g., 36A and 36B). Sub-steps typically had very similar conditions and were generally modeled as one step (e.g., 36A, 36B).

The Type 5 and Type 6 tests were run in series. For example, step group 40B – 41A is a Type 5 test where core inlet temperature was fixed, flow rate was varied, and power was maintained by moving control rods. After step 41, the control rods were put back to the step 40 position, which created step 42. Therefore, step group 40B – 42B is a Type 6 test, but a Type 5 test was conducted in between at step 41.

Table 3.4. Summary of Individual Reactivity Feedback Tests

Type Number	Test Type	Step Groups
1	Fuel Temperature	6B, 6C – 7A, 7B – 8A, 8B – 9A, 9B – 10A 45B, 45C – 46A – 47A 56A – 57A – 58A – 59A – 60A 61A – 62A
2	Constant Average Temperature	17B – 18A – 19A 34A, 34B – 35A, 35B – 36A, 36B 67B – 68A 83B – 84A – 85A 114B – 115A – 116A 116A – 117A 130B – 131A, 131B – 132A
3	Constant Outlet Temperature	28A, 28B – 29B – 30A, 30B 76A – 77A – 78B 78B – 79A, 79B 123A – 124A – 125A 173A – 174A – 175A – 176A
4	Temperature Coefficient	13A, 13B – 14A 22A – 23A, 23B 43A – 44A, 44B – 45A 85A – 86A
5	Flow Coefficient	40B – 41A 87B – 88A 137B – 138A
6	Static Loss of Flow	40B – 42B 87B – 89B 137B – 139A, 139B
7	Power Coefficient	24A, 24B – 25B, 25C 50B – 51A 52B, 52C – 53A 72B, 72C – 73A – 74A

3.2.1 Initial Conditions

All SAS4A/SASSYS-1 calculations began from the conditions of Step 2B, which represented conditions close to the nominal FFTF full power and flow values. Figure 3.6 and Figure 3.7 present the steady-state power and flow of each assembly for Step 2B, respectively. Assembly power was generated using the PERSENT code utilizing P_3 DIF3D-VARIANT transport calculations, accounting for both neutron power and gamma heating.

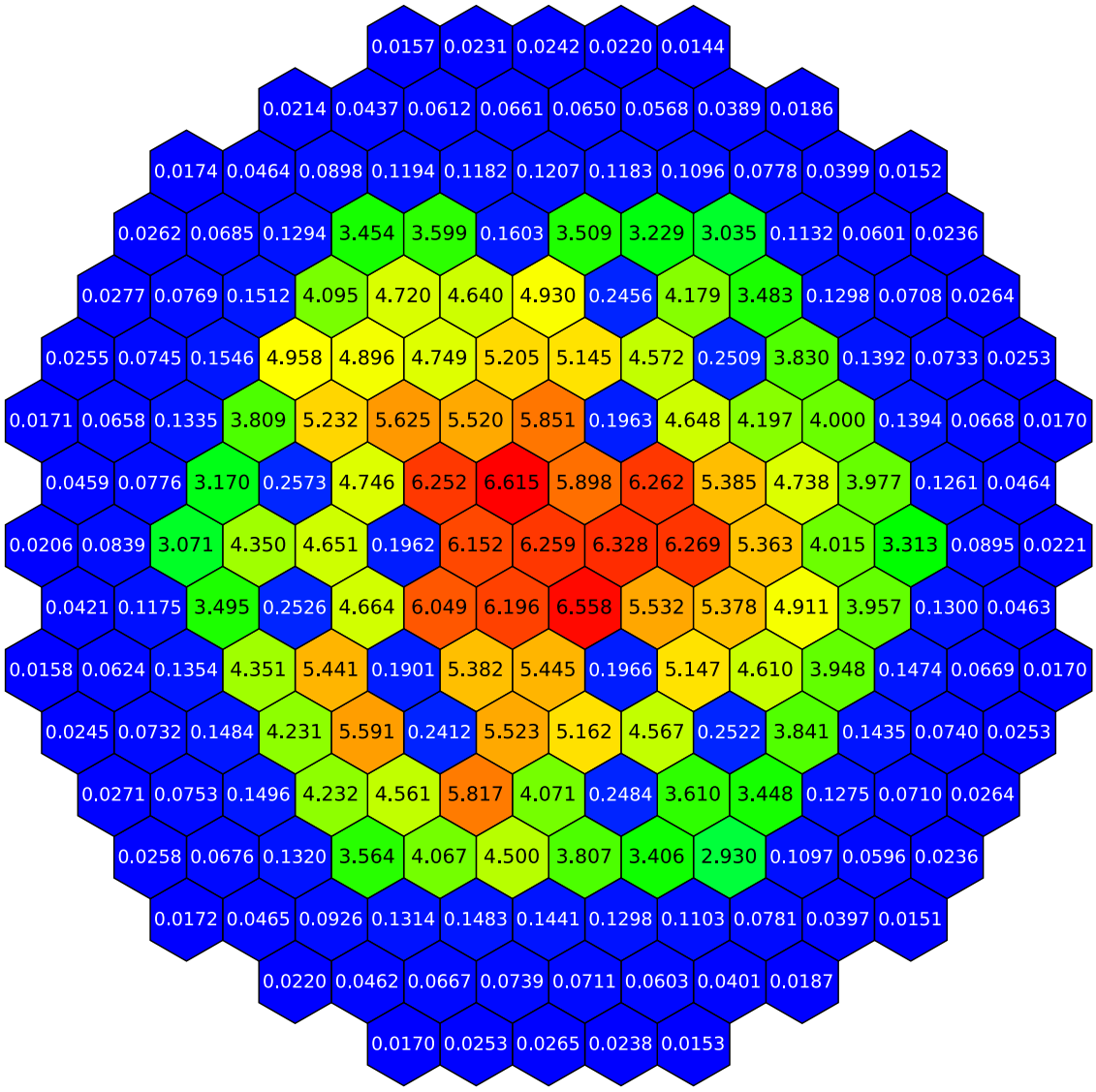

Figure 3.6. Initial Power Per Assembly for Cycle 8A Individual Reactivity Feedback Tests (MW)

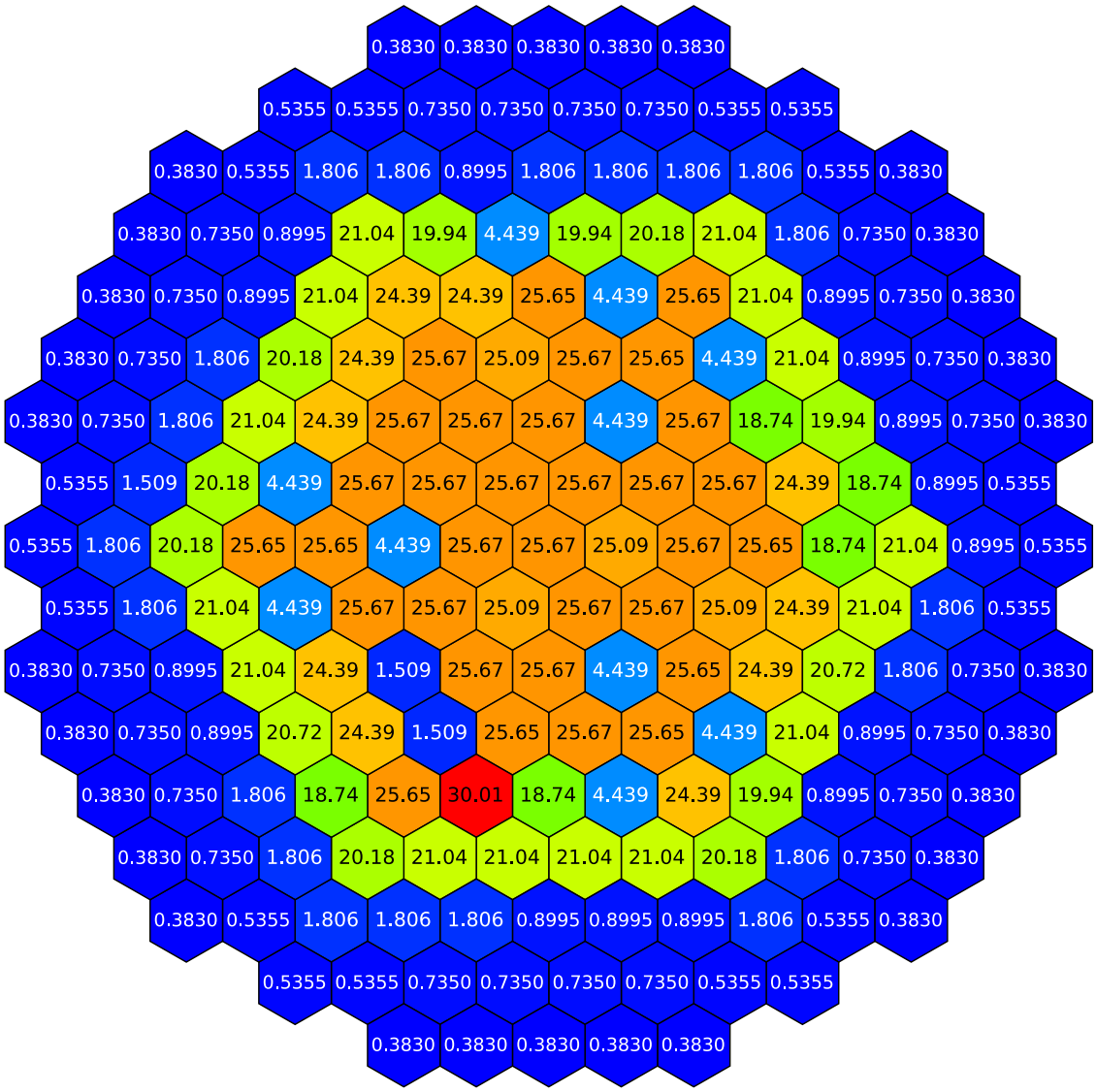

Figure 3.7. Initial Flow Per Assembly for Cycle 8A Individual Reactivity Feedback Tests (kg/s)

3.2.2 Transient Boundary Conditions

The individual reactivity feedback tests are defined by boundary conditions for power, core flow rate, and core inlet temperature. The boundary conditions for each step in the Cycle 8A individual reactivity feedback tests are presented in Appendix A. When simulating each step in SAS4A/SASSYS-1, the first 500 to 1000 seconds of the simulation were devoted to the changes from the previous step, and the last 500 to 1000 seconds simulated the hold time to achieve new steady-state conditions. These times are shorter than the actual test durations but were judged to be sufficient to stabilize all the temperatures in the SAS4A/SASSYS-1 results.

4 SAS4A/SASSYS-1 Model

This section describes the SAS4A/SASSYS-1 models that were developed for simulating the FFTF LOFWOS and individual reactivity feedback tests. The LOFWOS tests utilized the detailed heat transport system model capabilities of SAS4A/SASSYS-1 as described in Section 4.5. The simulations for the Cycle 8A individual reactivity feedback tests were done using a core-only model since their analysis is focused on the core reactivity feedbacks. Inputs for the core inlet temperature and flow rate were directly specified as boundary conditions using the measured data described in Appendix A.

4.1 Core Channels

In SAS4A/SASSYS-1, the thermal-hydraulic performance of a reactor core is analyzed with a model consisting of a number of single-pin channels. The channel model provides input to specify a single fuel pin and its associated coolant and structure. A single-pin model represents the average pin in an assembly, and assemblies with similar reactor physics and thermal-hydraulic characteristics are grouped together. A number of channels are selected to represent all assemblies in the reactor core.

Figure 4.1 illustrates the geometry used in the SAS4A/SASSYS-1 channel thermal-hydraulic model [6]. Heat generated in the fuel is assumed to travel radially through the cylindrically symmetrical pin into the coolant. Axial zones represent the fueled and gas plenum regions as well as upper and lower reflector zones. Reflector zones represent the regions of an assembly above the gas plenum and below the fuel. Each axial zone is also connected to a structure region, which can be used to model components such as wire-wrap or duct walls. Two-node slab geometry is used to represent both the reflector and structure regions.

At each axial location, temperatures are calculated at multiple radial nodes in the fuel, cladding, reflectors, and structure. A single bulk coolant temperature is assumed at each axial location. One-dimensional, radial heat transport calculations are performed at each axial segment from the fuel, through the cladding and into the coolant. Heat transfer is also calculated from the coolant to the gas plenum, reflector, and structure regions. The momentum equation is solved to determine the axial coolant flow. Convective heat transfer is assumed to dominate so axial heat conduction is neglected.

The nine GEM assemblies that were in the Cycle 8C core are filled with gas rather than coolant during the majority of the LOFWOS transients. For this reason, the GEM assemblies are not modeled as channels. Reactivity feedback from the GEM assemblies is included in the Cycle 8C model using the control system as described in Section 4.4.4. The remaining 190 assemblies of the FFTF Cycle 8C core and the 199 assemblies of the Cycle 8A core were modeled using four different base channel types:

- Driver Fuel Channel
- Fueled Tests Channels
- Reflector Channel
- Control Rod Channel

Sections 4.1.1 – 4.1.4 present the models for these channel types. The core model for Cycle 8C is described in Section 4.2. The core model for Cycle 8A is described in Section 4.3.

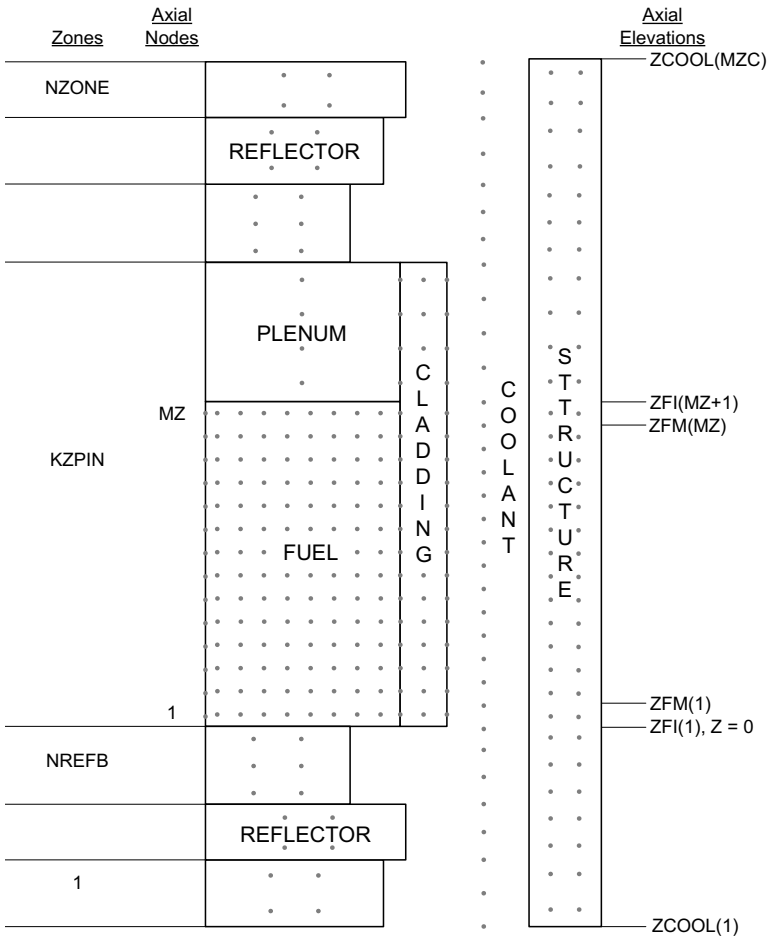

Figure 4.1. SAS4A/SASSYS-1 Core Channel Geometry

4.1.1 Driver Fuel Channel

The driver assemblies described in Section 2.1.1 were modeled using the driver fuel channel, which consists of six axial zones. The first lower reflector zone represents the inlet nozzle from the bottom of the flow holes to the bottom of the shield zone. The second lower reflector zone is the orifice region. The third lower reflector zone represents the remainder of the shield/orifice region below the fuel pin zone. Zone 4 is the fuel pin zone and includes the fissile fuel, blanket regions, and gas plenum. The end caps at the bottom of the fuel pin are included in the pin zone as a lower blanket region. Two upper reflector zones represent the structure above the gas plenum and the handling socket. The geometry of each driver channel type is identical with the exception of the second lower reflector zone which represents the orifice region. There are five geometric variations of this zone which reflect differences in the flow orificing blocks depending on the driver type and location.

Table 4.1 describes key input parameters and Figure 4.2 illustrates the axial geometry for the driver fuel channel.

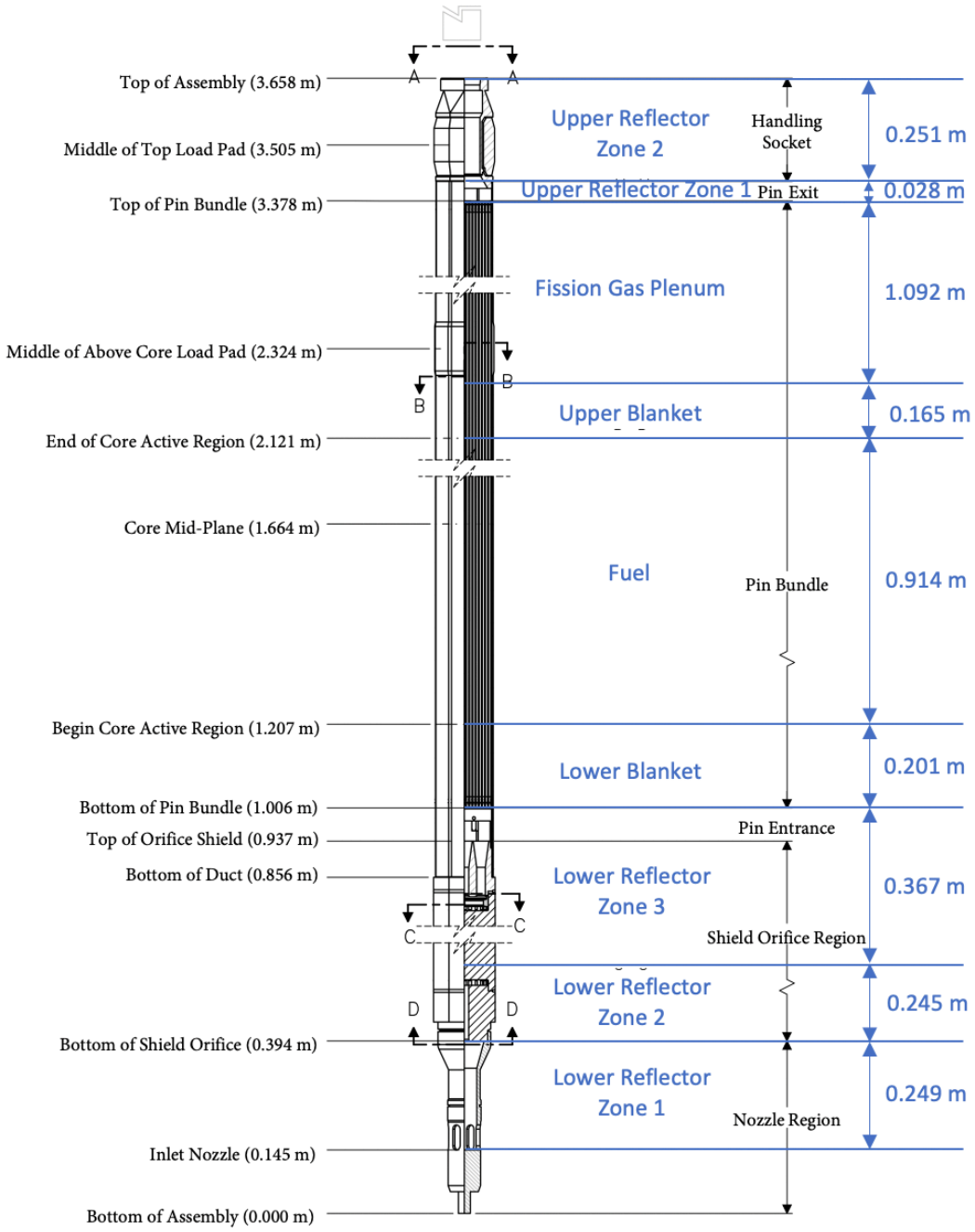

Figure 4.2. SAS4A/SASSYS-1 Model Zones and Regions for Driver Channel

Table 4.1. Driver Fuel Channel Key Input Parameters

Zone	Description	Number of Axial Segments (NZNODE)	Zone Height (ZONEL)	Flow Area Per Pin (AZZC)	Hydraulic Diameter (DHZ)
6	Upper Reflector 2	2	0.251 m	1.831E-05 m^2	7.109E-02 m
5	Upper Reflector 1	1	0.028 m	3.736E-05 m^2	1.016E-01 m
4	Gas Plenum	6	1.092 m	2.003E-05 m^2	3.267E-03 m
	Fuel	23	1.280 m		
3	Lower Reflector 3	3	0.367 m	9.945E-06 m^2	1.981E-02 m
2	Lower Reflector 2	2	0.245 m		
	3.2 Driver			7.425E-06 m^2	9.244E-03 m
	3.1 Driver, Row 5			6.593E-06 m^2	8.711E-03 m
	3.1 Driver, Row 6			4.713E-06 m^2	7.365E-03 m
	4.1/4.2 Driver, Rows 2-5			7.466E-06 m^2	9.270E-03 m
	4.1 Driver, Row 6			4.362E-06 m^2	7.085E-03 m
1	Lower Reflector 1	2	0.249 m	1.182E-05 m^2	5.712E-02 m

4.1.2 Fueled Tests Channels

The Cycle 8A core contained several fueled test assemblies that were not present in Cycle 8C. Three channel types were created for the Cycle 8A core model to represent the Advanced Oxide Test assemblies (ACO and FO), the Advanced Oxide Fuel Test assemblies (PO) and the Mixed Carbide Fuel Test assemblies (FC) described in Section 2.1.6. These channels have the same axial nodalization (NZNODE and ZONEL) as the driver fuel channel described in Section 4.1.1. Carbide fuel material properties are not explicitly modeled in the FC channel and are instead represented using Inconel material properties. Table 4.2 presents the key input parameters for the fueled tests channels that differ from the driver fuel channel.

Table 4.2. Fueled Tests Channels Key Input Parameters

Zone	Description	Flow Area Per Pin (AZZC)	Hydraulic Diameter (DHZ)
ACO and FO Channel			
6	Upper Reflector 2	2.351E-05 m^2	7.109E-02 m
5	Upper Reflector 1	4.797E-05 m^2	1.016E-01 m
4	Gas Plenum/Fuel	2.368E-05 m^2	3.364E-03 m
3	Lower Reflector 3	1.277E-05 m^2	1.981E-02 m
2	Lower Reflector 2	9.534E-06 m^2	9.244E-03 m
1	Lower Reflector 1	1.518E-05 m^2	5.712E-02 m
PO Channel			
6	Upper Reflector 2	2.351E-05 m^2	7.109E-02 m
5	Upper Reflector 1	4.797E-05 m^2	1.016E-01 m
4	Gas Plenum/Fuel	2.252E-05 m^2	3.199E-03 m
3	Lower Reflector 3	1.277E-05 m^2	1.981E-02 m
2	Lower Reflector 2	9.534E-06 m^2	9.244E-03 m
1	Lower Reflector 1	1.518E-05 m^2	5.712E-02 m
FC Channel			
6	Upper Reflector 2	4.365E-05 m^2	7.109E-02 m
5	Upper Reflector 1	8.909E-05 m^2	1.016E-01 m
4	Gas Plenum/Fuel	4.342E-05 m^2	4.407E-03 m
3	Lower Reflector 3	2.371E-05 m^2	1.981E-02 m
2	Lower Reflector 2	1.771E-05 m^2	9.244E-03 m
1	Lower Reflector 1	2.819E-05 m^2	5.712E-02 m

4.1.3 Reflector Channel

Compared with the driver assemblies, the contribution from the reflector assemblies to the overall simulation results is small, primarily because fueled assemblies dominate the reactivity feedbacks. Therefore, detailed modeling of the reflector assemblies was not as essential as for the fueled assemblies. The reflector channel has the same axial nodalization (NZNODE and ZONEL) as the driver fuel channel described in Section 4.1.1. To simplify the reflector channel model, only the core region is represented by the structure illustrated in Figure 2.8. Channel geometry above and below the core was assumed to be identical to that of the driver fuel channel with a 3.2 Driver orifice region.

Since 72 of the 98 reflector assemblies in Cycle 8C and 72 of the 107 reflector assemblies in Cycle 8A were of the Rows 8 and 9 reflector design illustrated in the first two cross sections shown in Figure 2.8, that 7-pin geometry was chosen to represent all reflector assemblies in the model. For simplicity, the seven solid steel rods were all modeled with the diameter of the six peripheral rods. Coolant channel dimensions were calculated to preserve the coolant flow area, and the rest of the reflector material was represented as structure in the channel model.

The reflector channel was also used to model the unfueled test assemblies (MOTA, ICSA, and FMA), since their contribution to the overall simulation results is also small. Table 4.3 presents the key input parameters for the reflector channel that differ from the driver fuel channel.

Table 4.3. Reflector Channel Key Input Parameters

Zone	Description	Flow Area Per Pin (AZZC)	Hydraulic Diameter (DHZ)
6	Upper Reflector 2	5.675E-04 m^2	7.109E-02 m
5	Upper Reflector 1	1.158E-03 m^2	1.016E-01 m
4	Gas Plenum/Fuel	1.114E-04 m^2	3.948E-03 m
3	Lower Reflector 3	3.083E-04 m^2	1.981E-02 m
2	Lower Reflector 2	2.302E-04 m^2	9.244E-03 m
1	Lower Reflector 1	3.665E-04 m^2	5.712E-02 m

4.1.4 Control Channel

The control channel has the same axial nodalization (NZNODE and ZONEL) as the driver fuel channel described in Section 4.1.1. Similar to the reflector channel, the control channel geometry above and below the core was assumed to be identical to that of the driver fuel channel with a 3.2 Driver orifice region. The geometry of the control channel model assumes full insertion of the control rods. This assumption was compensated for by scaling the input for the coolant density feedback to preserve the total coolant worth and is described further in Section 4.4.1. Table 4.4 presents the key input parameters for the control channel that differ from the driver fuel channel. The control channel was also used to model the High Enrichment High Burnup Absorber Test assembly (HEHB) in the Cycle 8A core model.

Table 4.4. Control Channel Key Input Parameters

Zone	Description	Flow Area Per Pin (AZZC)	Hydraulic Diameter (DHZ)
6	Upper Reflector 2	6.512E-05 m^2	7.109E-02 m
5	Upper Reflector 1	1.329E-04 m^2	1.016E-01 m
4	Gas Plenum/Fuel	5.799E-05 m^2	5.043E-03 m
3	Lower Reflector 3	3.538E-05 m^2	1.981E-02 m
2	Lower Reflector 2	2.641E-05 m^2	9.244E-03 m
1	Lower Reflector 1	4.205E-05 m^2	5.712E-02 m

4.2 Cycle 8C Core Model

The FFTF Cycle 8C core model used to simulate the LOFWOS tests consists of 29 channels created from the three base channel types described in Section 4.1. Variations of the three base channel models were created to assign initial flow rates as shown in Figure 3.2, model the different driver fuel orifice regions as described in Section 4.1.1, enable channel-to-channel heat transfer, assign reactivity feedback and decay heat parameters, and separate PIOTA assemblies into individual channels for direct comparison with measured test data. Table 4.5 summarizes the core channels and Figure 4.3 illustrates which channel each assembly was assigned to. Note that the GEM assemblies are not modeled as channels.

The ducted assembly design in FFTF prevents coolant mixing between fuel assemblies, potentially resulting in temperature gradients between neighboring assemblies. Considering the excellent thermal conductivity of sodium coolant in the inter-assembly gap, these temperature gradients could result in significant heat transfer between assemblies. Additionally, though the GEM assemblies are mostly filled with gas rather than coolant during the majority of the LOFWOS transients, there is a possibility of heat transfer through the solid steel plug at the top of the assemblies that could act as a heat conductor. These effects could be especially pronounced at the low power and flow conditions experienced during the LOFWOS tests. To account for this, the channel-to-channel heat transfer model in SAS4A/SASSYS-1 was activated to model heat transfer through the following paths:

- Between PIOTA assemblies and their neighbors
- Between PIOTA neighbors (for example, between Channels 19 and 20)
- Between PIOTA neighbors and their neighbors
- Between all reflector assemblies
- Across GEMs (for example, between Channels 9 and 16)

Inputs characterizing heat transfer perimeter times the heat transfer coefficient for each pair of channels participating in the heat transfer were entered into the model.

Due to the single-pin approximation used in SAS4A/SASSYS-1, there is an implicit assumption that all pins are located next to the duct wall. However, the average pins are located at some distance from the duct wall, where the heat transfer path is longer than if the pins were at the edge. In order to better understand the relationship between the heat transfer characteristics for average and edge pins, a sub-channel model of the FFTF assemblies which takes into account power and temperature distribution between the pins was created and studied. This sub-channel model was used to create correction factors for fueled channel heat transfer inputs that result in an equivalent heat transfer for the single pin model. The sub-channel model is not discussed further here.

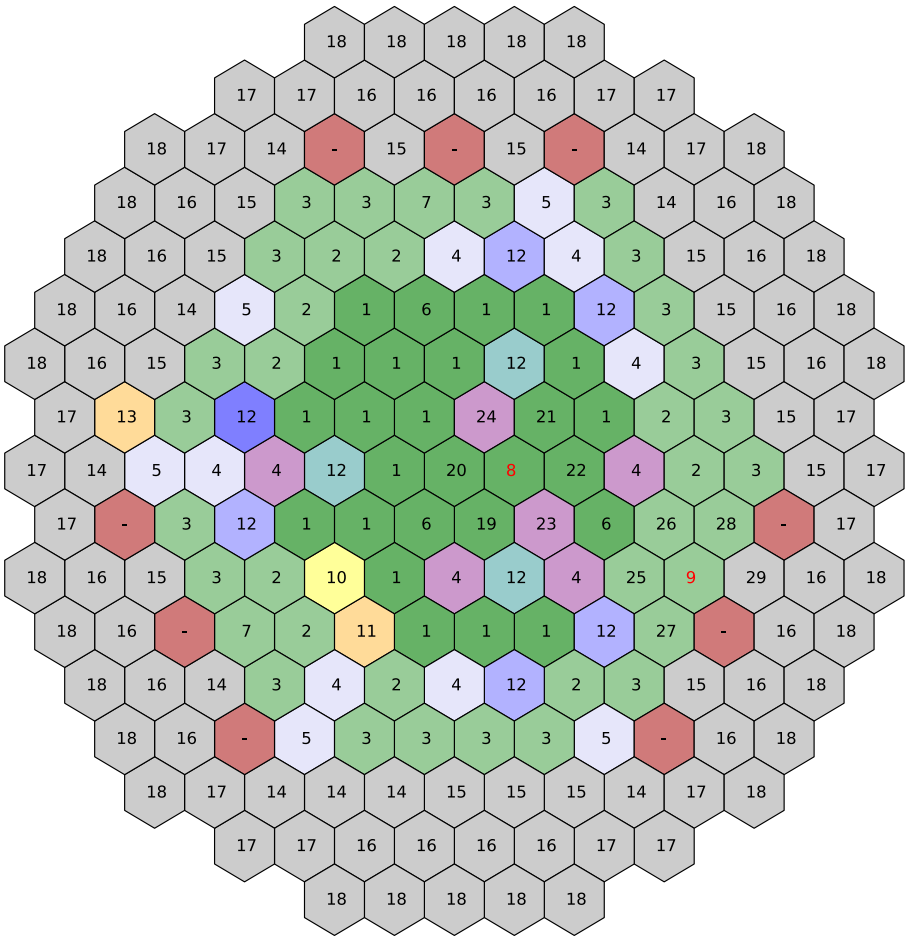

Figure 4.3. Cycle 8C Assembly Channel Locations

The FFTF SAS4A/SASSYS-1 core model also includes the DEFORM-4 oxide fuel and cladding deformation module. The DEFORM-4 module simulates fuel and cladding irradiation and its effect on the physical state of the fuel pin. It accounts for pre-transient steady-state irradiation as well as fuel pin behavior in the transient. The following phenomena are calculated by DEFORM-4:

- As-fabricated porosity migration by vapor transport, which is responsible for the formation of the central hole, and its effect on fuel thermal conductivity
- Grain growth, which affects the fission gas release and fuel creep characteristics
- Fission gas release, which affects the distribution of fuel porosity and fuel swelling
- Fission product swelling, including solid fission products and fission gas bubble swelling
- Irradiation-induced cladding swelling, which affects cladding dimensions and density

Aside from the as-fabricated fuel and cladding dimensions and properties, the most important DEFORM-4 input parameters are for the irradiation history. Since FFTF was a test reactor, it was subject to frequent startups, shutdowns, and power variations. That power and temperature variation could be expected to affect the fuel restructuring and deformation, as well as the size and conductivity of the fuel-cladding gap. All those phenomena are important for predicting fuel temperatures, both in transient and at the pre-transient conditions, which directly feed into the calculations of the Doppler and axial expansion fuel reactivity feedbacks.

Due to the complexity of the FFTF test reactor operation, the entire irradiation history could not be directly modeled in SAS4A/SASSYS-1 and some assumptions and simplifications were required. A simplified treatment has been implemented which assumes that the fuel was mostly irradiated at full-power conditions, with two ramps representing the initial power increase and the final power decrease to the test conditions. The lengths of these ramps were arbitrarily selected to be 10 and 5 days, respectively. Figure 4.4 shows a representative example of the irradiation history, though the inputs varied for each channel and for the different LOFWOS tests. The pre-transient irradiation history was broken up into five steps. Step 1 was used to simulate the initial reactor startup. Step 2 represents the early fuel irradiation in the first 30 days when most fuel restructuring occurs. This step was simulated with smaller time steps than the others to improve accuracy for deformation in fresh fuel. The duration of Step 3 was selected individually for each channel to preserve the total burnup for that channel. The conditions just prior to the test are simulated by a linear reduction from 100% power to the test-specific initial power over 5 days (Step 4), followed by steady state operation for 1 day before the test initiation (Step 5).

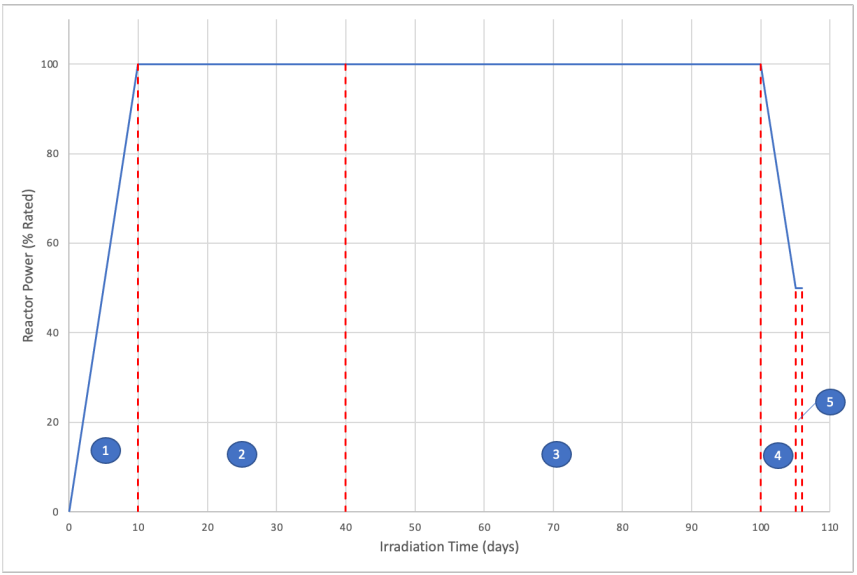

Figure 4.4. Cycle 8C DEFORM-4 Irradiation History

Table 4.5. Cycle 8C SAS4A/SASSYS-1 Core Channel Summary

Channel	Channel Type	Assembly Type	Number of Assemblies
1	Driver Fuel	3.2 Driver	18
2	Driver Fuel	3.1 Driver, Row 5	10
3	Driver Fuel	3.1 Driver, Row 6	20
4	Driver Fuel	4.1/4.2 Driver, Rows 2-5	10
5	Driver Fuel	4.1 Driver, Row 6	5
6	Driver Fuel	3.2 Driver (with slow PIOTA)	3
7	Driver Fuel	3.1 Driver, Row 6 (with slow PIOTA)	2
8	Driver Fuel	3.2 Driver (with fast PIOTA)	1
9	Driver Fuel	3.1 Driver, Row 6 (with fast PIOTA)	1
10	Reflector	Materials Open Test Assembly	1
11	Reflector	In-Core Shim Assembly	1
12	Control	Control/Safety Rod	9
13	Reflector	Fracture Mechanics Assembly	1
14	Reflector	Row 7 Reflector, REFL7	10
15	Reflector	Row 7 Reflector, REFL72	15
16	Reflector	Row 8A Reflector, REFL8A	24
17	Reflector	Row 8B Reflector, REFL8B	18
18	Reflector	Row 9 Reflector, REFL9	30
19-22	Driver Fuel	3.2 Driver (near Channel 8 PIOTA)	4
23-24	Driver Fuel	4.1/4.2 Driver, Rows 2-5 (near Channel 8 PIOTA)	2
25-26	Driver Fuel	3.1 Driver, Row 5 (near Channel 9 PIOTA)	2
27-28	Driver Fuel	3.1 Driver, Row 6 (near Channel 9 PIOTA)	2
29	Reflector	Row 7 Reflector, REFL7 (near Channel 9 PIOTA)	1

4.3 Cycle 8A Core Model

The FFTF Cycle 8A core model used to simulate the individual reactivity feedback tests consists of 19 channels created from the three base channel types described in Section 4.1. Variations of the three base channel models were created to assign initial flow rates as shown in Figure 3.7, model the different driver fuel orifice regions as described in Section 4.1.1, enable channel-to-channel heat transfer, assign reactivity feedback and decay heat parameters, and separate PIOTA assemblies into individual channels. Table 4.6 summarizes the core channels and Figure 4.5 illustrates which channel each assembly was assigned to.

Similar to the Cycle 8C core model discussed in Section 4.2, the channel-to-channel heat transfer model in SAS4A/SASSYS-1 was activated in the Cycle 8A core model to model heat transfer through the following paths:

- Between PIOTA assemblies and their neighbors
- Between PIOTA neighbors (for example, between Channels 2 and 3)
- Between PIOTA neighbors and their neighbors
- Between all reflector assemblies

Inputs characterizing heat transfer perimeter times the heat transfer coefficient for each pair of channels participating in the heat transfer were entered into the model.

Similar to the Cycle 8C core model discussed in Section 4.2, the Cycle 8A core model also includes the DEFORM-4 oxide fuel and cladding deformation module. The input for pre-transient irradiation of fuel was calculated based on burnup data for Cycle 8A assemblies.

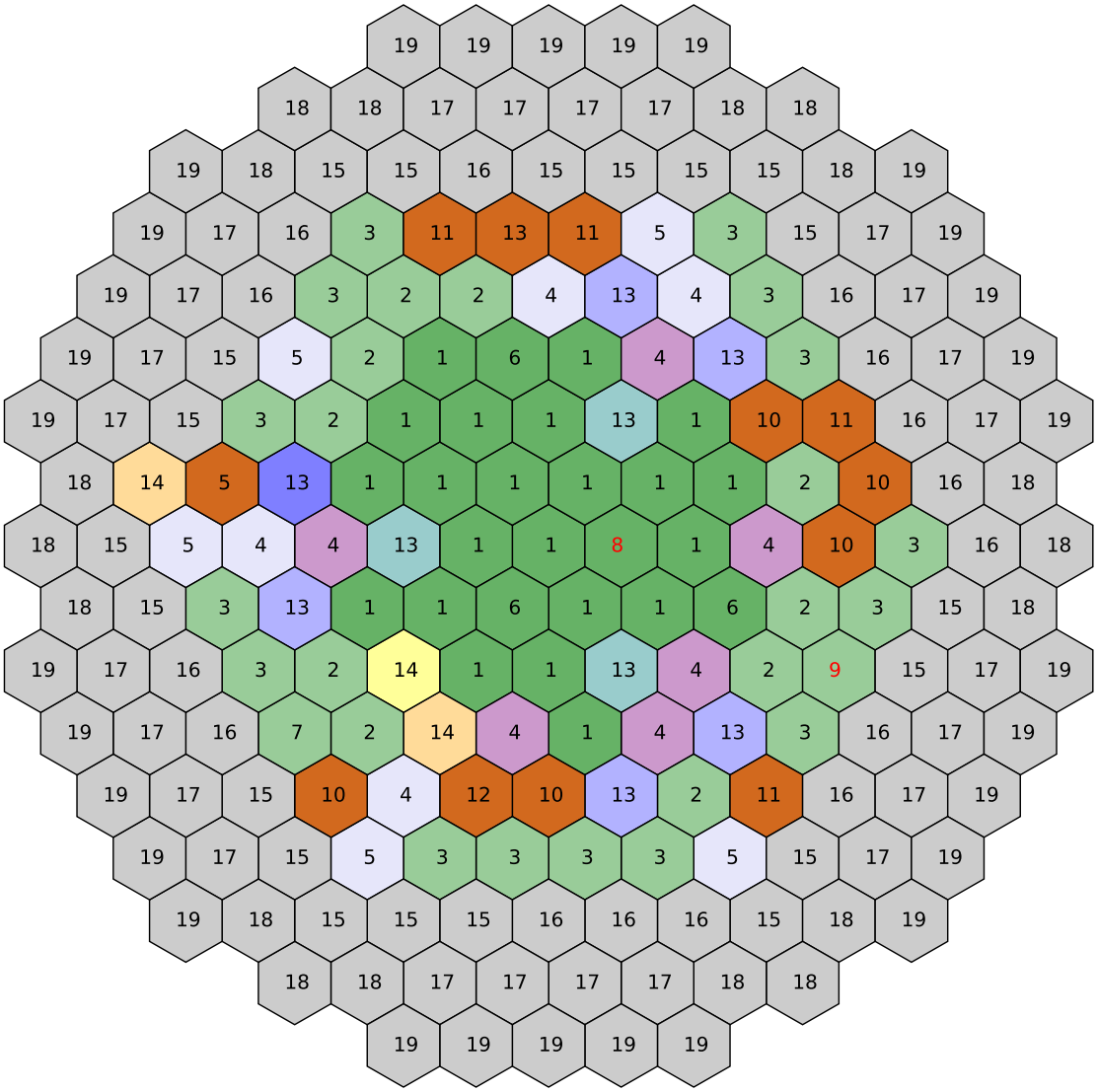

Figure 4.5. Cycle 8A Assembly Channel Locations

Table 4.6. Cycle 8A SAS4A/SASSYS-1 Core Channel Summary

Channel	Channel Type	Assembly Type	Number of Assemblies
1	Driver Fuel	3.2 Driver	22
2	Driver Fuel	3.1 Driver, Row 5	10
3	Driver Fuel	3.1 Driver, Row 6	15
4	Driver Fuel	4.1/4.2 Driver, Rows 2-5	10
5	Driver Fuel	4.1 Driver, Row 6	6
6	Driver Fuel	3.2 Driver	3
7	Driver Fuel	3.1 Driver, Row 6	1
8	Driver Fuel	3.2 Driver (with fast PIOTA)	1
9	Driver Fuel	3.1 Driver, Row 6 (with fast PIOTA)	1
10	Fueled Test	ACO and FO	5
11	Fueled Test	PO	4
12	Fueled Test	Carbide Fuel Test (FC)	1
13	Control	Control/Safety Rod	10
14	Reflector	ICSA, MOTA, FMA	3
15	Reflector	Row 7 Reflector, REFL7	20
16	Reflector	Row 7 Reflector, REFL72	15
17	Reflector	Row 8A Reflector, REFL8A	24
18	Reflector	Row 8B Reflector, REFL8B	18
19	Reflector	Row 9 Reflector, REFL9	30

4.4 Point Kinetics, Decay Heat, and Reactivity Feedback

The point kinetics, decay heat, and reactivity feedback models built into SAS4A/SASSYS-1 are used to calculate transient core power during the tests. Input parameters for these models have been calculated for the Cycle 8C core to predict power during the LOFWOS tests. Models for the LOFWOS tests that use measured power as a transient boundary condition have also been developed to assess test predictions independent of the accuracy of the power predictions. Input parameters for point kinetics and reactivity feedback models have also been calculated for the Cycle 8A core. The Cycle 8A core model uses measured power as a transient boundary condition, but SAS4A/SASSYS-1 still calculates and prints each individual reactivity feedback and the total reactivity even though the point kinetics equations are not used and the effect of reactivity on power is ignored. The decay heat model is not used for Cycle 8A since it cannot be used in SAS4A/SASSYS-1 when power is specified as a boundary condition.

Coefficients for the point kinetics, decay heat, and reactivity feedback models were previously calculated for the Cycle 8C core to support Argonne's analysis performed under the IAEA Coordinated Research Project. Coefficients for the point kinetics and reactivity feedback models (but not decay heat) were also calculated for the Cycle 8A core. The results of these neutronics calculations were also used to construct the core radial power distribution and axial power profiles for the driver fuel channels. Power in non-fueled channels was assumed to be axially uniform.

The point kinetics equations, which assume a time-independent spatial power distribution within the reactor core, are solved using the second-order accurate methods available in SAS4A/SASSYS-1. Table 4.7 lists the point kinetics parameters for the Cycle 8C and Cycle 8A cores.

Table 4.7. Point Kinetics Parameters

Group	Cycle 8C		Cycle 8A	
	Delayed Neutron Fraction, β_i	Decay Constant, λ_i (s^{-1})	Delayed Neutron Fraction, β_i	Decay Constant, λ_i (s^{-1})
1	8.314E-05	1.335E-02	8.307E-05	1.335E-02
2	5.885E-04	3.098E-02	5.875E-04	3.099E-02
3	4.901E-04	1.168E-01	4.901E-04	1.168E-01
4	1.106E-03	3.060E-01	1.107E-03	3.061E-01
5	6.360E-04	8.803E-01	6.367E-04	8.804E-01
6	2.277E-04	2.913E+00	2.281E-04	2.913E+00
β_{eff}	3.131E-03		3.132E-03	
Prompt Neutron Lifetime, Λ (s)	5.278E-07		4.960E-07	

Two decay heat curves were generated using ORIGEN-2 [7] and the power history prior to Cycle 8C. The curves were fitted with up to six-group exponential terms to be implemented into the SAS4A/SASSYS-1 model. The first curve represents the core average decay heat and was applied to all channels except for Channel 8. A channel-specific second decay heat curve was used for Channel 8 to improve the comparison to measured data in this PIOTA assembly because it had a significantly lower burnup than the majority of the core assemblies. Table 4.8 lists the decay heat parameters for the Cycle 8C core. The Cycle 8A core used the SAS4A/SASSYS-1 built-in decay heat curve for Pu-239 as a placeholder input, though it was not used by the code because the decay heat model was not turned on.

Table 4.8. Cycle 8C Decay Heat Parameters

Group	Curve 1 (Channels 1-7, 9, 19-28)		Curve 2 (Channel 8)	
	Precursor Concentration	Decay Constant λ_i (s^{-1})	Precursor Concentration	Decay Constant λ_i (s^{-1})
1	4.199E-03	7.682E-01	1.485E-02	1.321E-01
2	7.622E-03	1.289E-01	9.316E-03	2.219E-02
3	9.952E-03	2.504E-02	7.531E-03	5.285E-03
4	9.589E-03	6.113E-03	1.860E-02	3.480E-04
5	1.424E-02	3.787E-04	-	-
6	6.983E-03	3.012E-04	-	-

The following reactivity feedbacks were included in the model and are discussed in the following sections:

- Fuel Doppler
- Fuel axial expansion
- Cladding density
- Coolant voiding
- Control rod driveline expansion
- Core radial expansion
- GEM gas expansion

4.4.1 Channel-Dependent Reactivity Feedbacks

The fuel Doppler feedback is calculated from the average fuel temperature change at each axial segment. A 1/T dependence is assumed for the change in reactivity. Input is entered for two Doppler coefficients, one with coolant present and the other with coolant voided. SAS4A/SASSYS-1 linearly interpolates between these two values during the transient based on the sodium density to calculate the Doppler feedback.

The calculations for the reactivity feedbacks due to fuel, cladding, and coolant changes are similar to each other. The coolant feedback is calculated at all axial zones for all channels, while the fuel and cladding feedbacks are calculated only in the core axial zone and only for fueled channels. The cladding feedback represents the feedback from both cladding and structure assuming that the temperature changes in the cladding and structure are similar during a transient.

The control channel described in Section 4.1.4 simulates the control rod absorbers as fully inserted. However, when the control rod absorbers were partially or fully withdrawn, those assemblies were filled with some amount of sodium coolant. By simulating the control rod as fully inserted, the amount of sodium within the control assembly was not correctly predicted. This discrepancy affects the amount of reactivity feedback from coolant density changes. To more accurately account for this effect, the input for the coolant density feedback for the control channel was scaled to preserve the total coolant worth from neutronics calculations, which were calculated based on the actual position of the control rods. For the LOFWOS tests, the control rod positions in LOFWOS Test #13 were used and assumed to apply for the other LOFWOS tests. For the Cycle 8A individual reactivity feedback tests, the control rod positions from Step 2B were used.

Core axial expansion is calculated based on fuel and cladding density changes. As densities decrease, the fuel and cladding expand and push the mass higher up. The displaced mass in each pin is relocated above the fuel to conserve mass. The change in mass at each segment is then converted to a reactivity change based on user input fuel and cladding axial worth distributions. Since fuel has a higher worth in the center of the core, axial expansion will move the fuel from the center of the core to a region of low worth at the top of the core, introducing a negative reactivity feedback. With the fuel and cladding deformation (DEFORM-4) model activated, that model will calculate the axial expansion of the fuel and cladding. This expansion is then converted to the reactivity feedback based on the user input of fuel and cladding worth.

Table 4.9 and Table 4.10 list the reactivity worth for the integrated channel-dependent feedback effects in Cycle 8C and Cycle 8A, respectively. Note that these tables only provide the total reactivity worth over each channel, accounting for the number of assemblies represented by the channel. This illustrates which channels are the greatest contributors to the different feedback effects.

Table 4.9. Cycle 8C Channel-Dependent Reactivity Feedback Totals

Channel	Number of Assemblies	Void ($)	Fuel ($)	Clad ($)	Doppler (T Δk/ΔT)
1	18	2.356E-01	43.891	-3.326E+00	-1.918E-03
2	10	-1.611E-01	18.653	-5.238E-01	-5.808E-04
3	20	-8.856E-01	22.869	1.240E+00	-1.049E-03
4	10	-3.201E-02	22.128	-1.028E+00	-7.364E-04
5	5	-2.140E-01	5.237	3.259E-01	-2.243E-04
6	3	5.999E-02	7.719	-6.550E-01	-3.079E-04
7	2	-1.097E-01	2.739	1.478E-01	-1.224E-04
8	1	4.033E-02	3.551	-3.342E-01	-1.360E-04
9	1	-5.421E-02	1.388	7.563E-02	-5.937E-05
10	1	-5.681E-03	0.0	-4.290E-02	0.0
11	1	1.303E-04	0.0	-1.063E-01	0.0
12	9	-1.104E+00	0.0	5.511E-01	0.0
13	1	-6.291E-03	0.0	1.771E-01	0.0
14	10	-3.738E-02	0.0	8.896E-01	0.0
15	15	-6.546E-02	0.0	1.458E+00	0.0
16	24	-2.915E-02	0.0	1.103E+00	0.0
17	18	-3.176E-02	0.0	1.085E+00	0.0
18	30	-1.742E-02	0.0	6.341E-01	0.0
19	1	1.305E-02	2.438	-1.848E-01	-1.066E-04
20	1	1.303E-02	2.438	-1.848E-01	-1.066E-04
21	1	1.306E-02	2.438	-1.848E-01	-1.066E-04
22	1	1.307E-02	2.438	-1.848E-01	-1.066E-04
23	1	-3.194E-03	2.213	-1.028E-01	-7.364E-05
24	1	-3.206E-03	2.213	-1.028E-01	-7.364E-05
25	1	-1.613E-02	1.865	-5.238E-02	-5.808E-05
26	1	-1.611E-02	1.865	-5.238E-02	-5.808E-05
27	1	-4.427E-02	1.143	6.199E-02	-5.244E-05
28	1	-4.426E-02	1.143	6.199E-02	-5.244E-05
29	1	-3.735E-03	0.0	8.896E-02	0.0
Reactor Totals	190	-2.497	148.372	0.835	-5.929E-03

Table 4.10. Cycle 8A Channel-Dependent Reactivity Feedback Totals

Channel	Number of Assemblies	Void ($)	Fuel ($)	Clad ($)	Doppler (T Δk/ΔT)
1	22	2.955E-01	58.344	-4.394E+00	-2.487E-03
2	10	-1.684E-01	19.650	-4.488E-01	-5.759E-04
3	15	-5.823E-01	17.286	7.830E-01	-7.698E-04
4	10	-1.037E-01	19.963	-5.515E-01	-6.356E-04
5	6	-2.331E-01	6.168	3.607E-01	-2.575E-04
6	3	4.513E-02	7.870	-6.124E-01	-3.078E-04
7	1	-4.566E-02	1.382	4.761E-02	-6.460E-05
8	1	4.129E-02	3.226	-3.305E-01	-1.325E-04
9	1	-4.574E-02	1.300	5.780E-02	-5.866E-05
10	5	-1.439E-01	6.637	9.917E-02	-2.541E-04
11	4	-8.966E-02	3.960	1.141E-01	-2.058E-04
12	1	2.744E-03	0.0	-9.313E-02	0.0
13	10	-9.058E-01	0.0	6.675E-01	0.0
14	3	-1.596E-02	0.0	-1.057E-01	0.0
15	20	-7.590E-02	0.0	2.007E+00	0.0
16	15	-6.419E-02	0.0	1.609E+00	0.0
17	24	-1.533E-02	0.0	8.238E-01	0.0
18	18	-1.981E-02	0.0	7.266E-01	0.0
19	30	-1.175E-02	0.0	4.491E-01	0.0
Reactor Totals	199	-2.137	145.785	1.209	-5.750E-03

4.4.2 Control Rod Driveline Expansion

As the control rod drivelines heat up and expand, the control rods are pushed further into the core, thus producing a negative reactivity feedback. Conversely, cooling drivelines will contract and withdraw the control rods from the core, producing a positive reactivity feedback. SAS4A/SASSYS-1 calculates this reactivity using the following equations:

$$\Delta\rho_{CR} = A_{CRDEX}\Delta z + B_{CRDEX}\Delta z^2$$

$$\Delta z = \alpha\, L\, \Delta T$$

where the coefficients A_{CRDEX} and B_{CRDEX} are obtained using a quadratic fit of the control rod worth curve, Δz is the amount of driveline expansion, α is the thermal expansion coefficient of the drivelines, L is the nominal length of the drivelines washed by core outlet sodium, and ΔT is the temperature change from steady-state conditions experienced by the drivelines.

The driveline expansion reactivity coefficients were calculated using the control rod positions from LOFWOS Test #13 for the Cycle 8C model, and the control rod position from Step 2B from the Cycle 8A model. The entire length of the drivelines in the outlet plenum was included in the analysis as a length subject to expansion. Table 4.11 provides the input parameter values for the control rod driveline expansion model.

Table 4.11. Control Rod Driveline Expansion Parameters

Parameter	Description	Cycle 8C Value	Cycle 8A Value
A_{CRDEX}	Driveline expansion reactivity coefficients	-31.79 \$/m	-24.39 \$/m
B_{CRDEX}		-46.44 \$/m^2	-32.41 \$/m^2
α	Driveline thermal expansion coefficient	2.0E-05 1/K	2.0E-05 1/K
L	Nominal driveline length	6.764 m	6.764 m

4.4.3 Core Radial Expansion

The SAS4A/SASSYS-1 FFTF-specific detailed radial expansion model was implemented in both the Cycle 8C and Cycle 8A models to simulate a limited free bow type of core restraint system which accounts for the effects of the restraint mechanisms on the core radial shape at steady-state and during a transient. The following components are included in the detailed radial expansion model:

- Grid plate with assembly nozzle clearances
- Above core load pads (ACLP)
- Load pads at the top of the assemblies (TLP)
- Restraint ring (RR) at the top load pad location, which is attached to the core barrel

During both the steady-state and transient calculations, the assemblies are subjected to bending moments related to temperature differences on opposing sides of the hex can. The detailed radial expansion model uses these bending moments to solve beam equations for the assemblies and, depending on the contact points and modes at any of the core restraint locations, calculates the radial shape of the core along the assembly height. Then, this shape is converted into a reactivity feedback using the core radial expansion coefficient of reactivity and the axial power shape.

Most of the input parameters for the FFTF-specific detailed radial expansion model are available in Figure 2.11 and from additional assembly dimensions provided in Reference 1. The remaining input parameters were based on SAS4A/SASSYS-1 suggested values or values from the development of the FFTF-specific core restraint model. The radial expansion coefficient of reactivity provided by the neutronics calculations was -333.64 $/m for Cycle 8C and -321.17 $/m for Cycle 8A.

Simulations were also performed for Cycle 8A using the SAS4A/SASSYS-1 simple radial expansion model. This model assumes straight-line expansion between the core grid plate and the above core load pads to determine the average expansion of the core at the core midplane. The simplified radial expansion model is governed by the following equation:

$$\Delta\rho_{radial} = C_{re}\left[\Delta T_{in} + \frac{XMC}{XAC}(\Delta T_{SLP} - \Delta T_{in})\right]$$

where C_{re} is the radial expansion feedback coefficient, ΔT_{in} is the temperature change of the core grid plate at the core inlet, ΔT_{SLP} is the average structure temperature change at the elevation of the above core load pads, and $\frac{XMC}{XAC}$ is the height of the core midplane relative to the spacer buttons.

For the types of individual reactivity feedback tests the simple radial expansion model was used for, it was assumed that radial expansion would be determined solely by grid plate expansion, meaning the ratio $\frac{XMC}{XAC}$ is zero. The radial expansion coefficient, C_{re}, provided by the neutronics calculations was -0.003776 $/K.

4.4.4 GEM Reactivity

Reactivity feedback from the GEM assemblies was implemented into the SAS4A/SASSYS-1 model using the control system for Cycle 8C. GEM assemblies were not present in the Cycle 8A core. The control system allows a user to select any number of plant variables for use as measured quantities. These measured signals can then be processed by a user-defined network of mathematical blocks that implement an equation. Finally, the results of the signals are output to drive various parts of the simulation. In this case, an additional reactivity term is calculated with the control system and gets added to the other reactivity feedback effects at each time step.

The GEM reactivity is a major contributor to negative reactivity during the LOFWOS tests and depends on the gas-sodium interface level in the GEM assemblies. As the GEM sodium level decreases from its initial level during the loss of flow transient, negative reactivity is inserted. Once the sodium level is below the level of the active core, the maximum amount of negative reactivity is inserted at about -1.4$ since any further decrease in the sodium level does not significantly affect the increase in neutron leakage. The relationship between GEM sodium level and reactivity is shown in Figure 4.6. This data was determined by neutronics calculations provided as supplemental information for the FFTF IAEA CRP [1].

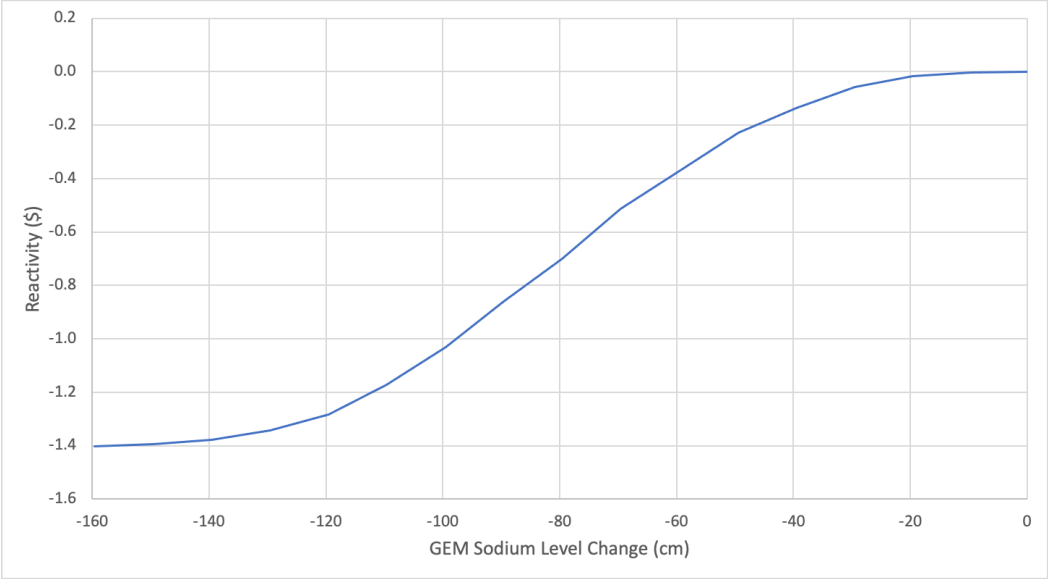

Figure 4.6. GEM Reactivity vs. GEM Sodium Level Change

An equation for the GEM sodium level L can be solved for using the following relationship between P_{GEM} (pressure of argon gas in the GEM) and P_{inlet} (inlet plenum pressure):

$$P_{inlet} = P_{GEM} + \rho g L + \rho g \Delta h$$

where Δh is the distance between the inlet plenum and the bottom of the GEM (the top of the inlet nozzle), ρ is sodium density, and g is gravitational acceleration. P_{GEM} can be expressed by the ideal gas law using the dimensions of the GEM expansion volume, the initial GEM sodium level as shown in Table 3.2, and the temperature of the GEM argon gas, T_{Ar}. A constant sodium density consistent with the core inlet temperature was assumed since the core inlet temperature does not vary much during the transient. Solving the above equation for L is not fully shown here, but results in the following equation for GEM sodium level which was programmed into the control system model:

$$L = \frac{P_{inlet} + 11538.8 - \sqrt{(P_{inlet} + 11538.8)^2 - 4 \times 8590.9\,(2.65 P_{inlet} - 628.9 T_{Ar} - 29751.8}}{2 \times 8590.9}$$

Because the argon temperature inside the GEM quickly equilibrates to its surrounding temperature, T_{Ar} was approximated by averaging the outlet temperatures of channels which surround the GEM assemblies. These channel outlet temperatures as well as P_{inlet} are available as measured signals from the control system and are used to calculate the GEM sodium level and the change in this level compared to the steady-state value. The interface level change is then converted to a reactivity using a user-input table based on the data provided from the neutronics calculations that is illustrated in Figure 4.6. The reactivity is fed back to the neutronics solver via a control signal and incorporated into the net reactivity at each time step.

4.5 Heat Transport System Model

The LOFWOS tests utilized the detailed heat transport system model capabilities of SAS4A/SASSYS-1 described in this section. The Cycle 8A individual reactivity feedback tests were simulated with a core model only since their analysis is focused on the core reactivity feedbacks. Inputs for the core inlet temperature and flow rate were directly specified as boundary conditions using the measured data described in Section 3.2.2.

The SAS4A/SASSYS-1 PRIMAR-4 module simulates the thermal hydraulics of the primary and intermediate heat transport system. A simplified example of PRIMAR-4 geometry is illustrated in Figure 4.7 [6]. In a PRIMAR-4 model, compressible volumes (CVs) are zero-dimensional volumes used to model larger volumes of coolant such as inlet and outlet plena and pools. CVs are characterized by their pressure, temperature, elevation, and volume.

Compressible volumes are connected by liquid segments, which are composed of one or more elements. Elements are modeled by one-dimensional, incompressible, single-phase flow and can be used to model pipes, valves, heat exchangers, steam generators, and more. Elements are characterized by their pressure, temperature, elevation, and mass flow rate.

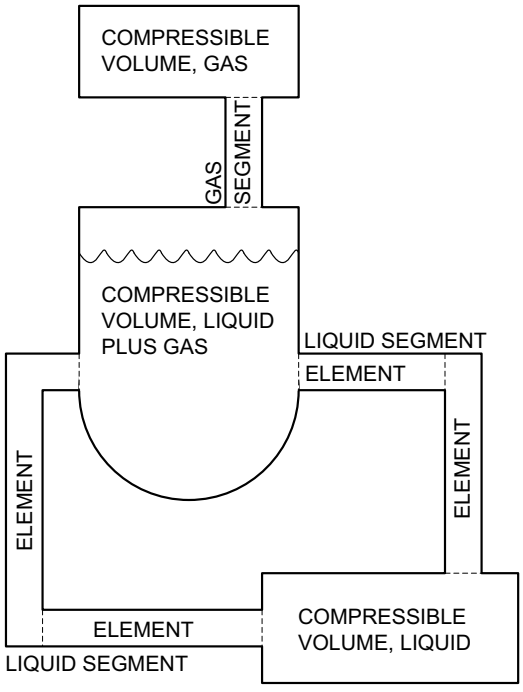

Figure 4.7. PRIMAR-4 Example Geometry

4.5.1 Primary System Loops

The PRIMAR-4 model of the primary system represents the components within the reactor vessel and the three primary heat transport loops. Figure 4.8 illustrates the model of the components within the reactor vessel, which includes the inlet plenum, core support structure, core, bypass flow paths, and outlet plenum.

Sodium discharged from the three primary loop inlet pipes flows into CV2, the inlet plenum. From there, the sodium flows into CV1, which represents the core basket and annular plenum within the core support structure. CV1 has three outlets: Segments 1, 2, and 10. Segment 1 comprises the core channels presented in Section 4.2 while Segment 2 represents the sodium flowing through the shields and along the core restraint system, as well as all sodium leakage between assemblies. Segment 10 represents the sodium that leaks past the assembly inlet nozzles from the core basket into the low-pressure plenum at the bottom of the core support structure to the peripheral plenum, CV8. From CV8, sodium flows out either through the annular in-vessel storage region surrounding the core barrel or into the bypass vessel cooling region.

Figures 4.9 - 4.11 illustrate the primary loop model. Elements 3-14, 15-26, and 27-38 represent primary loops 1, 2, and 3, respectively. Select parameters for the CVs, segments, and elements in the primary heat transport system model are provided in Tables 4.12 - 4.14.

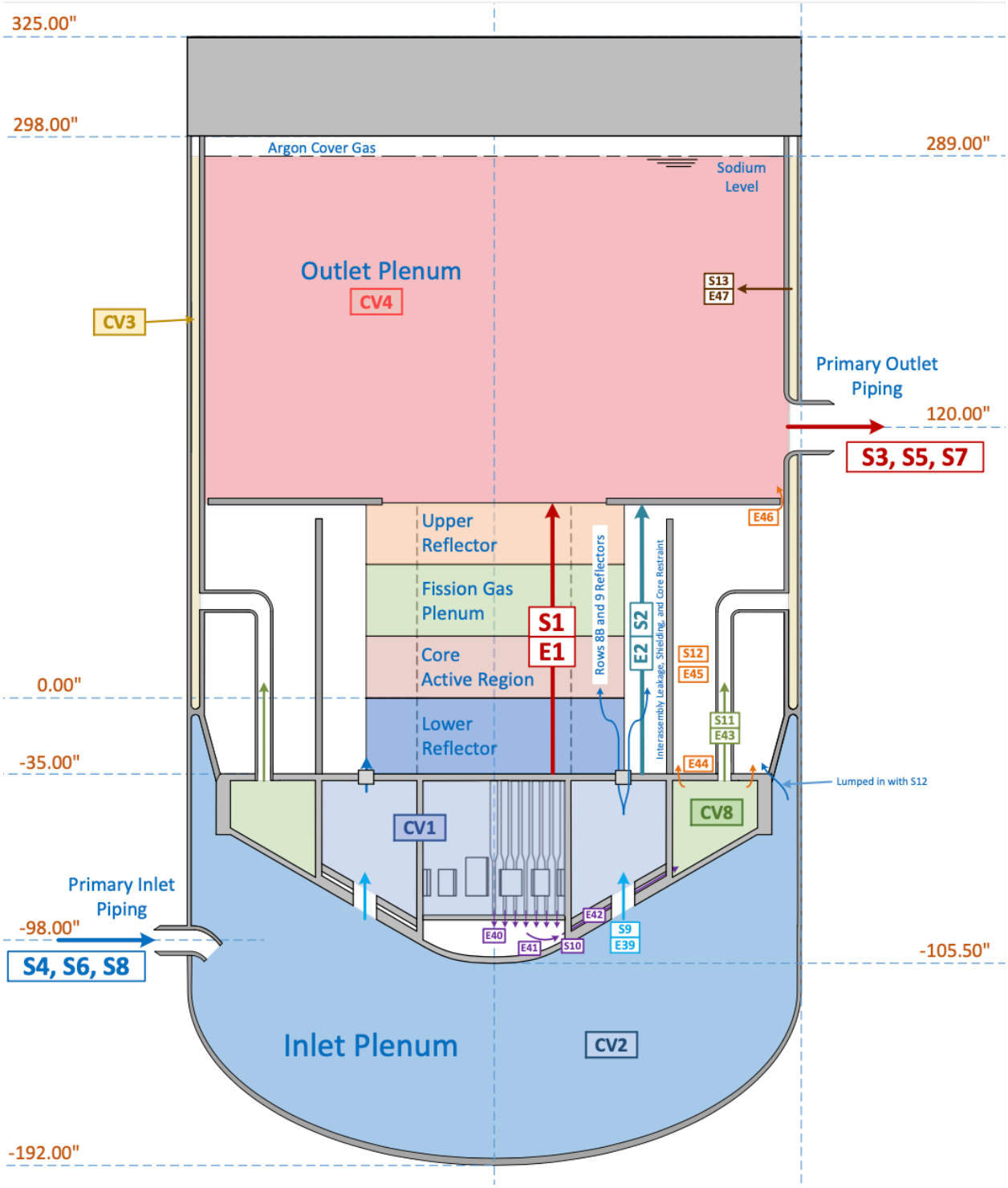

Figure 4.8. Reactor Vessel PRIMAR-4 Model

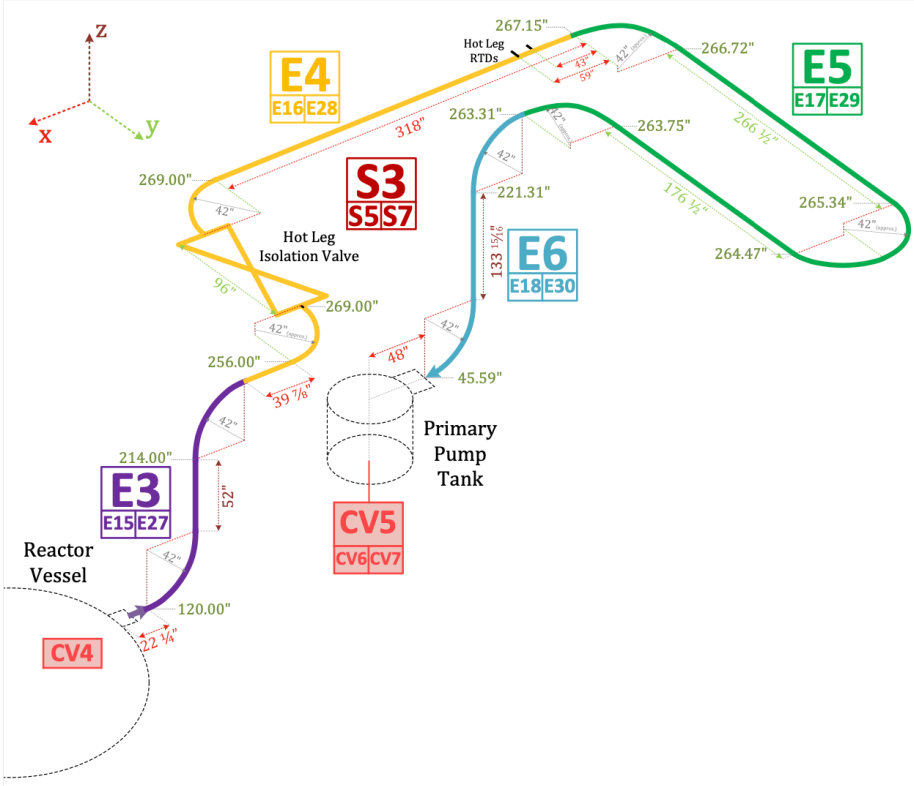

Figure 4.9. PRIMAR-4 Model: Reactor Vessel Outlet to Pump Inlet Primary Loop Piping

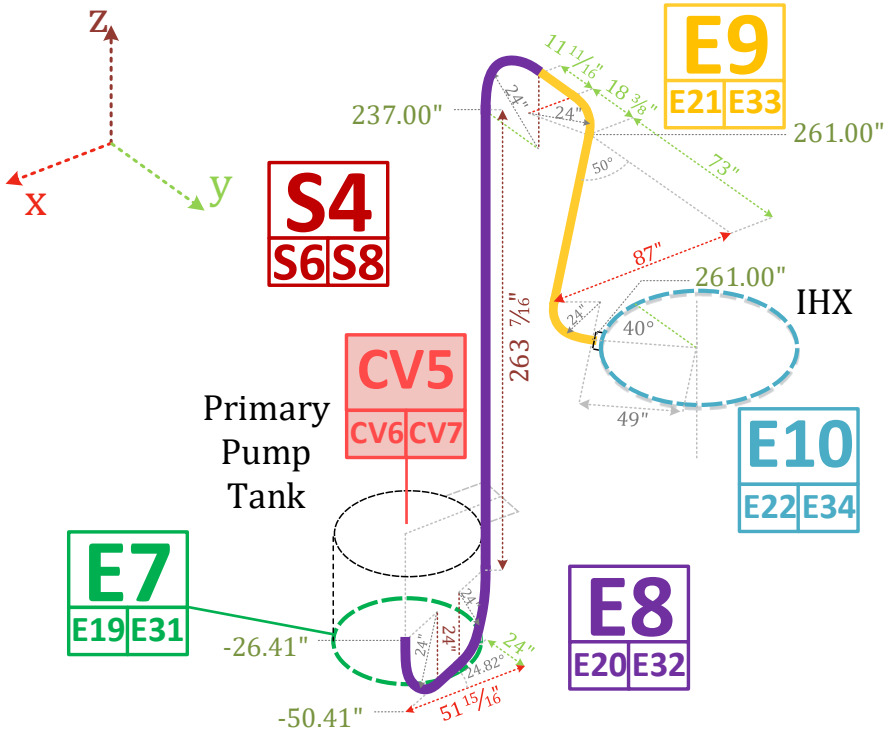

Figure 4.10. PRIMAR-4 Model: Pump Outlet to IHX Inlet Primary Loop Piping

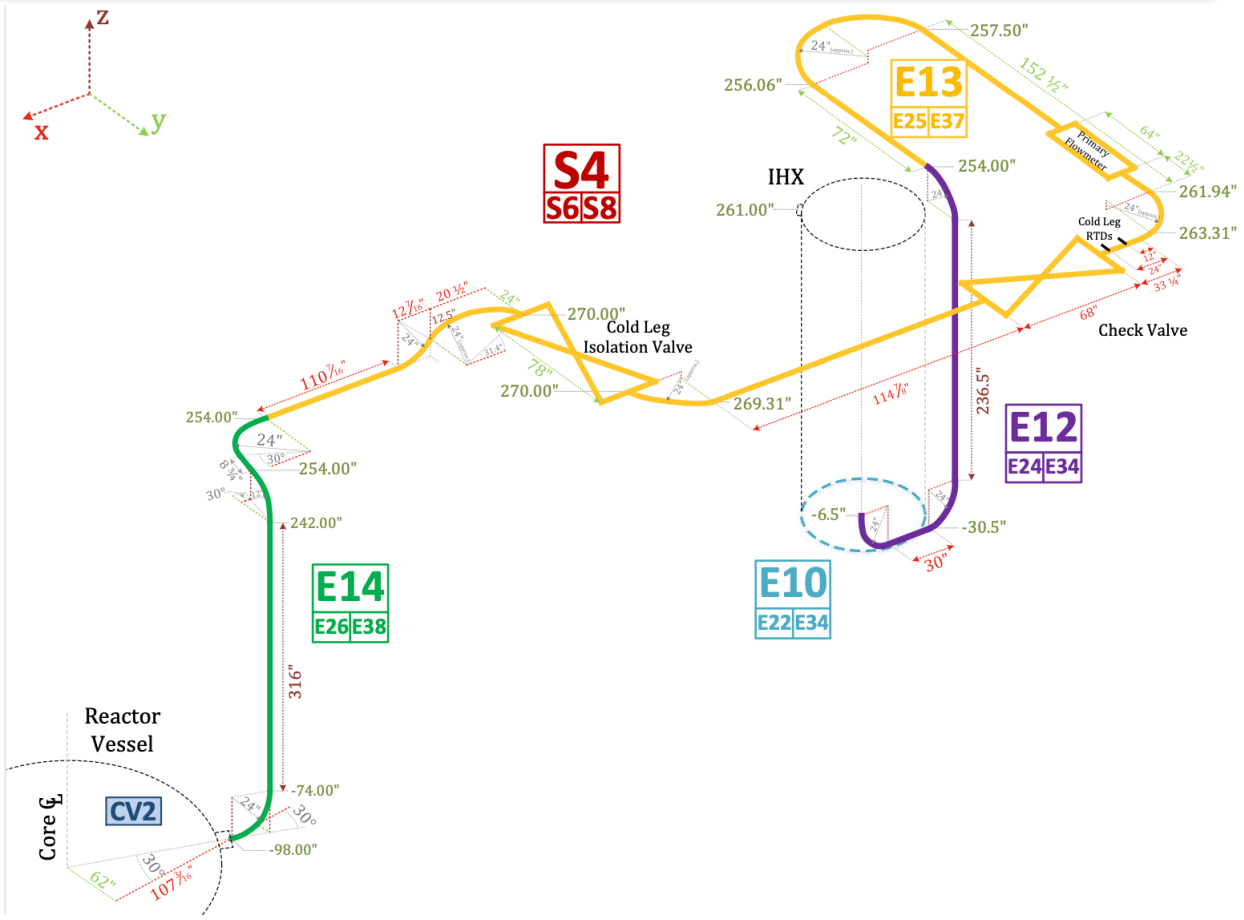

Figure 4.11. PRIMAR-4 Model: IHX Outlet to Reactor Vessel Primary Loop Piping

Table 4.12. Primary System Compressible Volumes

CV#	Description	Sodium Volume (m^3)	Gas Volume (m^3)	Total Volume (m^3)
1	Core Basket and Annular Plenum	10.85	0.0	10.85
2	Inlet Plenum	66.15	0.0	66.15
3	Bypass Vessel Cooling	4.5	0.14	4.64
4	Outlet Plenum	119.13	6.59	125.72
5-7	Primary Loops #1-3 Pump Tanks	2.97	5.0	7.97
8	Peripheral Plenum	7.78	0.0	7.78

Table 4.13. Primary System Segments

Segment #	Description	Mass Flow Rate (kg/s)		
		Test #10	Test #11	Test #12
1	Core Channels	2062.9	2063.0	2038.2
2	Inter-assembly leakage, shielding, core restraint	0.066	0.066	0.065
3	Reactor Vessel to Primary Pump #1	747.0	742.4	738.6
4	Primary Pump #1 to Reactor Vessel	747.0	742.4	738.6
5	Reactor Vessel to Primary Pump #2	730.7	725.0	723.7
6	Primary Pump #2 to Reactor Vessel	730.7	725.0	723.7
7	Reactor Vessel to Primary Pump #3	733.8	744.2	722.8
8	Primary Pump #3 to Reactor Vessel	733.8	744.2	722.8
9	Inlet Plenum to Annular Plenum	2211.5	2211.7	2185.1
10	Core Barrel Leakage to Peripheral Plenum	148.5	148.6	146.8
11	Peripheral Plenum to Bypass Vessel Cooling	114.5	114.5	113.1
12	Peripheral Plenum Leakage to Outlet Plenum	34.1	34.1	33.7
13	Bypass Vessel Cooling to Outlet Plenum	114.5	114.5	113.1

Table 4.14. Primary System Elements

Element #	Description	Elevations (m)		Hydraulic Diameter (m)	Flow Area (m^2)	Length (m)
		Inlet	Outlet			
1	Core Channels	-0.861	2.652	-[a]	-[a]	3.513
2	Inter-assembly leakage, shielding, core restraint	-0.861	2.652	1.000	0.1000	3.513
3, 15, 27	Reactor Vessel Outlet Pipe	3.084	6.538	0.692	0.3763	4.672
4, 16, 28	Hot Leg Piping	6.538	6.821	0.692	0.3763	14.880
5, 17, 29	Hot Leg Piping	6.821	6.724	0.692	0.3763	17.955
6, 18, 30	Pump Inlet	6.724	1.194	0.692	0.3763	6.754
7, 19, 31	Pump	1.194	-0.635	0.692	0.3763	1.829
8, 20, 32	Pump Outlet, Cold Leg Piping	-0.635	6.665	0.387	0.1178	10.174
9, 21, 33	IHX Inlet	6.665	7.675	0.387	0.1178	5.681
10, 22, 34	IHX Shell Side	7.675	3.319	0.039	1.0944	4.356
11, 23, 35	IHX Outlet	3.319	-0.130	0.277	0.8530	3.506
12, 24, 36	Cold Leg Piping	-0.130	6.487	0.387	0.1178	9.642
13, 25, 37	Cold Leg Piping	6.487	6.487	0.387	0.1178	21.245
14, 26, 38	Cold Leg Piping	6.487	-2.454	0.387	0.1178	10.323
39	Inlet Plenum to Annular Plenum	-2.111	-1.954	0.406	1.5566	0.156
40	Core Barrel Leakage to Low-Pressure Plenum	-2.111	-2.200	0.001	0.0116	0.089
41	Low-Pressure Plenum	-2.200	-2.377	1.000	0.3889	1.291
42	Low-Pressure Plenum to Peripheral Plenum	-2.377	-1.681	0.076	0.0547	0.940
43	Peripheral Plenum to Bypass Vessel Cooling	-0.930	1.344	0.152	0.0547	2.273
44	Peripheral Plenum to In-Vessel Storage	-0.930	-0.853	1.000	0.0500	0.076
45	In-Vessel Storage	-0.853	2.601	1.000	0.1000	3.454
46	In-Vessel Storage to Outlet Plenum	2.601	2.652	1.000	0.0500	0.051
47	Bypass Vessel Cooling to Outlet Plenum	5.014	5.014	1.000	0.1000	0.010

[a] - Geometry for Element 1 is defined by the core channel models

4.5.2 Intermediate Heat Exchanger

The three FFTF intermediate heat exchangers were modeled using the SAS4A/SASSYS-1 detailed IHX model, which represents a shell and tube heat exchanger. Figure 4.12 illustrates the components of the IHX model in the PRIMAR-4 model. The primary side of each IHX is represented by two elements. The first is for the shell-side coolant of the IHX within the active heat transfer region. The second is for the annular outlet surrounding the bottom of the IHX tubes and the lower secondary-side inlet plenum. Primary sodium then flowed into the primary-side cold leg piping. Sodium surrounding the IHX tube bundle below the active heat transfer region was neglected from the model as the outlet from the tube bundle was higher up, which led to stagnated primary-side sodium in this region.

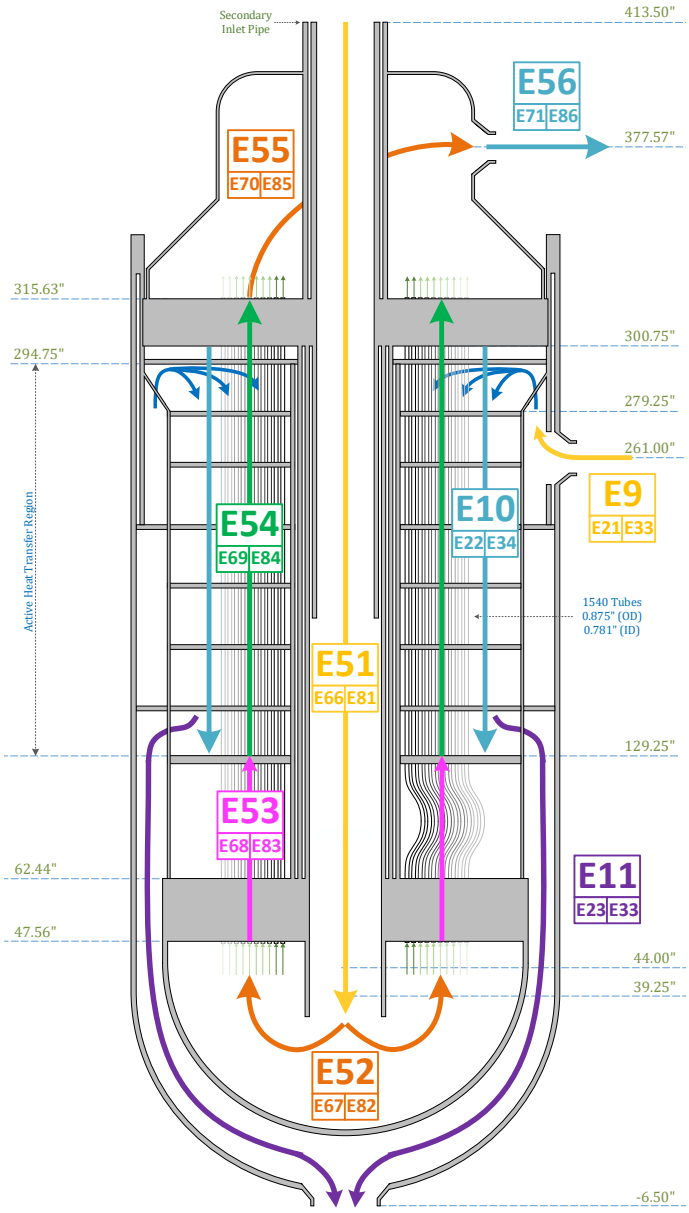

Figure 4.12. PRIMAR-4 Model: Intermediate Heat Exchangers

4.5.3 Secondary System Loops

Figures 4.13 - 4.15 illustrate the components of the secondary loops. Each loop includes elements representing the tube-side of the IHX, the hot and cold leg piping, secondary pump, and DHX modules. Select parameters for the CVs, segments, and elements in the secondary heat transport system model are provided in Tables 4.15 - 4.17.

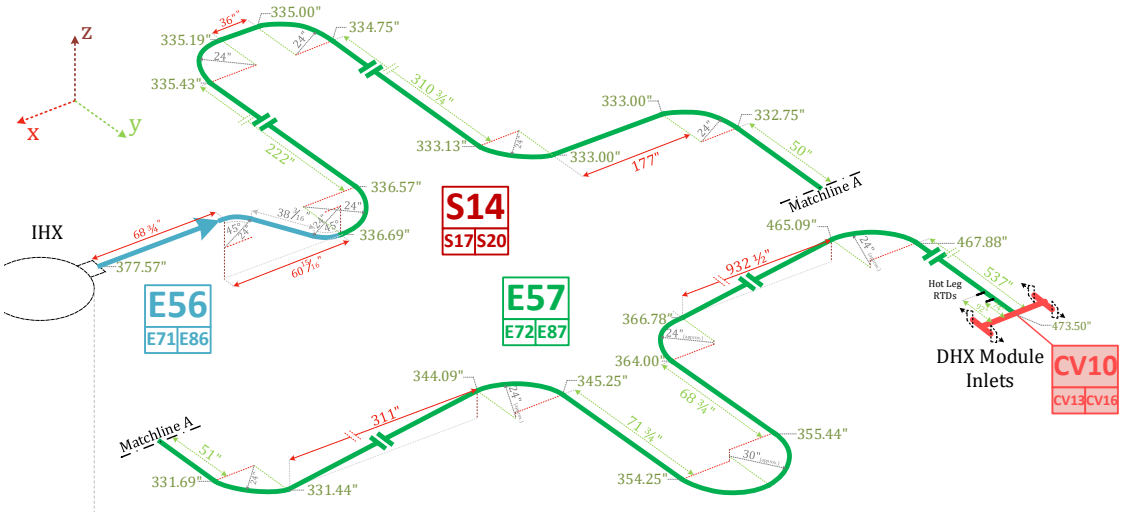

Figure 4.13. PRIMAR-4 Model: IHX Outlet to DHX Inlet Secondary Loop Piping

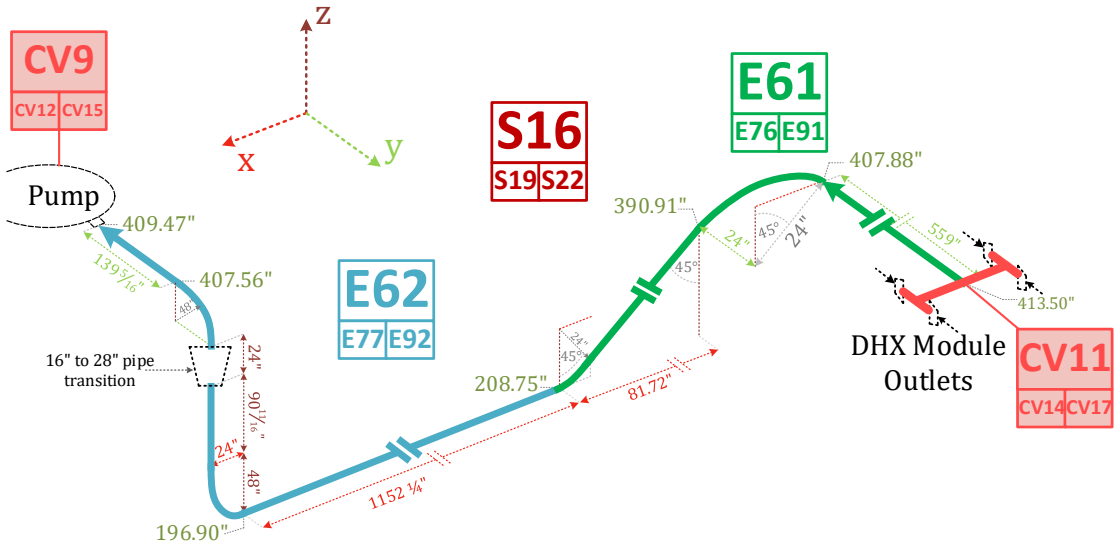

Figure 4.14. PRIMAR-4 Model: DHX Outlet to Pump Inlet Secondary Loop Piping

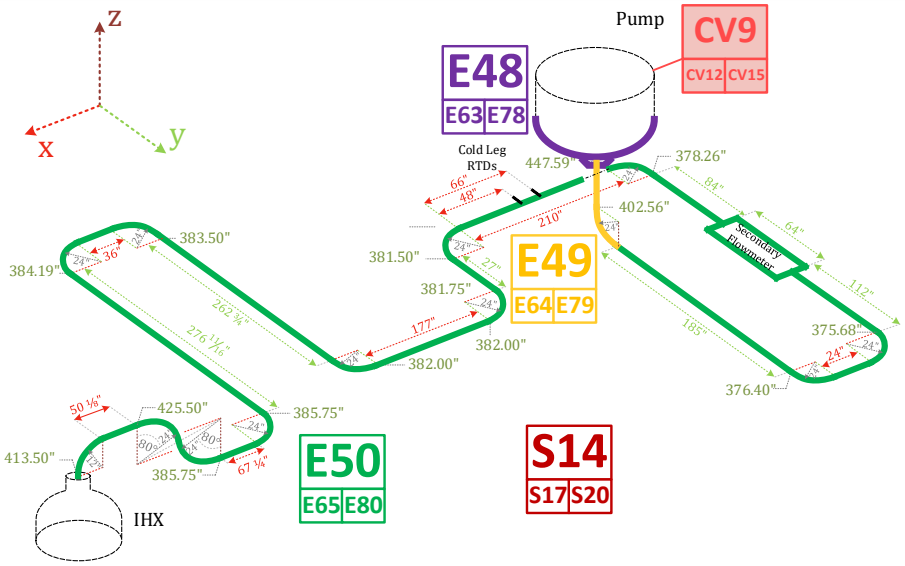

Figure 4.15. PRIMAR-4 Model: Pump Outlet to IHX Inlet Secondary Loop Piping

Table 4.15. Secondary System Compressible Volumes

CV#	Description	Sodium Volume (m^3)	Gas Volume (m^3)	Total Volume (m^3)
9, 12, 15	Secondary Loops #1-3 Pump Tanks	2.97	1.0	3.97
10, 13, 16	Secondary Loops #1-3 DHX Inlet	0.13	0.0	0.13
11, 14, 17	Secondary Loops #1-3 DHX Outlet	0.13	0.0	0.13

Table 4.16. Secondary System Segments

Segment #	Description	Mass Flow Rate (kg/s)		
		Test #10	Test #11	Test #12
14	Secondary Pump to DHX Inlet, Loop #1	729.9	729.9	735.5
15	DHX Modules #1-4, Loop #1	182.5	182.5	183.9
16	DHX Outlet to Secondary Pump, Loop #1	729.9	729.9	735.5
17	Secondary Pump to DHX Inlet, Loop #2	738.6	736.6	736.6
18	DHX Modules #1-4, Loop #2	184.6	184.1	184.1
19	DHX Outlet to Secondary Pump, Loop #2	738.6	736.6	736.6
20	Secondary Pump to DHX Inlet, Loop #3	735.8	730.9	732.0
21	DHX Modules #1-4, Loop #3	183.9	182.7	183.0
22	DHX Outlet to Secondary Pump, Loop #3	735.8	730.9	732.0

Table 4.17. Secondary System Elements

Element #	Description	Elevations (m)		Hydraulic Diameter (m)	Flow Area (m^2)	Length (m)
		Inlet	Outlet			
48, 63, 78	Pump	10.436	11.404	0.387	0.1178	0.968
49, 64, 79	Pump Outlet	11.404	9.596	0.387	0.1178	2.101
50, 65, 80	Cold Leg Pipe	9.596	10.538	0.387	0.1178	56.032
51, 66, 81	IHX Downcomer	10.538	1.033	0.387	0.1178	9.506
52, 67, 82	IHX Inlet Plenum	1.033	1.244	0.387	0.1178	0.831
53, 68, 83	IHX Non-Active Tubes	1.244	3.319	0.387	0.1178	2.075
54, 69, 84	IHX Tube-Side	3.319	7.675	0.020	0.4760	4.356
55, 70, 85	IHX Outlet Plenum	7.675	9.626	0.387	0.1178	0.831
56, 71, 86	IHX Outlet Pipe	9.626	8.588	0.387	0.1178	3.935
57, 72, 87	Hot Leg to DHX Inlet	8.588	12.062	0.387	0.1178	120.570
58, 73, 88	DHX Inlet Pipe	12.062	15.928	0.187	0.0274	22.167
59, 74, 89	DHX Modules #1-4	15.928	12.931	0.031	0.0512	46.549
60, 75, 90	DHX Outlet Pipe	12.931	10.538	0.187	0.0274	17.067
61, 76, 91	Cold Leg Pipe	10.538	5.338	0.387	0.1178	18.570
62, 77, 92	Cold Leg Pipe and Pump Inlet	5.338	10.436	0.387	0.1178	39.070

4.5.4 Dump Heat Exchangers

The DHX module in each loop contained four individual dump heat exchangers. Figure 4.16 illustrates the inlet and outlet piping for each DHX module in the PRIMAR-4 model. With one CV at each end of the modules, functioning as the inlet and outlet manifolds, the multiplicity feature was used to represent the four dump heat exchangers and their inlet and outlet piping within a DHX module using a single average segment.

Although the geometry of the dump heat exchangers was included in the model to account for their hydraulic losses, the DHXs themselves were modeled using a simple table look-up steam generator. The model uses a user-specified outlet temperature boundary condition. The temperature profiles during the transient for the four units in each DHX module were averaged together as shown in Figures 3.3 - 3.5 and input as one of the transient boundary conditions in the model.

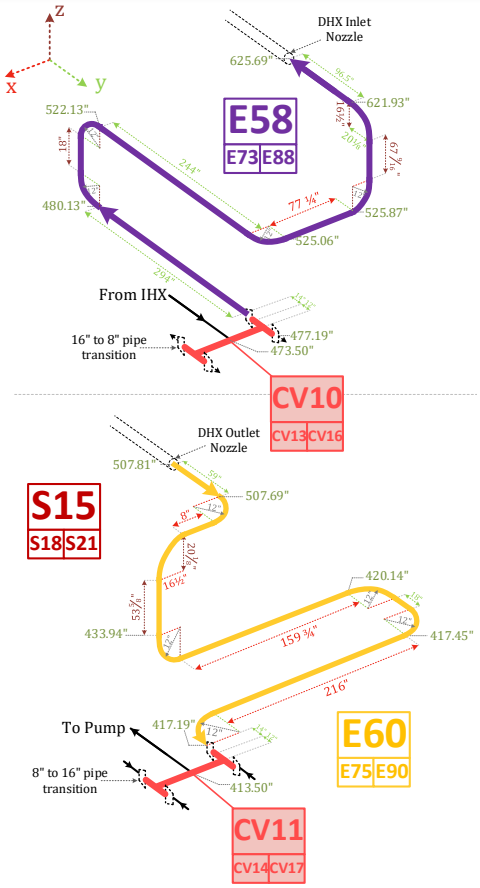

Figure 4.16. PRIMAR-4 Model: DHX Inlet and Outlet Pipes

4.5.5 Pumps

Elements 7, 19, and 31 represent the three primary sodium pumps and Elements 48, 63, and 78 represent the three secondary sodium pumps. The six pump elements in the PRIMAR-4 model were the first elements in their respective segments, each drawing from compressible volumes with cover gas representing the pump tanks.

Reference 1 specifies that the same homologous pump theory which is available in the SAS4A/SASSYS-1 homologous pump model provides a good approximation of the FFTF pumps, so this model was used for modeling the three primary loop pumps. Measured primary pump speed was provided as a boundary condition for the LOFWOS tests as shown in Figures 3.3 - 3.5, so the user-specified pump speed option was selected for the pump model. With this option, the motor torque and friction loss torque calculations are bypassed, and pump head is calculated directly based on pump speed and the current flow rate.

The secondary pumps did not trip during the LOFWOS tests, so using the homologous pump model is not necessary. Instead, the secondary pumps were modeled using the normalized pump head vs. time model, with a constant user-specified pump head defined for the entire transient simulation.

4.5.6 Component-to-Component Heat Transfer

In SAS4A/SASSYS-1 simulations, heat transfer is automatically simulated between a component's sodium and wall. The component-to-component heat transfer model in the code may be used to account for additional heat transfer paths, such as between two elements or from a CV to a constant temperature heat sink. This model can be used to simulate heat losses to the environment or heat transferred from a volume of sodium to a pipe that is flowing through that volume.

Reference 1 provides a list of additional heat losses and sources, which were incorporated into the SAS4A/SASSYS-1 model using the component-to-component heat transfer model. Table 4.18 lists these additional heat transfer paths and the heat transfer rates.

Pump heating is accounted for by specifying component-to-component heat transfer between the pump and a constant 99999°C heat source and a very low heat transfer coefficient. By specifying such a large temperature for the second component, the temperature difference between the two components will be nearly constant, leading to an essentially fixed heat transfer rate. Pump heating was only considered for the secondary pumps because the primary pumps tripped and therefore were not a significant source of heat after the start of the transient. The primary pump heat transfer paths were still included in the model in case they are needed for future simulations.

Ideally heat losses through the primary and secondary loop pipes would be distributed along all pipes in the model. However, due to a limited number of allowable component-to-component heat transfer paths in SAS4A/SASSYS-1, piping losses were assigned to the three longest elements in each primary loop and the two longest elements in each secondary loops. Because the LOFWOS tests are relatively short, this approximation is not expected to have a significant impact on the simulation results.

Table 4.18. Component-to-Component Heat Transfer

Description	Component 1	Component 2	Heat Transfer Rate (MW)
Bypass Vessel Cooling	CV4	CV3	1.62
Reactor Head and Vessel Losses	CV4	100°C	0.24
Primary Pump Heating	Elements 7, 19, 31	99999°C	0.0
Secondary Pump Heating	Elements 48, 63, 78	99999°C	0.67
Primary Loop Hot Leg Piping Losses	Elements 4, 16, 28	100°C	0.046
	Elements 5, 17, 29	100°C	0.045
Primary Loop Cold Leg Piping Losses	Elements 13, 25, 37	100°C	0.046
Secondary Loop Cold Leg Piping Losses	Elements 50, 65, 80	100°C	0.095
Secondary Loop Hot Leg Piping Losses	Elements 57, 72, 87	100°C	0.095

5 Results

In this section, predicted results for the LOFWOS and individual reactivity feedback tests are compared against the measured test data. The predicted results were generated with the model presented in Section 3.2 using SAS4A/SASSYS-1 Version 5.5.

5.1 LOFWOS Tests #10-12

LOFWOS Tests #10-12 were simulated two different ways. Results predicted using the point kinetics, reactivity feedback, and decay heat models are presented in this section. A version of the models using measured power as a boundary condition was created and used for troubleshooting during model development. Ultimately good agreement between measured and predicted power was reached and the results in these two types of simulations are very similar, so the measured power boundary condition version of the results is not shown here.

LOFWOS Tests #10-12 are driven by the three primary pumps tripping, causing flow through the core to decrease. Figure 5.1 illustrates the measured and predicted primary loop mass flow rates for the full flow range and the low flow range for LOFWOS Test #12. The measured and predicted primary loop mass flow rates agree very well throughout the test, though it can be seen that flow measurements become more uncertain at low flows. Since all three tests were initiated from full flow, the primary loop mass flow rate results are very similar for Tests #10-11 and are not shown here.

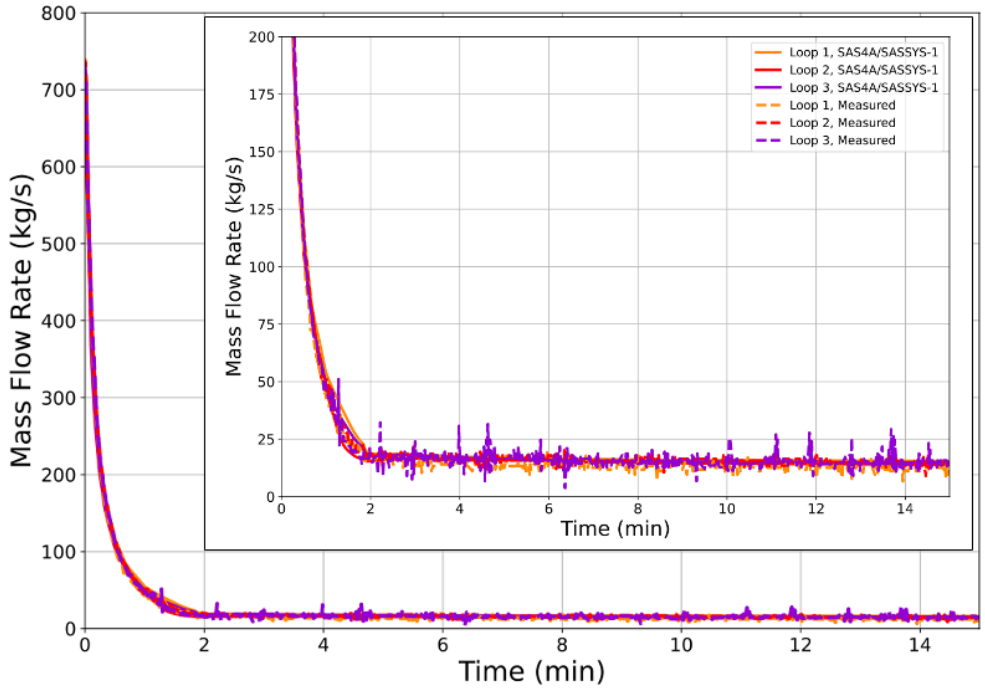

Figure 5.1. LOFWOS-12 Measured and Predicted Primary Loop Mass Flow Rates

When the primary pumps trip, large temperature changes in the core and a decreased core inlet pressure generated the necessary reactivity feedbacks to drive net reactivity negative, causing fission power to decrease and significantly reducing the core power level as the system worked to establish natural circulation. Figures 5.2 - 5.4 illustrate total power, fission power, and decay heat production for the full length of the tests as well as a closer view of the first three minutes of the tests.

Overall, power predictions agree well with the measured data throughout the tests. Decay heat is in excellent agreement for the whole test, while fission power is underpredicted slightly in the first minute of the tests and agrees well after that. Test #12 shows the best agreement in fission power in the first minute, with Tests #10 and #11 agreeing a little less closely.

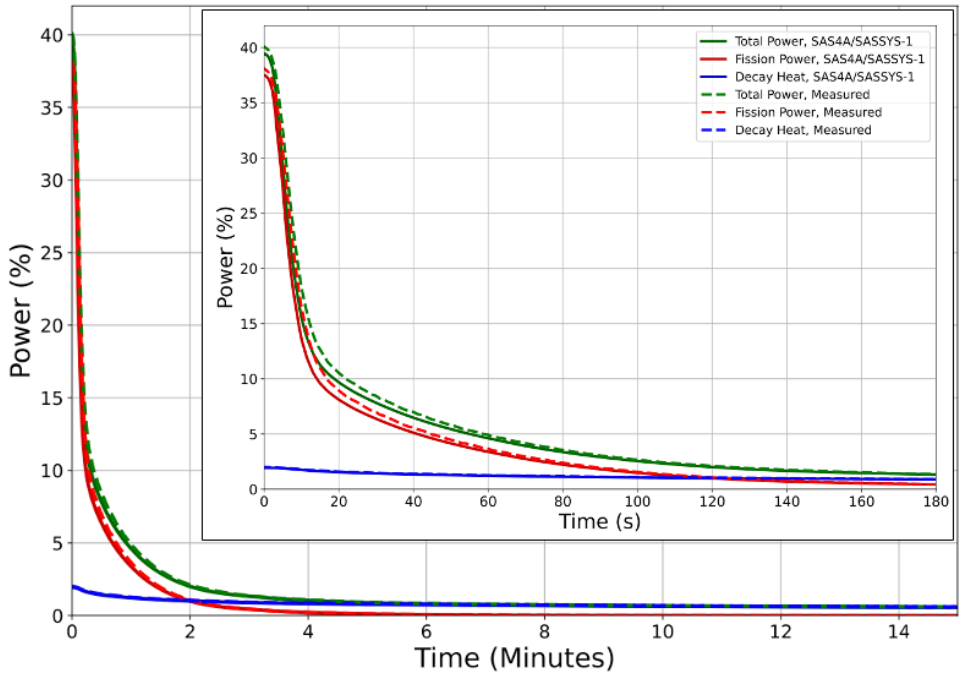

Figure 5.2. LOFWOS-10 Measured and Predicted Total Power, Fission Power, and Decay Heat

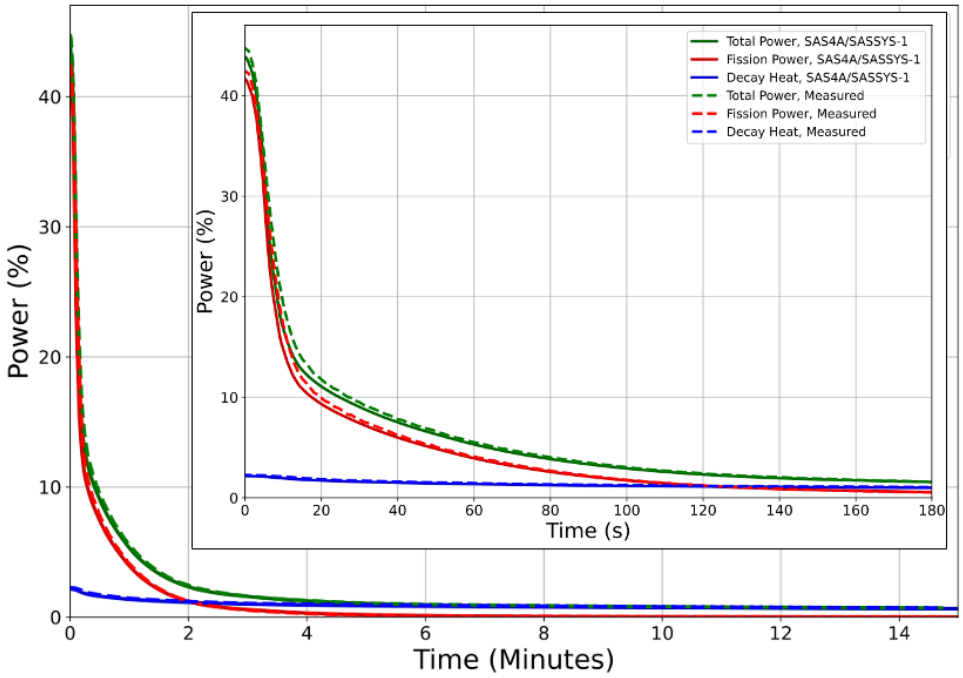

Figure 5.3. LOFWOS-11 Measured and Predicted Total Power, Fission Power, and Decay Heat

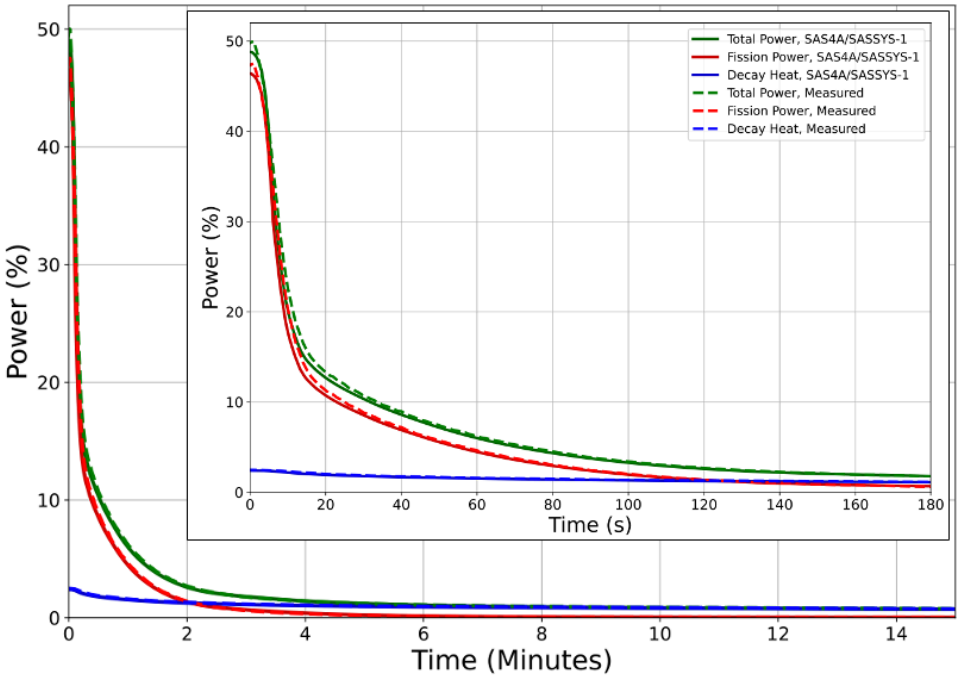

Figure 5.4. LOFWOS-12 Measured and Predicted Total Power, Fission Power, and Decay Heat

Figures 5.5 - 5.7 illustrate the reactivity feedbacks calculated by SAS4A/SASSYS-1 as well as the predicted net reactivity compared with the net reactivity calculated from the reactor power measurements (which for simplicity will be referred to as “measured” net reactivity). The model predicts the shape of the net reactivity very well.

During the first few seconds of the tests, fission power reduces primarily due to the negative reactivity from the GEMs. After twenty seconds, the core flow rate has decreased enough that the GEM gas-sodium interface level drops below the active fuel region. Most of the negative reactivity from the GEMs has been generated and the GEM reactivity feedback flattens out. The control rod driveline expansion feedback also generates negative reactivity during the tests, but that reactivity is introduced more slowly. Expansion of the control rod drivelines is driven by increasing core outlet temperatures. Sodium in the outlet plenum heats up, which causes driveline temperatures to increase as well. As the drivelines heat up, they expand and push the control rods further into the core. This feedback occurs more slowly than the other effects because of the large thermal inertia of the outlet plenum.

As core power decreases, fuel temperatures begin to decrease, which introduces a significant positive Doppler feedback response from the fuel. The other positive reactivity feedback is axial expansion of the fuel. For this transient, decreasing core temperatures result in axial fuel contraction, creating a more compact core with reduced radial neutron leakage. The coolant density, or voiding, reactivity feedback effect was negligible.

The final significant negative feedback is the radial core expansion reactivity feedback. Decreasing core flow rate leads to higher temperatures above the core. The load pads and restraint ring heat up and expand, exerting forces at key locations, resulting in the assembly being pushed radially outward within the fueled region. This resulting core radial expansion generates negative reactivity. After about 100 seconds, reduced temperatures cause the core to contract back towards its original pre-transient radial shape.

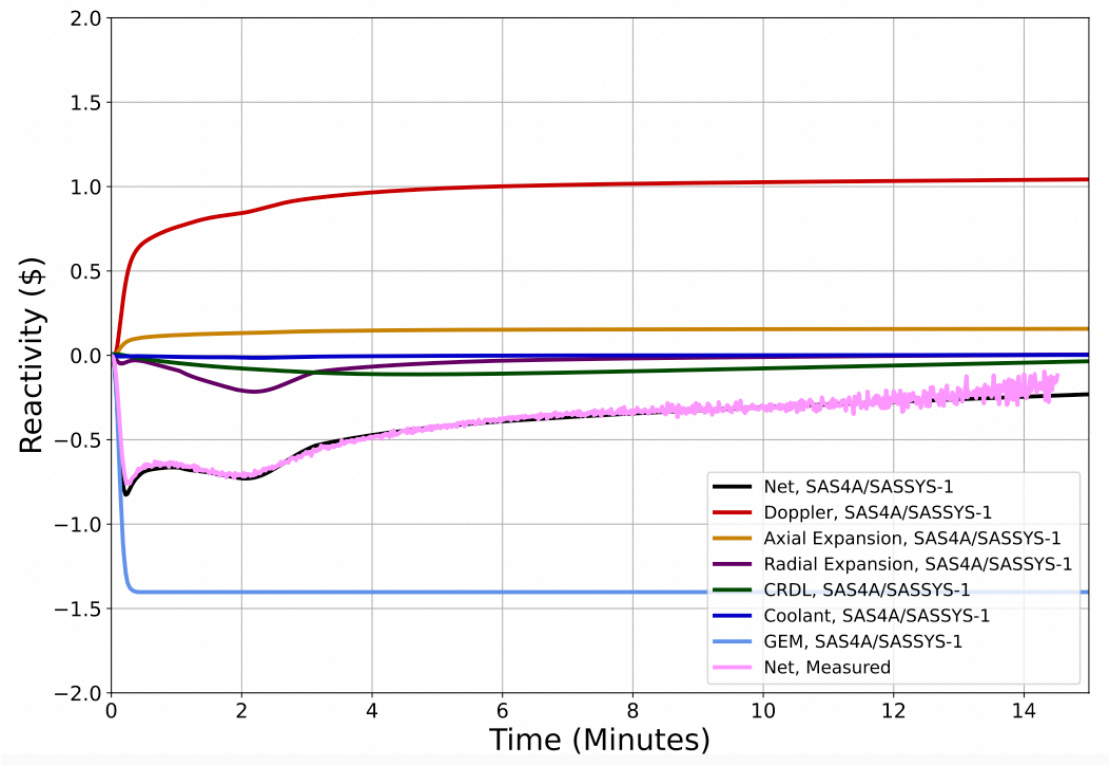

Figure 5.5. LOFWOS-10 Measured and Predicted Reactivity Feedback and Net Reactivity

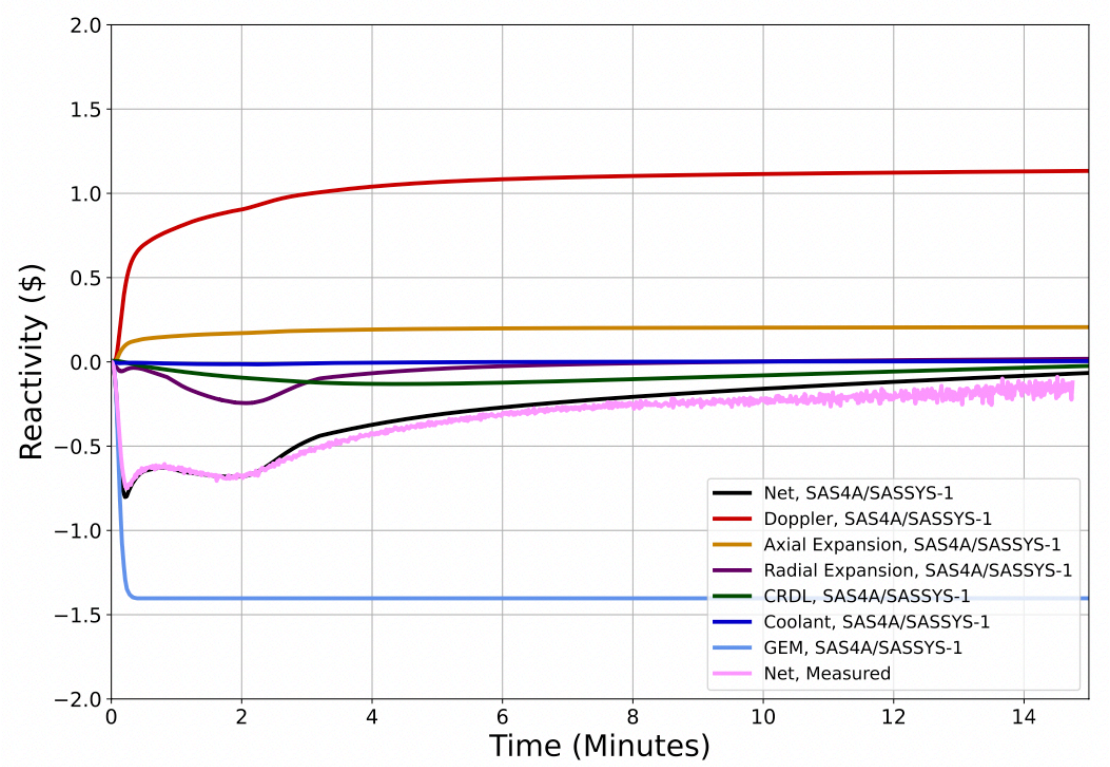

Figure 5.6. LOFWOS-11 Measured and Predicted Reactivity Feedback and Net Reactivity

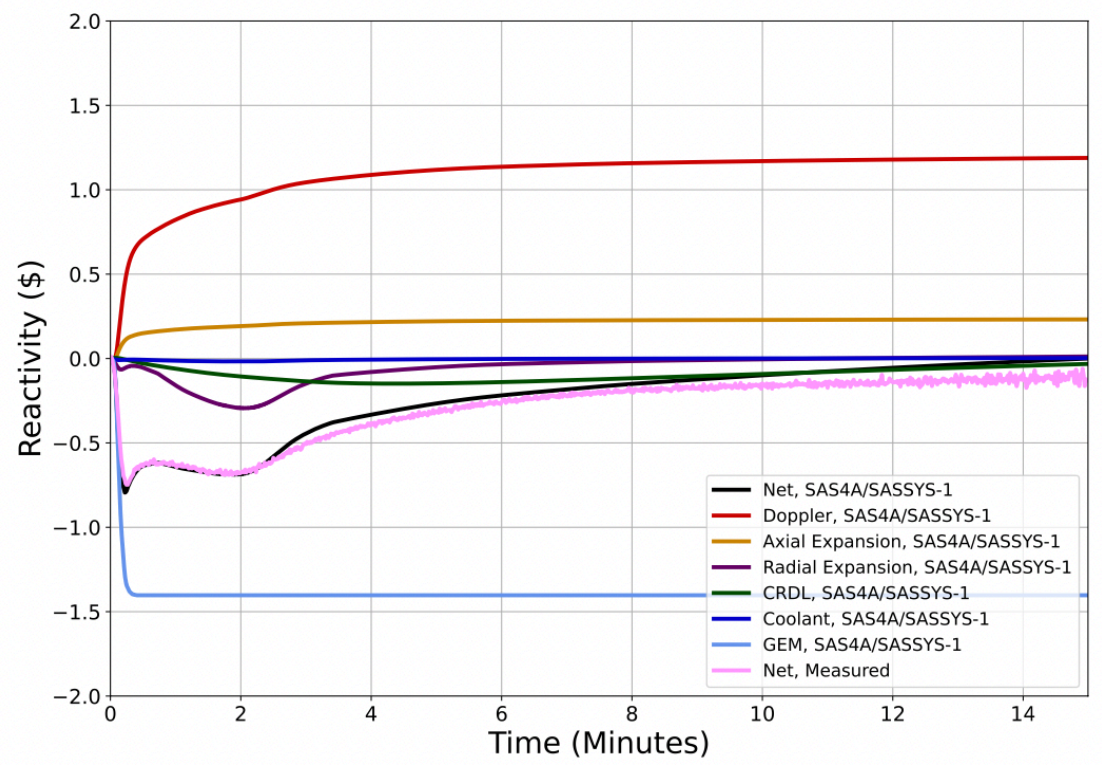

Figure 5.7. LOFWOS-12 Measured and Predicted Reactivity Feedback and Net Reactivity

Figures 5.8-5.10 illustrate the measured and predicted fast response PIOTA outlet temperatures. The Channel 8 PIOTA is near the center of the core in Row 2, and the Channel 9 PIOTA is at the periphery of the active core in Row 6. These temperatures are well-captured during the first twenty seconds as the core flow rate decreases. After the full GEM negative reactivity is inserted, the predicted PIOTA outlet temperatures for the Channel 9 PIOTA remain above the measured values for the remainder of the transient. This discrepancy could be due to underestimated heat transfer from this assembly to neighboring assemblies, since this assembly was located next to two colder assemblies (one reflector and one GEM). Additionally, there may be uncertainty in temperatures and trends for this assembly which is at the periphery of the active core. Because the Channel 8 assembly is the hottest in the core, the second peak in the Channel 8 PIOTA temperature curve represents the highest coolant temperature in the core during the LOFWOS transients. This temperature is matched by the SAS4A/SASSYS-1 results very well, particularly for Test #12, and is slightly underpredicted as the test initial power levels decrease in Tests #11 and #10.

A noticeable discrepancy between the measured and predicted fast response PIOTA outlet temperatures is the predicted “bump” in the temperatures which occurs a little after two minutes into the transient but does not appear in the measured data. This discrepancy is least pronounced for Test #12 and increases as the initial power levels of the tests decrease. The bumps were also observed in the predicted results for the simulation when measured power was used as a boundary condition, which eliminates the possibility of reactivity effects causing this behavior. Therefore, it is most likely that they are caused by variation of the flow rate entering the core from the primary pumps. Reference 1 does not provide any indications of the conditions of when primary pump

rotor locking occurred, but it is postulated that the bumps in temperature are caused by how the behavior of pump rotor locking is captured in the SAS4A/SASSYS-1 model.

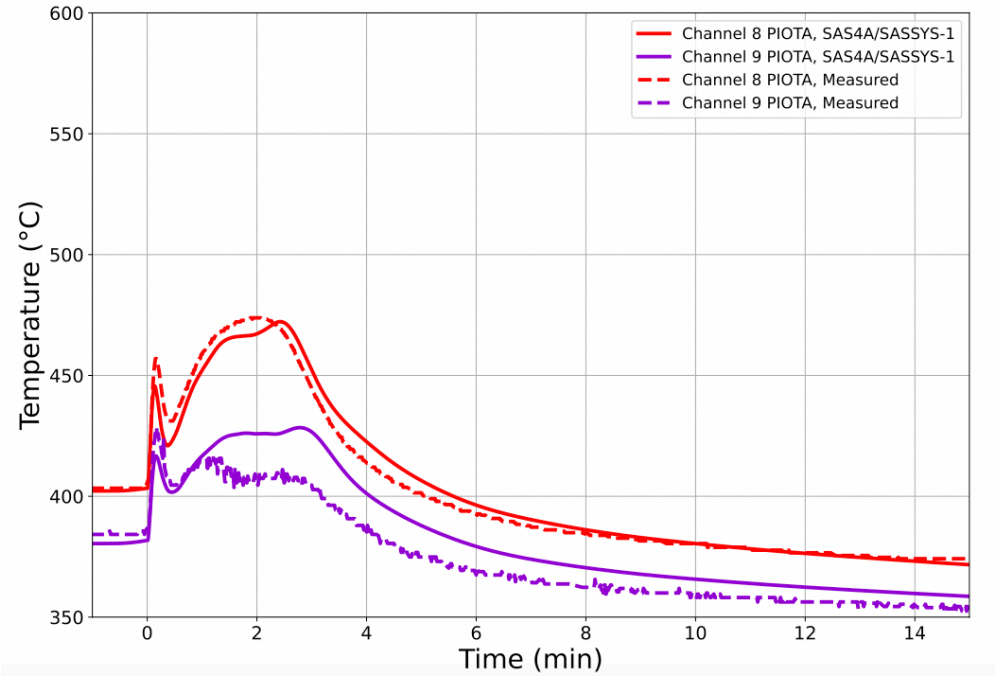

Figure 5.8. LOFWOS-10 Measured and Predicted PIOTA Outlet Temperatures

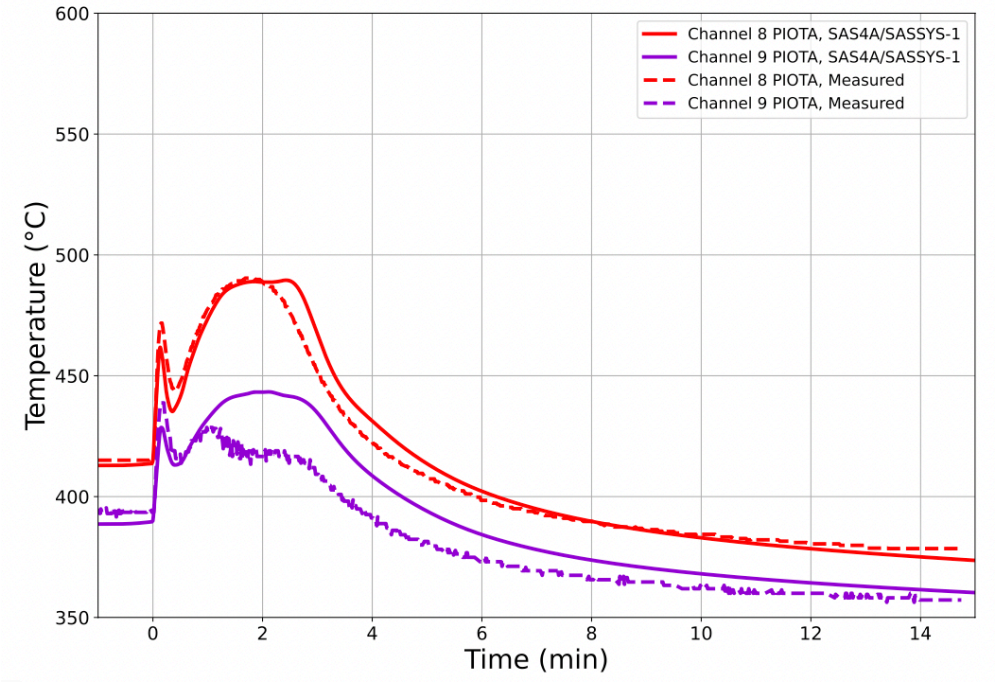

Figure 5.9. LOFWOS-11 Measured and Predicted PIOTA Outlet Temperatures

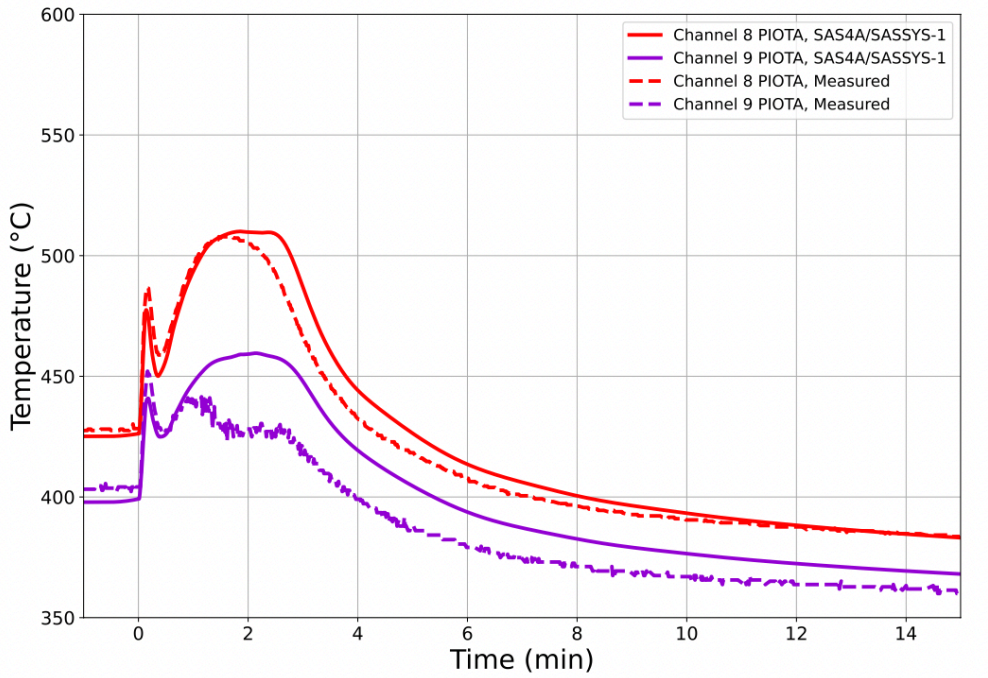

Figure 5.10. LOFWOS-12 Measured and Predicted PIOTA Outlet Temperatures

Figures 5.11 - 5.13 illustrate the measured and predicted hot and cold leg temperatures in the three primary and secondary loops. To directly compare these temperatures, a 5 second time constant was applied to the model predictions using the SAS4A/SASSYS-1 control system module. This time delay was included to account for instrumentation delay as described in Section 2.5.2.

The primary and secondary loop cold leg temperatures are relatively flat because they are measured far enough downstream of the core that they are not affected by core outlet temperature increases until well after the conclusion of the tests. The primary hot leg temperatures also change very little during the test. Because the secondary loop pumps do not trip but the primary pumps do, heat rejection through the IHXs is significantly reduced. The secondary hot leg temperatures decrease quickly after the primary pumps trip, reaching temperatures similar to the secondary cold leg since heat rejection through the IHXs is low.

Although the predicted and measured primary and secondary hot and cold leg temperatures demonstrate similar progressions, it appears that the predicted temperature changes occur approximately thirty seconds before the measured temperatures experience the same changes. This fairly consistent thirty-second discrepancy suggests an inconsistency between the test definition and measured test data as opposed to a modeling problem.

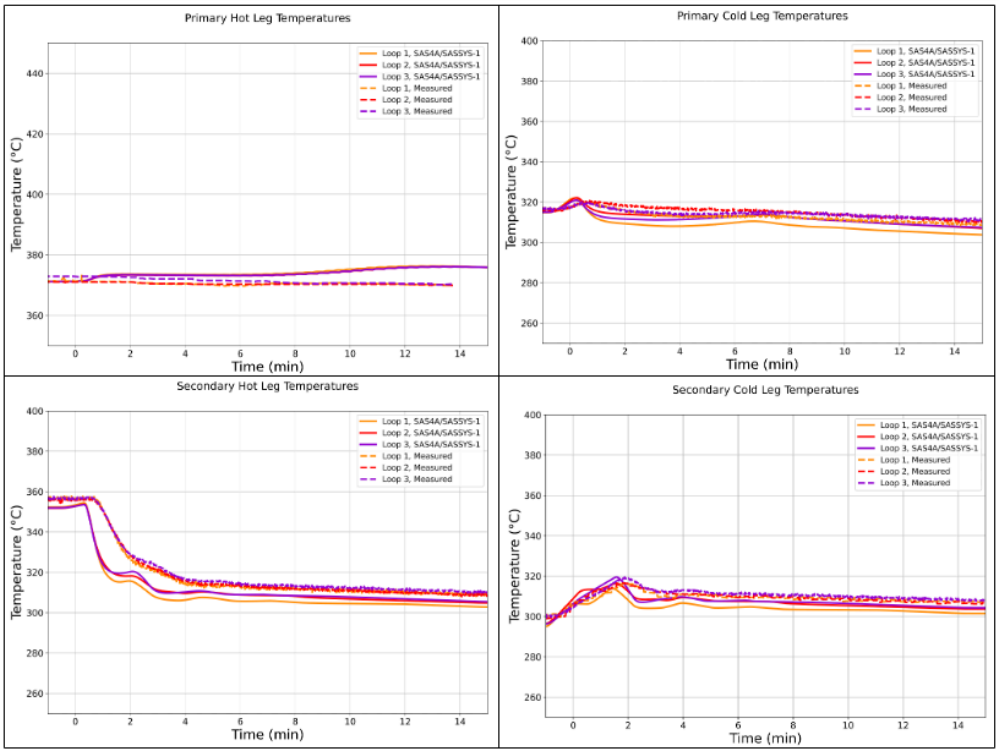

Figure 5.11. LOFWOS-10 Measured and Predicted Primary and Secondary Loop Temperatures

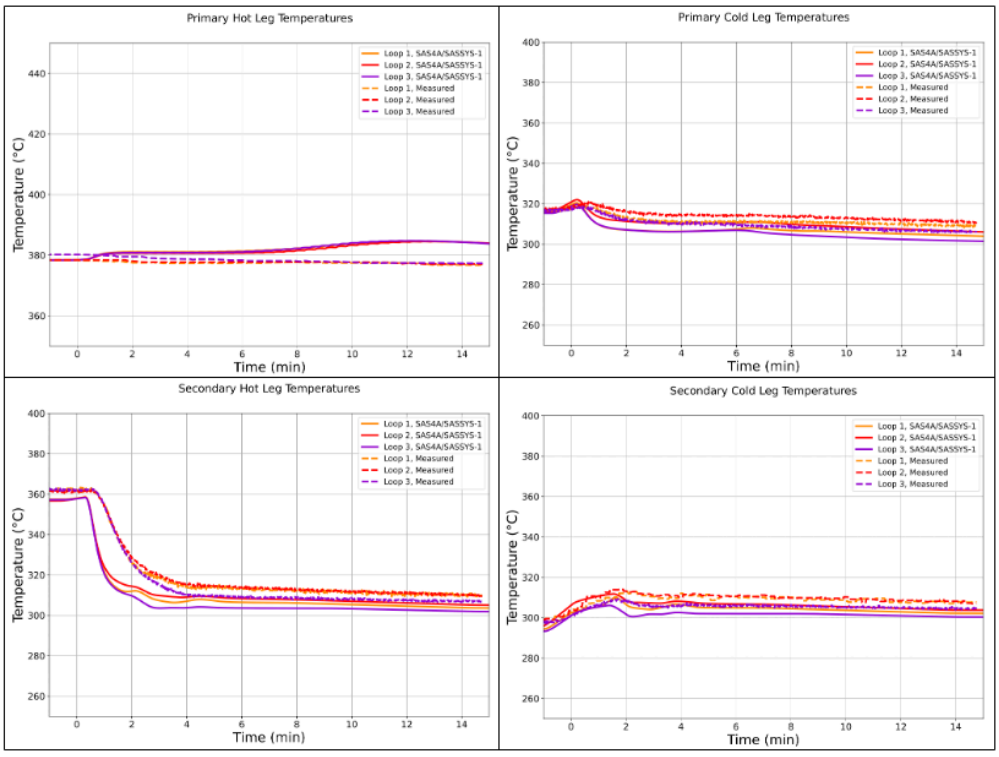

Figure 5.12. LOFWOS-11 Measured and Predicted Primary and Secondary Loop Temperatures

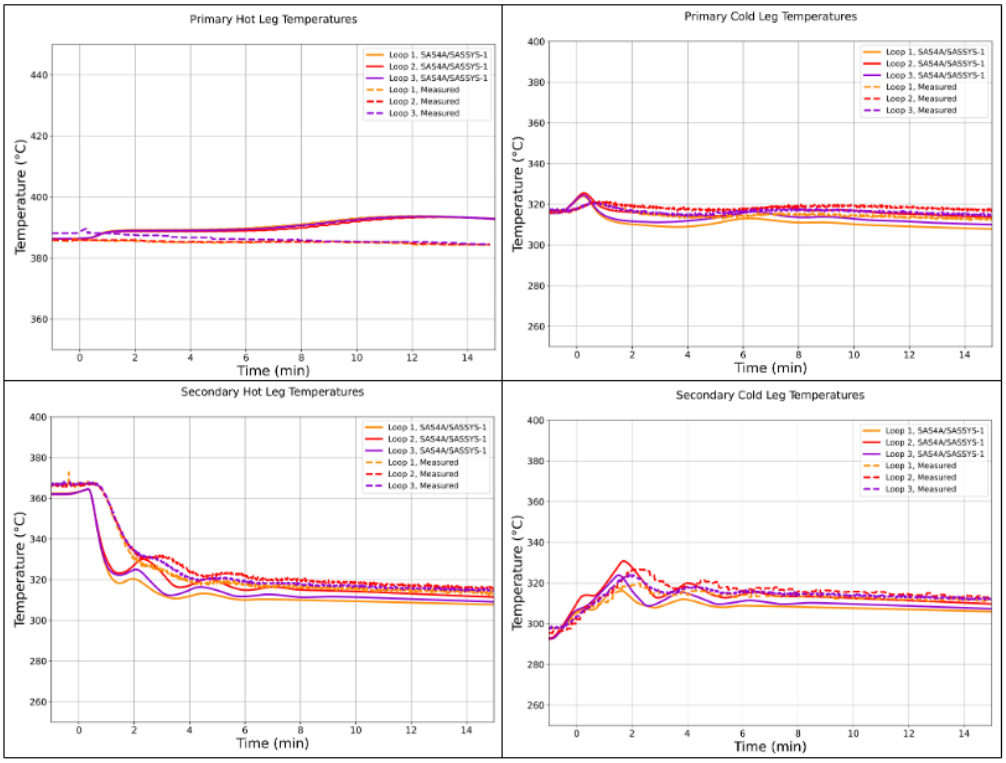

Figure 5.13. LOFWOS-12 Measured and Predicted Primary and Secondary Loop Temperatures

5.2 Individual Reactivity Feedback Tests

Net reactivity at the end of each step is the main output from the SAS4A/SASSYS-1 simulations for which there is corresponding measured data, so it is compared to FFTF measured reactivity data to evaluate how accurate the reactivity feedbacks are. To calculate the FFTF measured reactivity data, measurements of changes in control rod positions were converted to reactivity using rod worth information to determine the magnitude of the associated reactivity feedbacks between test states. Reactivity change from fuel burnup was also calculated and accounted for in the calculation.

Figures 5.14 – 5.20 show the validation results from the individual reactivity feedback tests. These figures each consist of three parts. The first plot compares the change in net reactivity from the reference step, which is the first step in each step series. The SAS4A/SASSYS-1 result is the sum of all reactivity feedbacks, while the FFTF value is calculated from the control rod positions minus the calculated reactivity from fuel burnup. The second plot shows the components of the reactivity feedback calculated by SAS4A/SASSYS-1. There is no similar data from the tests, but these plots confirm that the reactivity feedbacks in each series come from the sources they are expected to based on the type of test. The third plot shows the test conditions, which were input to SAS4A/SASSYS-1 as boundary conditions for power, core flow rate, and core inlet temperature. The power and flow rate boundary conditions are normalized to the Step 2B conditions for the purpose of input to SAS4A/SASSYS-1.

As discussed in Section 3.2.1, each set of SAS4A/SASSYS-1 calculations starts from the base Step 2B, then proceeds in simulating the specific set of steps. Although this approach is sufficient for thermal-hydraulic modeling of the core, there is an unavoidable simplification in this approach for the fuel performance and behavior. Specifically, none of the reactor history between the base and the first modeled step, or between the steps, is modeled. Therefore, the fuel conditions at the start of the test series may not be represented accurately. This uncertainty in fuel conditions would increase with the test number. Since fuel-cladding gap thickness and thermal conductivity are calculated by the DEFORM-4 fuel performance module and have significant effects on both fuel Doppler and axial expansion, these fuel reactivity feedbacks are most impacted by the uncertainty in fuel conditions.

Similarly, the reactivity feedback coefficients for the Cycle 8A model discussed in Section 4.4.1 were calculated based on the conditions of Step 2B and assumed to apply throughout the remainder of Cycle 8A. The uncertainty associated with this assumption would also increase with the test number. The inputs for CRDL feedback discussed in Section 4.4.2 were calculated based on the control rod positions at Step 2B and assumed to apply to the other steps as well. The Step 2B conditions were close to full power, and steps at different power levels could require a more accurate assessment using their actual control rod initial positions to develop the inputs for CRDL feedback.

SAS4A/SASSYS-1 simulations were performed with the detailed radial expansion model as discussed in Section 4.4.3, with the exception of tests with uniform core expansion (Type 3), which were simulated with the simple radial expansion model.

5.2.1 Type 1 Tests – Fuel Feedbacks

In the Type 1 tests, core inlet temperature was held approximately constant while power and flow were changed, roughly preserving the power-to-flow ratio. As a result, temperatures in the core remain constant except in the fuel. This type of test separates the fuel only reactivity feedbacks such as Doppler and axial expansion while minimizing reactivity feedbacks from coolant and structures.

Figure 5.14 shows the results from the four series of Type 1 tests that were simulated. The individual reactivity feedback results from SAS4A/SASSYS-1 confirm that the fuel feedbacks are dominant, and the rest of the feedbacks are negligible. Overall, very good agreement is achieved for the Type 1 tests.

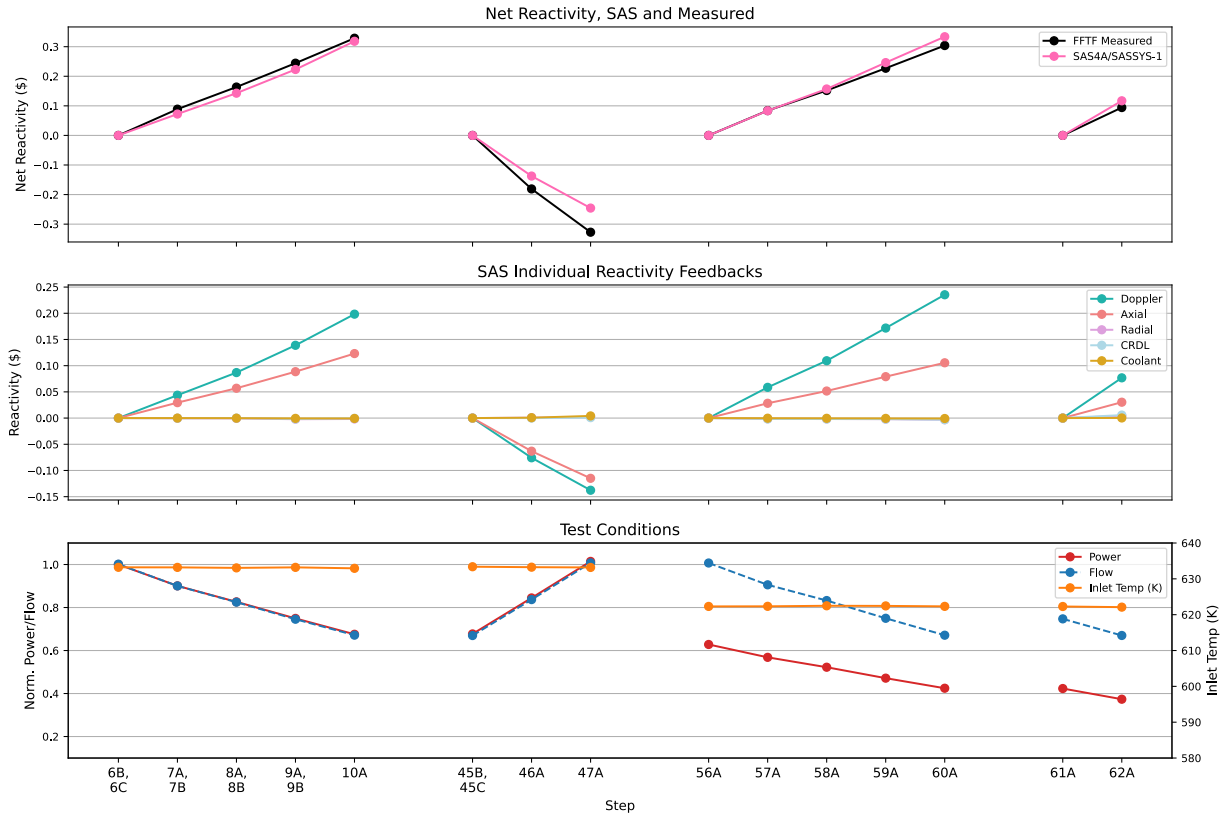

Figure 5.14. Type 1 (Fuel Feedback) Tests Measured and Predicted Reactivity

5.2.2 Type 2 Tests – Core Radial and CRDL Expansion

In the Type 2 tests, power was held constant, and the core inlet temperature and flow rate were adjusted to maintain a constant average coolant temperature. By maintaining average coolant, cladding, and fuel temperatures, reactivity feedbacks from coolant and fuel are minimized. Variation of the core inlet and outlet temperatures induces reactivity feedbacks from core structures, such as grid plate and load pads, as well as control rod driveline expansion.

Figure 5.15 shows the results from the seven series of Type 2 tests that were simulated. The individual reactivity feedback results from SAS4A/SASSYS-1 confirm that radial and CRDL expansion reactivity feedbacks are dominant, and the rest of the feedbacks are minimized. In the step 114B-115A-116A series, Doppler feedback contributes more than the other step series, which may be due to the average fuel temperature not being held as constant for this series as for the other series.

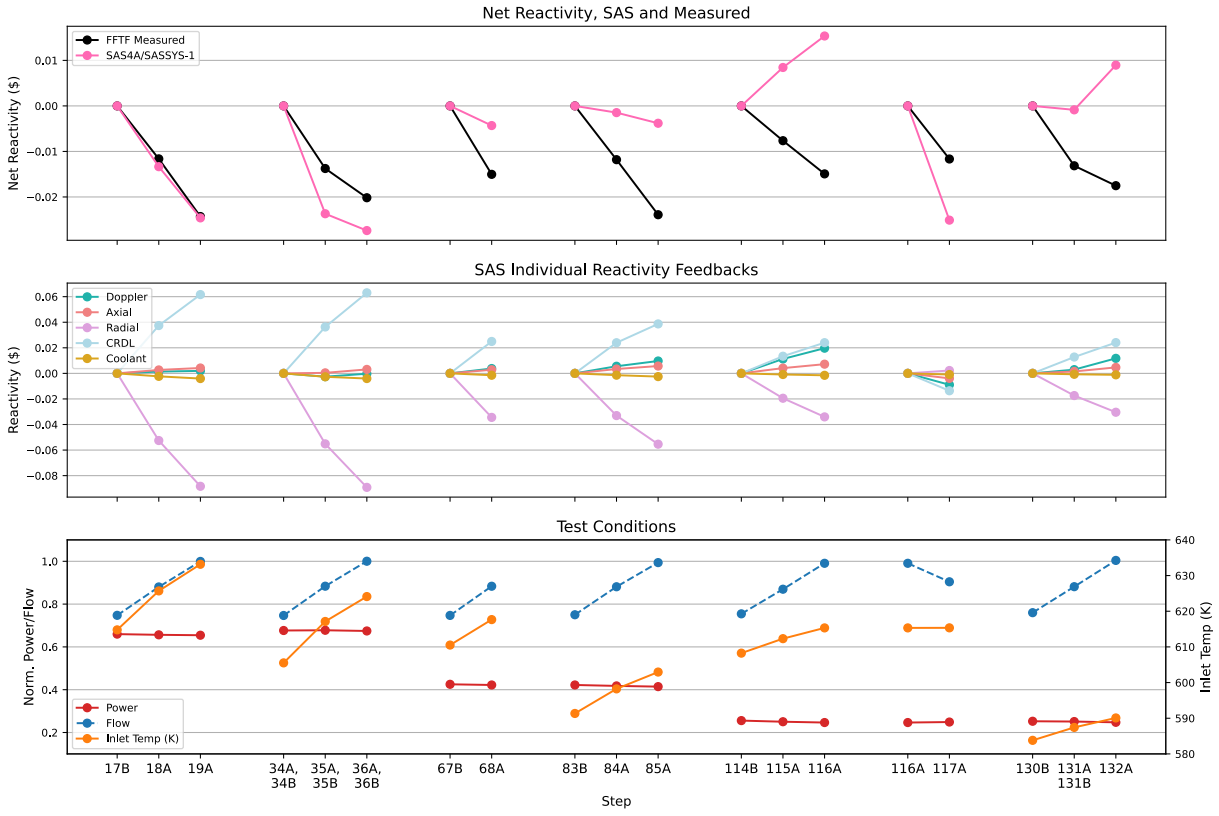

Figure 5.15. Type 2 (Core Radial / CRDL Expansion) Tests Measured and Predicted Reactivity

Although the general direction of net negative reactivity is preserved in most of the tests, there is still a significant difference from the measured data. The differences could be explained by a few observations. In these tests, the net reactivity is very small, less than 4 cents for all steps, since the two primary feedbacks are opposite in sign and of comparable magnitude. Therefore, even a small error in each feedback can result in a much larger relative difference for net reactivity. Accuracy of test data for such a small reactivity change has not been assessed yet. Additionally, since CRDL expansion reactivity feedback is a significant contributor to net reactivity, uncertainties in CRDL inputs particularly at powers less than nominal would have an impact on the Type 2 tests.

5.2.3 Type 3 Tests – Grid Plate Expansion

In the Type 3 tests, power was held constant, and the core inlet temperature and flow rate were adjusted to maintain a constant core outlet temperature. This minimized reactivity feedbacks from both load pad and CRDL expansion, making these tests useful for investigating the expansion of the core grid plate with nearly uniform core radial expansion.

Figure 5.16 shows the results from the five series of Type 3 tests that were simulated. The individual reactivity feedback results from SAS4A/SASSYS-1 confirm that radial expansion reactivity feedback is dominant. Overall, good agreement is achieved for the Type 3 tests, particularly the earlier steps, with results differing more for tests with higher step numbers.

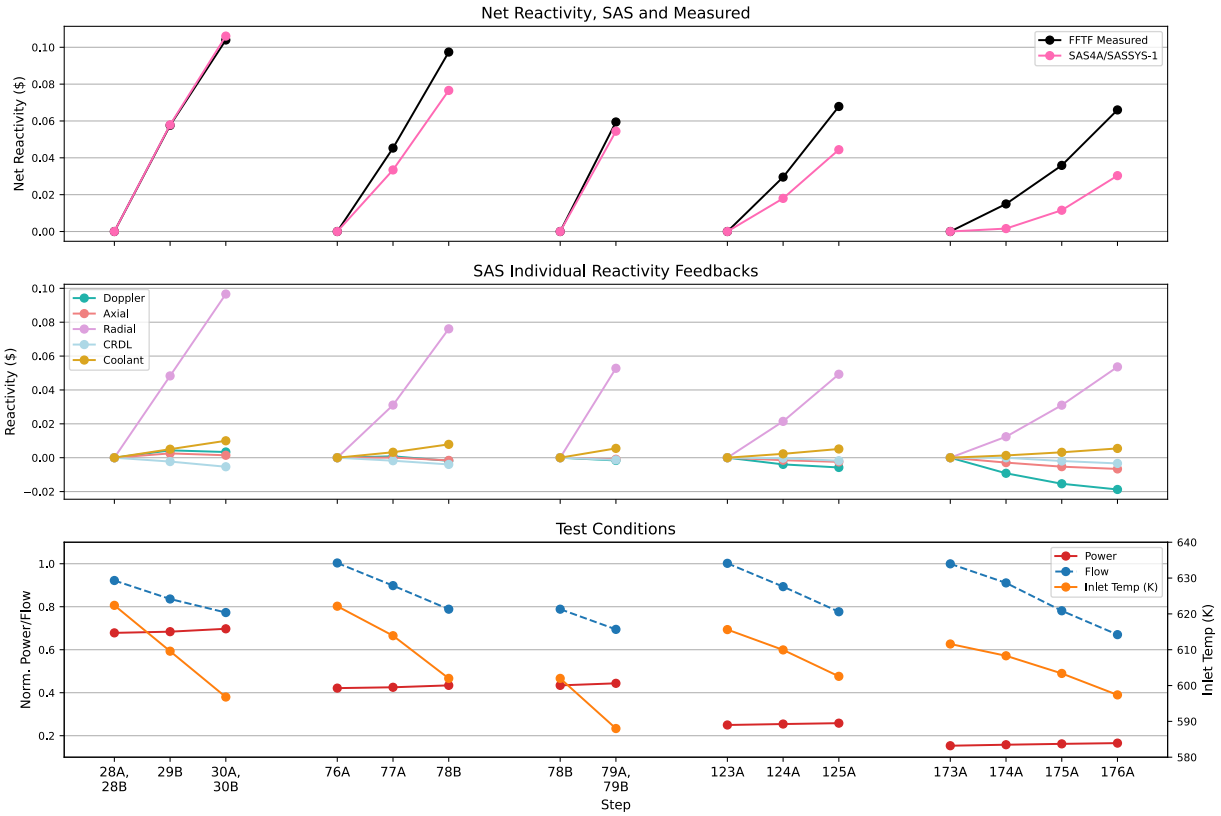

Figure 5.16. Type 3 (Grid Plate Expansion) Tests Measured and Predicted Reactivity

5.2.4 Type 4 Tests – Temperature Coefficient

In the Type 4 tests, power and core flow rate were held constant, and the core inlet temperature was adjusted to create a uniform temperature change. This integral test type evaluates temperature reactivity coefficients.

Figure 5.17 shows the results from the four series of Type 4 tests that were simulated. The individual reactivity feedback results from SAS4A/SASSYS-1 reflect that this is an integral test type and all of the reactivity feedbacks contribute, with the direction of the reactivity change dependent on the direction of the core inlet temperature change. Overall, good agreement is achieved for the Type 4 tests.

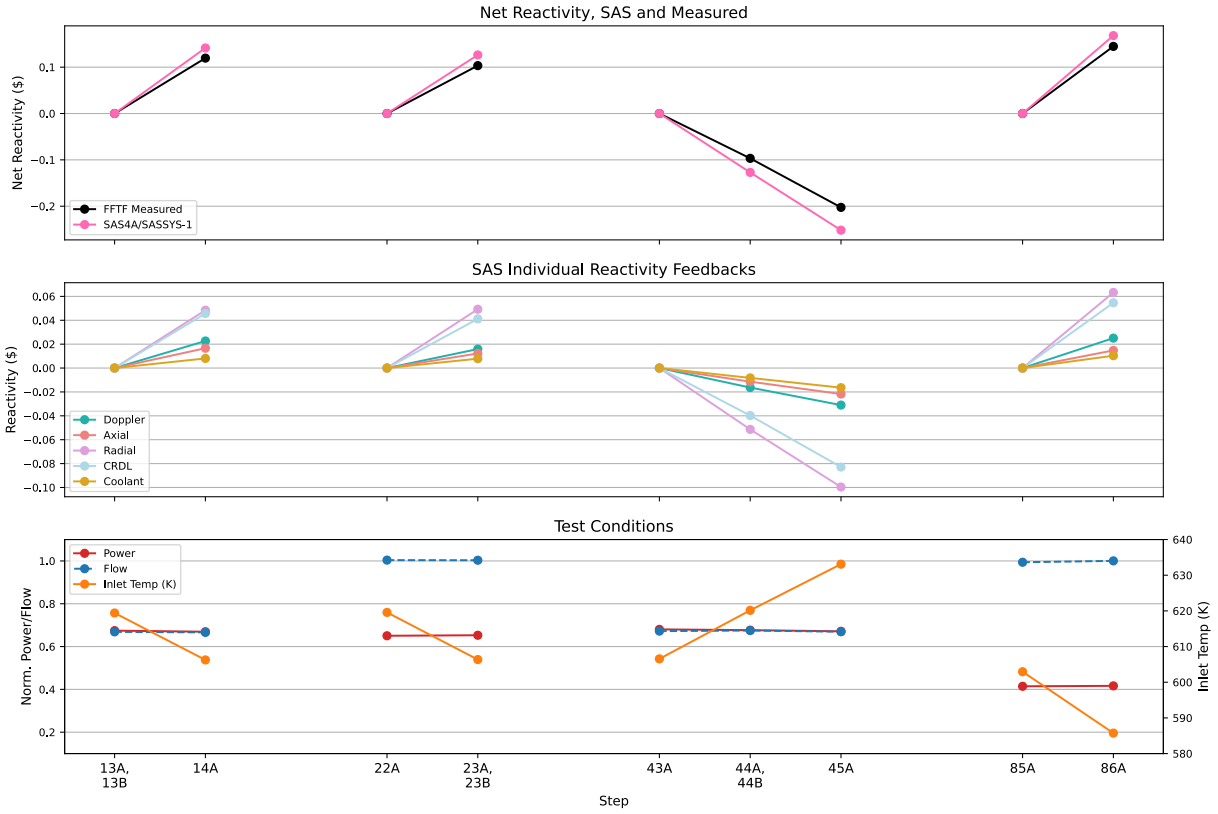

Figure 5.17. Type 4 (Temperature Coefficient) Tests Measured and Predicted Reactivity

5.2.5 Type 5 Tests – Flow Coefficient

In the Type 5 tests, power and core inlet temperature were held constant, and core flow rate was adjusted to create a uniform temperature change except at the core grid plate. This integral test type evaluates flow reactivity coefficients.

Figure 5.18 shows the results from the three series of Type 5 tests that were simulated. The individual reactivity feedback results from SAS4A/SASSYS-1 reflect that this is an integral test type and all of the reactivity feedbacks contribute.

Overall, good agreement is achieved for the Type 5 tests especially considering that they have some similarities to the Type 2 tests discussed in Section 5.2.2. Change in net reactivity is small, with CRDL and radial expansion feedbacks working against each other, though in this case the magnitude of the CRDL feedback is larger than radial expansion. Agreement is very good for the first test and differences increase as power level decreases and step number increases.

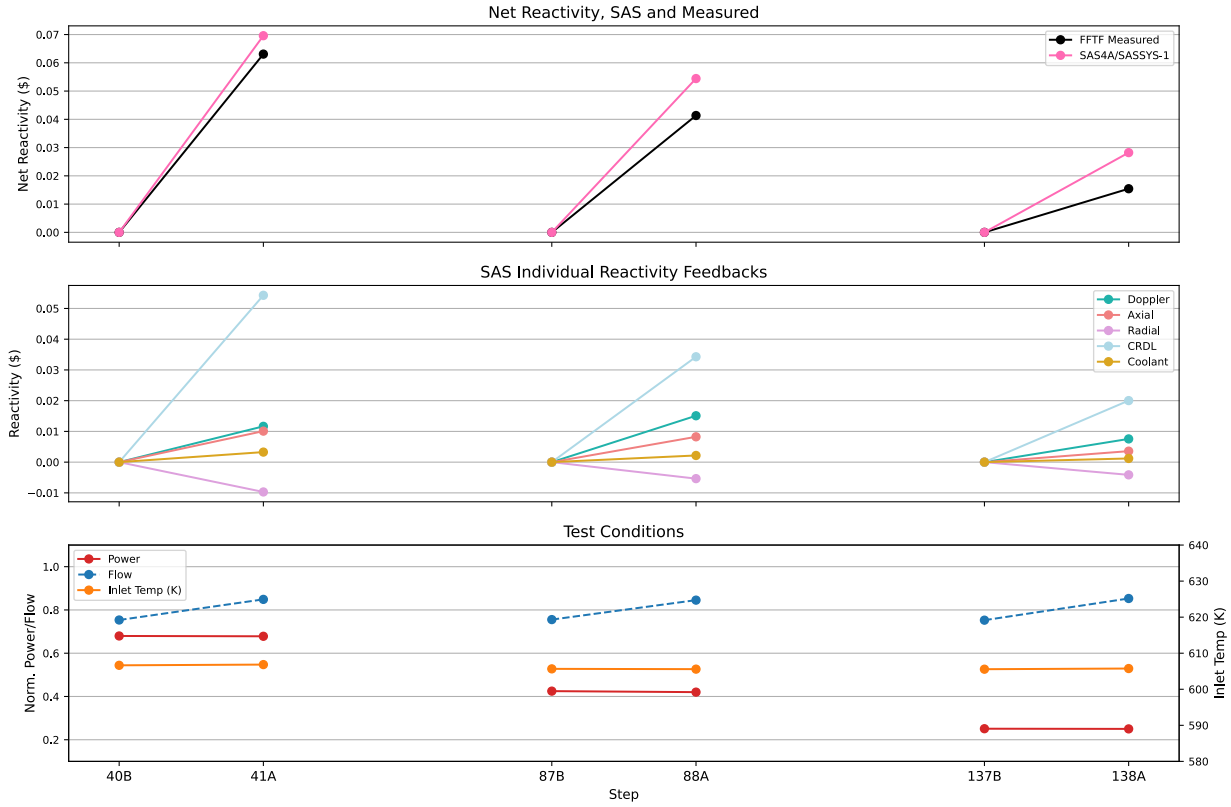

Figure 5.18. Type 5 (Flow Coefficient) Tests Measured and Predicted Reactivity

5.2.6 Type 6 Tests – Static Loss of Flow

In the Type 6 tests, core inlet temperature was held constant and core flow rate was adjusted. Power was allowed to adjust from the reactivity feedbacks only. This test type represents a static simulation of the Cycle 8C loss-of-flow tests.

Figure 5.19 shows the results from the three series of Type 6 tests that were simulated. The individual reactivity feedback results from SAS4A/SASSYS-1 reflect that this is an integral test type and all of the reactivity feedbacks contribute.

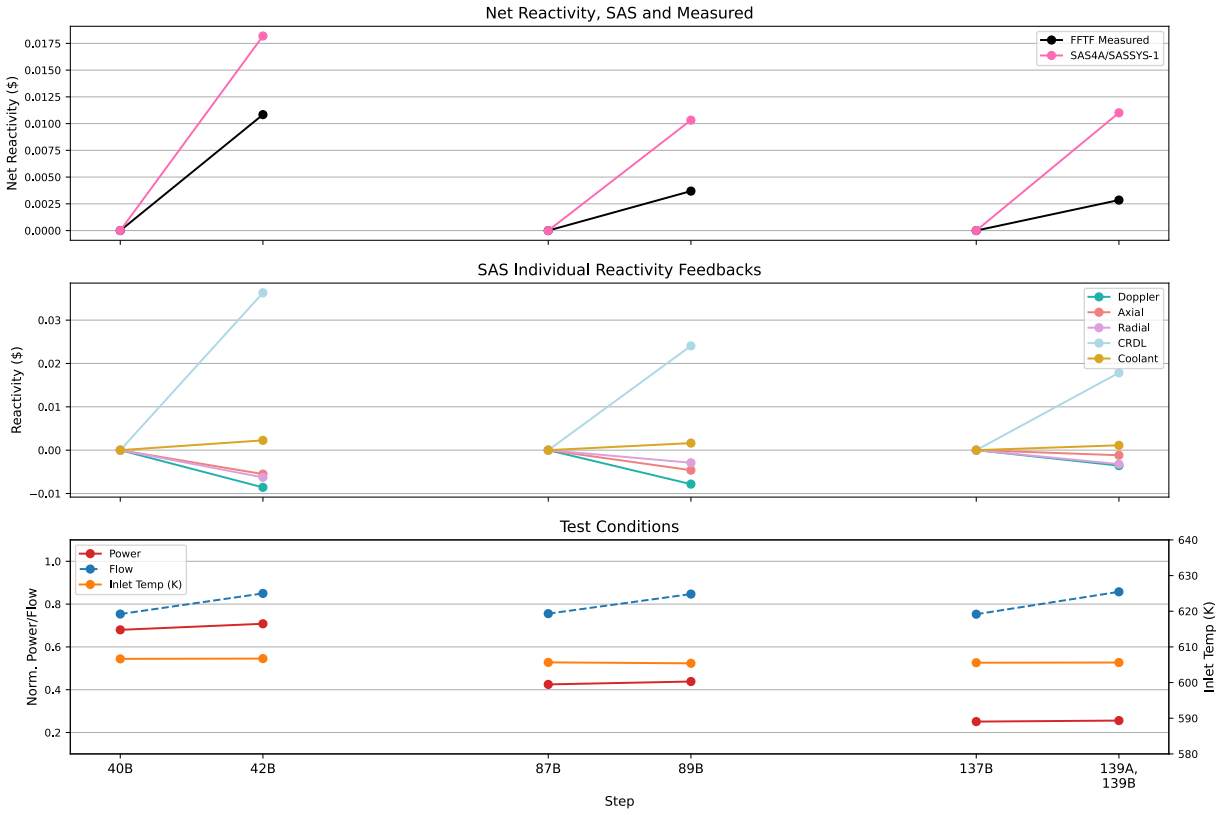

Figure 5.19. Type 6 (Static Loss of Flow) Tests Measured and Predicted Reactivity

Although the general direction of net positive reactivity is preserved in all of the tests, there is still a significant difference from the measured data. The differences could be explained by many of the same observations made for the Type 2 tests as discussed in Section 5.2.2. For the Type 6 tests, change in net reactivity is even smaller than the Type 2 tests, less than 2 cents in all cases. Additionally, CRDL expansion reactivity feedback is even more dominant in the Type 6 tests, so inaccuracy in that component affects the Type 6 tests significantly.

5.2.7 Type 7 Tests – Power Coefficient

In the Type 7 tests, core flow rate and core inlet temperature were held constant, and power was adjusted. This integral test type evaluates power reactivity coefficients and is similar to the Type 5 tests described in Section 5.2.5 except that the reactivity feedbacks are dominated by the fuel Doppler and axial expansion feedbacks.

Figure 5.20 shows the results from the four series of Type 7 tests that were simulated. The individual reactivity feedback results from SAS4A/SASSYS-1 reflect that this is an integral test type, with mainly the fuel Doppler and axial expansion feedbacks, and CRDL expansion feedback contributing.

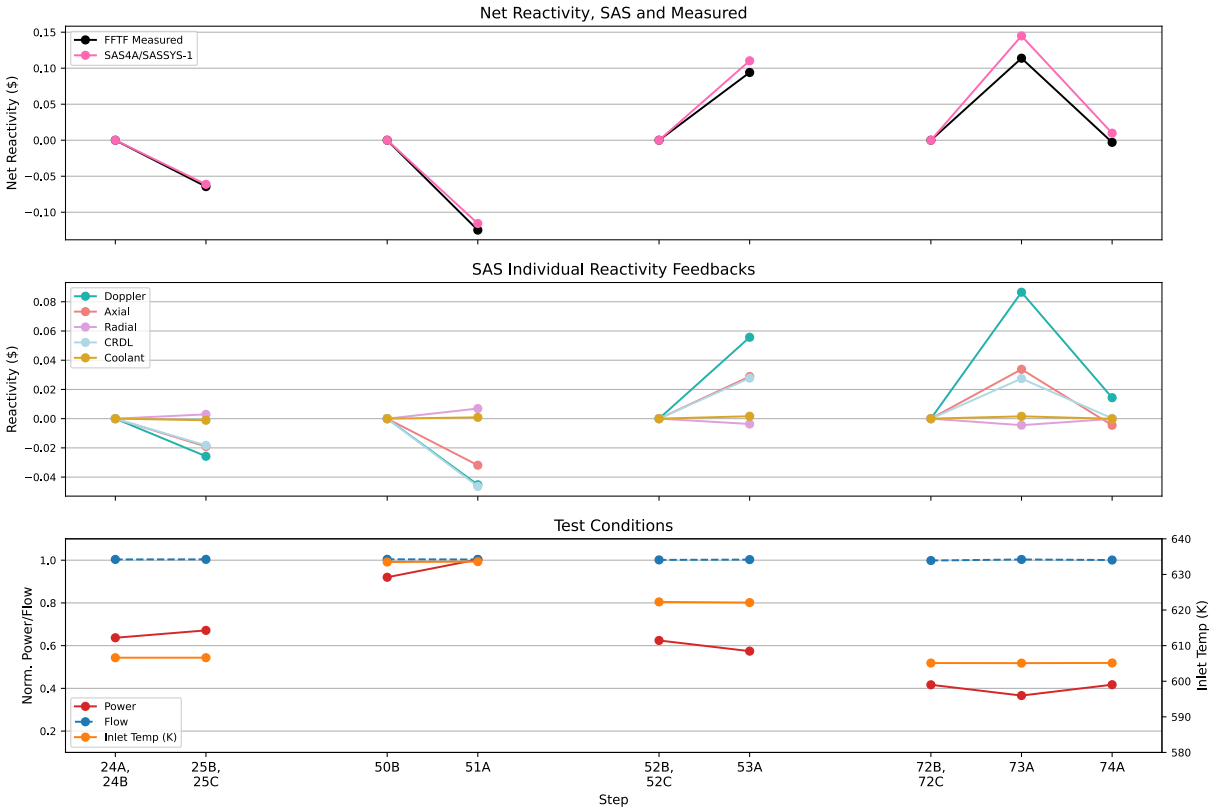

Figure 5.20. Type 7 (Power Coefficient) Tests Measured and Predicted Reactivity

Overall, very good agreement is achieved for the Type 7 tests. Of particular interest is the last test, step series 72B, 72C – 73A – 74A. The third step of this test returns very close to the same conditions of the initial step, and the FFTF measured change in reactivity reflects this as it returns to about zero. However, the SAS4A/SASSYS-1 net reactivity does not return quite to zero, driven primarily by the Doppler reactivity feedback. It is possible this is due to not being able to accurately capture the timing of the test steps, and because the SAS4A/SASSYS-1 DEFORM-4 fuel performance models are more applicable to long-term irradiation than quick transients. These models impact the fuel-clad gap conductance, which affects fuel temperature and therefore the magnitude of the Doppler reactivity feedback. This is more noticeable in the step series 72B, 72C – 73A – 74A because it is the only symmetrical test simulated in that the final step returns to the same initial conditions of the first step. Despite the non-symmetrical result from SAS4A/SASSYS-1 in the last series, excellent agreement with measured data is achieved for the Type 7 tests in general.

6 Summary and Conclusions

The FFTF Passive Safety Testing program provided data for computer code validation, confirmed the safety margins of FFTF as a liquid metal reactor, and demonstrated the inherent and passive safety benefits of its specific design features. The program included thirteen loss of flow without scram tests initiated at varying power levels, some of which did not use primary loop pony motors and therefore the primary system was allowed to transition to natural circulation flow rates. In preparation for the Passive Safety Testing program, a series of individual reactivity feedback tests were performed which were designed to simulate and validate specific features and reactivity feedbacks of the FFTF core.

Three of the natural circulation LOFWOS tests were simulated with Argonne's SAS4A/SASSYS-1 fast reactor safety analysis code to support the validation base of the code. The FFTF SAS4A/SASSYS-1 model used for the LOFWOS tests represents the core and the primary and secondary heat transport systems. The core model was developed to represent Cycle 8C, the cycle during which the LOFWOS tests were performed. All assemblies in the core with the exception of the GEM assemblies are represented by twenty-nine channels using channel models for the driver fuel, reflector assemblies, and control assemblies. Reactivity feedback from the GEM assemblies was incorporated using the SAS4A/SASSYS-1 control system module. Point kinetics, reactivity feedback, and decay heat models were developed for predicting core power. The primary heat transport system model included models to represent the reactor vessel, piping for the three primary loops and pumps, and the intermediate heat exchanger. The secondary heat transport system model included models for the piping for the three secondary loops and pumps, and the dump heat exchangers. Temperature boundary conditions were specified at the dump heat exchanger outlets.

Primary loop flow rates are well-predicted throughout the tests. Power predictions agree well with the measured data throughout the tests, though fission power is slightly underpredicted in the first minute of the tests but agrees very well after that. The model predicts the net reactivity shape very well. The fast response PIOTA outlet temperature that represents the peak core coolant temperature is matched by the SAS4A/SASSYS-1 results very well particularly for Test #12 and is slightly underpredicted as the test power levels decrease in Tests #11 and #10. The fast response PIOTA outlet temperature in the assembly located at the periphery of the active core is overpredicted for most of the transient, which could be due to underestimated heat transfer from this assembly to neighboring assemblies. The predicted and measured primary and secondary hot and cold leg temperatures demonstrate similar progressions, though the predicted temperature changes occur approximately thirty seconds before the measured temperatures experience the same changes. It is thought that this is due to an inconsistency between the test definition and measured test data as opposed to a modeling problem.

A selection of individual reactivity feedback tests were also simulated with SAS4A/SASSYS-1 to support the validation base of the code. The FFTF SAS4A/SASSYS-1 model used for the individual reactivity feedback tests represents the core only, since the analysis is focused on the core reactivity feedbacks. Core inlet temperature and flow rate were specified as boundary conditions using measured data. The core model was developed to represent Cycle 8A, the cycle during which the individual reactivity feedback tests were performed. All assemblies in the core are represented by nineteen channels using channel models for the driver fuel, fueled tests assemblies, reflector assemblies, and control assemblies. Point kinetics and reactivity feedback models were developed for predicting net reactivity.

Net reactivity is very well predicted for many of the individual reactivity feedback tests. Agreement with measured data for the fuel feedback, temperature coefficient, and power coefficient test types was excellent. The grid plate expansion and flow coefficient test types were well predicted, but with slightly larger differences between measured and predicted data. The core radial and CRDL expansion and static loss of flow test types did not agree with the measured data as well as the other test types.

One source of differences between predicted and measured net reactivity seems to be due to the SAS4A/SASSYS-1 prediction of CRDL expansion reactivity feedback. This may be because the inputs for CRDL feedback were developed based on the same starting control rod position. Steps at different starting power levels could require a more accurate assessment using their actual control rod initial positions. Another source of differences could be because the SAS4A/SASSYS-1 fuel performance models are more applicable to long-term irradiation than quick transients, and due to simplifications made in fuel performance modeling. Specifically, none of the reactor history between the base and the first modeled step, or between the steps, is modeled. Fuel performance modeling impacts fuel-cladding gap thickness and thermal conductivity which have significant effects on fuel reactivity feedbacks.

Overall, it can be concluded that for LOFWOS Tests #10-12, there was good agreement between the flow, power, and temperature predictions and the measured data. For the individual reactivity feedback tests, there was good agreement between net reactivity predictions and the measured data.

Acknowledgement

This work was sponsored by the U.S. Department of Energy's Office of Nuclear Energy (NE) and Office of Clean Energy Demonstrations (OCED) as part of the Advanced Reactor Demonstration Program (ARDP).

References

1. T. Sumner, A. Moisseytsev, F. Heidet, D.W. Wootan, A.M. Casella, and J.V. Nelson, "Benchmark Specification for FFTF LOFWOS Test #13," ANL-ART-102 (Rev 2), Argonne National Laboratory report, July 31, 2022.
2. PNNL/HEDL, unpublished information, 2020.
3. A. J. Brunett, L. Ibarra, T.H. Fanning, and R. Hu, "Improvements and Path Forward for Regulatory Acceptance of SAS4A/SASSYS-1", ANL/NSE-18/13, Nuclear Science and Engineering Division, Argonne National Laboratory, October 31, 2018.
4. A. Moisseytsev, D. Wootan, and T. Sumner, "Simulation of FFTF Individual Reactivity Feedback Tests with SAS4A/SASSYS-1 Code", 2022 International Conference on Fast Reactors and Related Fuel Cycles, Vienna, Austria, April 19-22, 2022.
5. American Nuclear Society, Decay Heat Power in Light Water Reactors, ANSI/ANS-5.1-2005.
6. T.H. Fanning, A. J. Brunett, and T. Sumner, eds., The SAS4A/SASSYS-1 Version 5.5 Safety Analysis Code System", ANL/NSE-SAS/5.5, Nuclear Science and Engineering Division, Argonne National Laboratory, 2022.
7. Croff, G. "A User's Manual for the ORIGEN2 Computer Code," ORNL/TM-7175 (July 1980).

Appendix A. Cycle 8A Boundary Conditions

Step	Power (%)	Primary Flow (%)	Core Inlet Temperature (°F)	Reactivity Change (cents) from Step 2B		
				Change due to Rod Movement	Change due to Burnup	Total Change
2B	94.98	99.97	679.85	0.000	0.000	0.000
3A	87.26	100.07	679.59	-12.108	0.256	-11.852
3B	87.16	100.13	679.51	-12.108	0.412	-11.696
4A	87.29	94.02	679.83	-7.664	0.692	-6.972
4B	87.43	94.18	679.84	-7.664	0.778	-6.886
5A, 5B	86.70	99.54	660.56	-21.114	1.242	-19.872
6A	95.44	100.25	679.75	2.430	2.309	4.739
6B, 6C	95.00	100.13	680.13	2.342	2.814	5.156
7A, 7B	85.55	90.02	680.09	-6.008	3.343	-2.665
8A, 8B	78.49	82.46	679.84	-13.159	3.671	-9.488
9A, 9B	71.17	74.53	680.10	-20.990	3.907	-17.083
10A	64.16	67.12	679.62	-29.215	4.125	-25.090
10B	63.93	66.73	679.35	-29.995	4.747	-25.248
11A, 11B	62.94	75.48	679.82	-38.854	5.042	-33.812
12A	59.25	66.31	679.39	-39.973	5.294	-34.679
12B	59.26	66.32	679.41	-39.973	5.344	-34.629
13A, 13B	64.06	66.85	655.27	-40.814	5.689	-35.125
14A	63.57	66.60	631.59	-52.431	6.025	-46.406
14B	63.32	66.59	631.43	-52.847	6.244	-46.603
14C	62.76	66.57	631.74	-52.847	7.236	-45.611
15A, 15B	61.99	75.67	631.21	-61.615	7.522	-54.093
16A, 16B	58.98	66.69	631.89	-61.046	7.782	-53.264
17A	62.57	74.55	646.91	-51.165	8.186	-42.979
17B	62.66	74.73	646.93	-51.165	8.278	-42.887
18A	62.35	87.99	666.59	-49.489	8.791	-40.698
18B	62.27	87.90	666.57	-49.489	8.858	-40.631
19A	62.17	99.91	680.03	-47.818	9.195	-38.623
19B	62.14	99.88	679.92	-47.818	9.262	-38.556
20A, 20B	62.35	90.05	679.69	-43.394	9.564	-33.830
21A, 21B	59.78	99.28	680.19	-51.445	9.901	-41.544
22A	61.78	100.36	655.56	-59.057	10.220	-48.837
22B, 22C	62.10	100.14	655.11	-57.093	11.574	-45.519
23A, 23B	62.01	100.30	631.77	-67.742	11.868	-55.874
24A, 24B	60.49	100.33	632.23	-70.294	12.011	-58.283
25A	63.76	100.07	632.20	-63.512	12.187	-51.325

Step	Power (%)	Primary Flow (%)	Core Inlet Temperature (°F)	Reactivity Change (cents) from Step 2B		
				Change due to Rod Movement	Change due to Burnup	Total Change
25B, 25C	63.77	100.36	632.24	-63.585	12.280	-51.305
26A, 26B	64.37	89.87	631.98	-58.184	12.591	-45.593
27A, 27B	63.59	99.91	680.69	-40.651	13.137	-27.514
28A, 28B	64.43	92.17	660.62	-45.316	13.583	-31.733
29A	65.09	83.58	637.48	-50.591	13.978	-36.613
29B	64.96	83.57	637.59	-50.591	14.070	-36.521
30A, 30B	66.23	77.27	614.56	-54.797	14.499	-40.298
31A, 31B	64.42	66.51	615.07	-49.197	14.726	-34.471
32A, 32B	63.88	75.27	615.22	-57.618	15.096	-42.522
33A, 33B	59.48	66.36	614.81	-60.737	15.323	-45.414
34A, 34B	64.27	74.66	630.27	-48.641	15.685	-32.956
35A, 35B	64.37	88.34	651.16	-46.737	16.214	-30.523
36A, 36B	64.06	100.00	663.73	-45.632	16.677	-28.955
37A, 37B	64.45	90.52	663.95	-40.694	17.030	-23.664
38A, 38B	58.67	99.69	663.95	-54.831	17.332	-37.499
39A	63.81	100.35	614.29	-67.046	18.139	-48.907
39B	64.18	100.45	614.39	-65.015	19.350	-45.665
40A	64.66	75.46	632.40	-42.807	19.871	-22.936
40B	64.56	75.33	632.29	-42.807	20.107	-22.700
41A	64.42	84.86	632.65	-48.619	20.603	-28.016
41B	64.46	84.83	632.53	-48.619	20.687	-27.932
42A	67.24	84.89	632.51	-42.807	21.048	-21.759
42B	67.25	84.96	632.43	-42.807	21.191	-21.616
43A	64.62	67.19	632.12	-35.187	21.679	-13.508
43B, 43C	63.96	67.26	631.62	-35.477	24.133	-11.344
44A, 44B	64.27	67.47	656.61	-22.580	24.613	2.033
45A	63.76	66.91	679.91	-11.664	24.949	13.285
45B, 45C	64.32	66.95	680.42	-9.787	25.142	15.355
46A	80.22	83.66	680.19	9.920	26.756	36.676
46B	80.04	83.58	679.98	9.570	26.992	36.562
47A	96.35	100.74	680.06	26.966	29.169	56.135
47B	95.52	99.92	679.44	26.461	29.749	56.210
47C	95.54	100.08	679.39	26.461	29.976	56.437
48A	87.50	100.30	660.25	5.532	30.817	36.349
48B	87.32	100.26	660.16	5.532	31.002	36.534
49A	87.55	94.79	680.82	19.968	31.767	51.735

Step	Power (%)	Primary Flow (%)	Core Inlet Temperature (°F)	Reactivity Change (cents) from Step 2B		
				Change due to Rod Movement	Change due to Burnup	Total Change
49B	87.64	94.88	680.76	19.968	31.901	51.869
50A	87.43	100.30	680.68	16.678	32.406	49.084
50B	87.39	100.39	680.61	16.678	32.591	49.269
51A	95.30	100.31	680.80	30.190	33.625	63.815
52A	59.49	101.10	659.72	-39.090	35.264	-3.826
52B, 52C	59.29	100.11	660.44	-35.489	36.836	1.347
53A	54.54	100.25	660.10	-44.729	37.004	-7.725
53B	54.33	100.14	659.91	-44.729	37.324	-7.405
54A, 54B	59.74	89.62	660.58	-29.703	37.820	8.117
55A, 55B	58.97	99.21	629.50	-48.696	38.316	-10.380
56A	59.66	100.67	660.48	-32.999	38.660	5.661
56B. 56C	59.75	100.72	660.52	-32.944	38.761	5.817
57A	53.98	90.53	660.53	-40.879	39.173	-1.706
57B	53.97	90.51	660.50	-40.879	39.241	-1.638
58A	49.61	83.22	660.80	-47.280	39.568	-7.712
58B	49.56	83.16	660.79	-47.280	39.602	-7.678
59A	44.78	74.97	660.74	-54.612	39.762	-14.850
59B	44.75	74.97	660.69	-54.612	39.896	-14.716
60A	40.33	67.10	660.51	-62.027	40.022	-22.005
60B, 60C	40.38	67.05	660.55	-61.918	40.392	-21.526
61A	40.20	74.70	660.44	-65.555	40.476	-25.079
61B	40.16	74.62	660.38	-65.555	40.502	-25.053
62A	35.48	66.98	660.12	-74.894	40.560	-34.334
62B	35.49	67.01	660.18	-74.894	40.577	-34.317
63A, 63B	40.51	67.04	644.78	-68.935	40.670	-28.265
64A	40.29	67.20	629.42	-77.177	40.745	-36.432
64B, 64C	40.54	67.04	629.74	-75.632	40.829	-34.803
65A	40.08	75.11	629.57	-80.153	40.897	-39.256
65B	39.99	75.15	629.40	-80.153	40.964	-39.189
66A	35.71	66.53	629.59	-87.852	41.098	-46.754
66B	35.68	66.46	629.66	-87.852	41.124	-46.728
67A	40.37	74.59	639.20	-73.665	41.267	-32.398
67B	40.39	74.69	639.26	-73.665	41.325	-32.340
68A	40.09	88.32	652.11	-71.985	41.502	-30.483
68B	39.98	88.13	652.15	-71.985	41.519	-30.466
69A	39.68	99.50	660.17	-70.868	41.645	-29.223

Step	Power (%)	Primary Flow (%)	Core Inlet Temperature (°F)	Reactivity Change (cents) from Step 2B		
				Change due to Rod Movement	Change due to Burnup	Total Change
69B	39.75	99.69	660.27	-70.850	41.763	-29.087
70A, 70B	39.99	89.87	660.69	-68.068	41.914	-26.154
71A	35.35	100.04	660.17	-80.991	42.040	-38.951
71B	35.05	99.82	660.36	-80.991	42.519	-38.472
72A	39.66	99.45	629.84	-84.123	42.687	-41.436
72B, 72C	39.58	99.81	629.53	-84.379	42.788	-41.591
73A	34.79	100.31	629.49	-95.715	42.839	-52.876
73B	34.72	100.27	629.49	-95.715	42.889	-52.826
74A	39.62	100.05	629.58	-83.817	43.057	-40.760
74B, 74C	39.86	100.09	629.83	-82.983	43.099	-39.884
75A	40.10	90.53	629.93	-80.708	43.259	-37.449
75B	40.04	90.34	629.85	-80.708	43.301	-37.407
76A	40.02	100.32	660.19	-68.623	43.528	-25.095
76B	40.10	100.39	660.23	-68.623	43.612	-25.011
77A	40.39	89.79	645.37	-72.807	43.873	-28.934
77B	40.38	89.76	645.41	-72.807	43.990	-28.817
78A	41.25	78.81	623.87	-77.591	44.285	-33.306
78B	41.23	78.83	623.92	-77.591	44.301	-33.290
79A, 79B	42.14	69.44	598.74	-83.268	44.570	-38.698
80A	40.29	66.84	595.26	-88.701	44.663	-44.038
80B, 80C	40.08	66.70	595.04	-88.948	44.781	-44.167
81A, 81B	39.88	75.38	594.97	-93.200	44.890	-48.310
82A	35.23	66.41	595.32	-102.068	45.024	-57.044
82B	35.10	66.31	595.38	-102.068	45.268	-56.800
83A	40.07	75.01	604.76	-87.255	45.495	-41.760
83B	40.09	75.00	604.74	-87.255	45.520	-41.735
84A	39.68	88.08	617.15	-85.847	45.747	-40.100
84B	39.75	88.32	617.26	-85.847	45.773	-40.074
85A	39.36	99.36	625.64	-84.444	45.941	-38.503
85B	39.47	100.66	625.62	-84.444	46.042	-38.402
86A	39.55	100.01	594.65	-98.625	46.243	-52.382
86B, 86C	39.44	100.11	594.48	-97.776	46.630	-51.146
87A	40.30	75.44	630.38	-72.542	47.017	-25.525
87B	40.34	75.52	630.52	-72.542	47.135	-25.407
88A	39.90	84.51	630.38	-76.442	47.370	-29.072
88B	39.97	84.68	630.43	-76.442	47.395	-29.047

Step	Power (%)	Primary Flow (%)	Core Inlet Temperature (°F)	Reactivity Change (cents) from Step 2B		
				Change due to Rod Movement	Change due to Burnup	Total Change
89A	41.52	84.46	630.06	-72.542	47.479	-25.063
89B	41.62	84.66	630.05	-72.542	47.504	-25.038
90A	40.29	67.19	629.96	-68.950	47.731	-21.219
90B, 90C	40.31	67.32	630.03	-69.313	47.832	-21.481
91A, 91B	40.14	66.73	645.62	-61.668	48.034	-13.634
92A	40.21	66.71	660.47	-54.683	48.253	-6.430
92B, 92C	40.31	66.91	660.17	-54.654	48.396	-6.258
93A, 93B	49.55	83.18	660.21	-38.236	49.203	10.967
94A	59.36	100.22	660.32	-23.160	50.085	26.925
94B, 94C	59.20	100.02	660.50	-22.111	50.548	28.437
95A	59.12	99.91	630.26	-36.097	50.943	14.846
95B	59.17	99.91	630.27	-35.531	51.287	15.756
96A, 96B	59.61	90.82	659.65	-16.908	51.851	34.943
97A	54.68	99.48	659.44	-30.176	52.448	22.272
97B	54.60	99.48	659.41	-30.176	52.565	22.389
98A	59.36	100.46	659.89	-20.186	52.969	32.783
99A	35.44	99.73	648.11	-76.990	53.406	-23.584
99B, 99C	35.58	99.88	648.02	-73.950	55.062	-18.888
100A, 100B	30.93	99.64	647.95	-85.001	55.222	-29.779
101A, 101B	35.74	90.58	648.35	-71.430	55.407	-16.023
102A, 102B	35.29	98.36	630.70	-82.150	55.600	-26.550
103A	35.52	99.81	648.19	-73.389	55.777	-17.612
103B, 103C	35.43	100.07	648.30	-73.480	56.046	-17.434
104A, 104B	32.32	90.31	647.90	-79.896	56.163	-23.733
105A	29.36	82.27	648.25	-85.823	56.214	-29.609
105B	29.41	82.38	648.29	-85.823	56.264	-29.559
106A, 106B	26.93	75.04	648.50	-91.232	56.332	-34.900
107A	24.28	67.23	648.58	-96.966	56.390	-40.576
107B, 107C	24.20	67.26	647.67	-98.139	56.592	-41.547
108A, 108B	24.03	75.64	647.99	-95.998	56.626	-39.372
109A	19.05	66.94	648.31	-113.491	56.643	-56.848
109B	19.00	66.71	648.26	-113.491	56.643	-56.848
110A, 110B	23.97	67.15	638.88	-98.822	56.676	-42.146
111A	24.10	67.02	630.07	-106.911	56.727	-50.184
111B, 111C	24.03	66.83	630.03	-106.768	56.794	-49.974
112A	23.77	75.33	629.79	-109.022	56.844	-52.178

Step	Power (%)	Primary Flow (%)	Core Inlet Temperature (°F)	Reactivity Change (cents) from Step 2B		
				Change due to Rod Movement	Change due to Burnup	Total Change
112B	23.80	75.53	629.82	-109.022	56.861	-52.161
113A	19.19	66.67	629.80	-121.558	56.920	-64.638
113B	19.21	66.80	629.87	-121.558	56.920	-64.638
114A	24.08	75.13	635.94	-104.803	56.979	-47.824
114B	24.28	75.43	635.18	-104.803	57.029	-47.774
115A	23.78	86.93	642.49	-103.963	57.105	-46.858
115B	23.76	86.80	642.44	-103.963	57.122	-46.841
116A	23.42	99.04	647.92	-103.125	57.214	-45.911
116B	23.27	98.87	647.81	-103.496	57.282	-46.214
117A	23.64	90.40	647.95	-101.824	57.349	-44.475
117B	23.68	90.60	647.95	-101.824	57.366	-44.458
118A	18.66	98.73	647.83	-117.054	57.416	-59.638
118B	18.59	99.80	647.74	-117.054	57.441	-59.613
119A	23.43	100.52	630.00	-111.651	57.500	-54.151
119B, 119C	23.50	99.92	629.85	-110.964	57.517	-53.447
119D, 119E	23.69	100.41	629.75	-110.964	57.651	-53.313
120A	18.85	99.77	630.23	-124.910	57.719	-67.191
120B	18.82	99.48	630.19	-124.910	57.719	-67.191
121A	23.31	101.38	629.85	-112.092	57.794	-54.298
121B, 121C	23.37	99.70	629.82	-111.431	57.929	-53.502
122A	23.57	90.03	629.98	-110.012	58.021	-51.991
122B	23.58	90.12	630.07	-110.012	58.089	-51.923
123A	23.73	100.16	648.44	-101.844	58.173	-43.671
123B	23.79	100.22	648.44	-101.844	58.189	-43.655
124A	24.15	89.32	638.23	-104.647	58.324	-46.323
124B	24.10	89.03	638.19	-104.647	58.374	-46.273
125A	24.53	77.64	624.96	-108.312	58.492	-49.820
125B	24.53	77.54	624.85	-108.312	58.517	-49.795
126A	25.19	67.21	607.67	-112.854	58.635	-54.219
126B	25.13	67.13	607.64	-112.854	58.694	-54.160
127A	24.31	67.79	585.22	-126.342	58.887	-67.455
127B, 127C	23.87	66.83	584.96	-127.331	59.055	-68.276
128A	23.76	75.17	584.88	-129.031	59.173	-69.858
128B	23.78	75.31	584.79	-129.031	59.232	-69.799
129A	19.22	66.92	584.52	-142.193	59.266	-82.927
129B	19.20	66.88	584.50	-142.193	59.282	-82.911

Step	Power (%)	Primary Flow (%)	Core Inlet Temperature (°F)	Reactivity Change (cents) from Step 2B		
				Change due to Rod Movement	Change due to Burnup	Total Change
130A	23.91	75.51	590.96	-125.332	59.400	-65.932
130B	23.99	75.97	591.18	-125.332	59.467	-65.865
131A 131B	23.86	88.11	597.70	-123.924	59.560	-64.364
132A	23.52	100.38	602.48	-123.361	59.686	-63.675
132B	23.48	100.53	602.57	-123.361	59.762	-63.599
133A	23.55	90.55	602.73	-122.238	59.846	-62.392
133B	23.48	90.27	602.61	-122.238	59.989	-62.249
134A, 134B	18.45	99.61	602.52	-138.145	60.106	-78.039
135A	23.31	100.90	584.58	-132.138	60.182	-71.956
135B	23.40	100.49	584.54	-130.917	60.216	-70.701
13SC	23.57	101.02	584.65	-130.917	60.636	-70.281
136A	23.58	102.03	630.49	-109.262	60.846	-48.416
136B, 136C	23.33	100.31	630.08	-109.643	61.140	-48.503
137A	23.87	75.36	630.36	-105.067	61.292	-43.775
137B	23.84	75.25	630.35	-105.067	61.334	-43.733
138A	23.76	85.27	630.68	-106.494	61.451	-45.043
138B	23.73	85.21	630.76	-106.494	61.485	-45.009
139A, 139B	24.29	85.72	630.45	-105.067	61.619	-43.448
140A	24.25	67.26	630.25	-102.220	61.737	-40.483
140B, 140C	24.57	67.33	630.37	-101.360	61.846	-39.514
141A	24.61	67.11	639.70	-96.512	61.947	-34.565
141B	24.64	67.12	639.75	-96.512	62.141	-34.371
142A	24.46	66.93	648.43	-92.545	62.225	-30.320
142B, 142C	24.43	67.00	648.37	-92.779	62.393	-30.386
143A, 143B	30.29	83.52	648.43	-78.801	62.746	-16.055
144A	35.91	100.40	648.41	-66.795	63.065	-3.730
144B, 144C	35.70	100.13	647.94	-66.911	63.444	-3.467
145A, 145B	35.47	99.51	629.60	-75.651	63.763	-11.888
146A	35.98	90.19	647.36	-64.122	64.133	0.011
146B	35.97	90.20	647.39	-64.122	64.175	0.053
147A, 147B	30.66	99.91	646.93	-79.067	64.436	-14.631
148A	35.51	100.16	647.40	-66.352	64.621	-1.731
149A, 149B	21.83	100.40	640.99	-104.067	65.899	-38.168
150A, 150B	16.98	99.57	640.71	-118.582	65.966	-52.616
151A	21.98	90.79	641.21	-102.381	66.083	-36.298
151B	21.99	90.89	641.23	-102.381	66.100	-36.281

Step	Power (%)	Primary Flow (%)	Core Inlet Temperature (°F)	Reactivity Change (cents) from Step 2B		
				Change due to Rod Movement	Change due to Burnup	Total Change
152A, 152B	21.73	100.51	619.86	-113.998	66.243	-47.755
153A	21.86	100.40	641.38	-102.943	66.378	-36.565
153B, 153C	21.66	100.47	641.30	-103.786	66.445	-37.341
154A, 154B	20.46	94.78	641.21	-106.889	66.529	-40.360
155A	18.13	83.17	641.25	-113.141	66.613	-46.528
155B	18.12	83.12	641.23	-113.141	66.638	-46.503
156A	16.48	74.54	641.28	-117.721	66.672	-51.049
156B	16.48	74.64	641.31	-117.721	66.697	-51.024
157A	14.85	66.79	641.36	-122.322	66.731	-55.591
157B, 157C	15.00	66.79	641.42	-122.133	66.815	-55.318
158A	14.91	74.88	641.54	-123.260	66.857	-56.403
158B	14.69	74.82	641.32	-124.171	66.882	-57.289
159A	10.13	66.81	641.67	-139.859	66.899	-72.960
159B	10.12	66.84	641.62	-139.859	66.891	-72.968
160A, 160B	14.99	66.84	635.91	-124.171	66.924	-57.247
161A	15.07	67.02	630.26	-127.849	66.941	-60.908
161B, 161C	14.81	67.08	630.04	-127.873	66.991	-60.882
162A	14.66	74.94	629.93	-129.282	67.042	-62.240
162B	14.60	74.93	629.93	-129.282	67.059	-62.223
163A	10.00	67.10	630.04	-145.839	67.067	-78.772
163B	9.97	67.13	630.07	-145.839	67.059	-78.780
164A	14.69	74.80	633.87	-127.029	67.101	-59.928
164B	14.70	74.74	633.89	-127.029	67.109	-59.920
165A	14.45	87.36	637.76	-127.029	67.176	-59.853
165B	14.51	87.36	637.75	-127.029	67.176	-59.853
166A	14.13	99.50	640.99	-126.748	67.227	-59.521
166B	14.14	99.58	641.03	-126.748	67.235	-59.513
167A, 167B	14.38	90.49	641.39	-125.345	67.286	-58.059
168A, 168B	9.40	100.72	641.15	-143.537	67.302	-76.235
169A	14.23	100.25	630.32	-131.260	67.328	-63.932
169B, 169C	14.13	99.96	630.20	-131.592	67.345	-64.247
170A	9.43	98.97	630.51	-148.461	67.353	-81.108
170B	9.43	98.93	630.50	-148.461	67.353	-81.108
171A	14.56	101.15	630.49	-129.898	67.387	-62.511
171B, 171C	14.61	101.25	630.52	-129.774	67.403	-62.371
172A	14.62	90.51	630.47	-129.490	67.471	-62.019

Step	Power (%)	Primary Flow (%)	Core Inlet Temperature (°F)	Reactivity Change (cents) from Step 2B		
				Change due to Rod Movement	Change due to Burnup	Total Change
172B	14.58	90.35	630.51	-129.490	67.487	-62.003
173A	14.57	99.92	641.20	-124.674	67.580	-57.094
173B	14.51	99.81	641.21	-124.674	67.597	-57.077
174A	15.01	91.05	635.28	-126.086	67.664	-58.422
174B	15.05	90.86	635.28	-125.804	67.689	-58.115
175A	15.39	78.09	626.41	-128.087	67.756	-60.331
175B	15.36	78.14	626.50	-128.087	67.857	-60.230
176A	15.72	66.99	615.63	-130.929	67.925	-63.004
176B	15.71	66.88	615.57	-130.929	67.941	-62.988
177A	14.69	66.80	576.89	-153.677	68.017	-85.660
177B, 177C	14.67	66.57	576.82	-153.590	68.034	-85.556
178A, 178B	14.64	74.99	576.72	-154.441	68.084	-86.357
179A	9.99	66.87	576.79	-171.642	68.110	-103.532
179B	9.93	66.74	576.80	-171.642	68.110	-103.532
180A	14.63	75.01	580.72	-151.892	68.168	-83.724
180B	14.67	75.14	580.80	-151.892	68.185	-83.707
181A, 181B	14.36	87.65	585.05	-151.610	68.261	-83.349
182A, 182B	14.18	99.66	588.18	-151.327	68.337	-82.990
183A	14.21	90.75	588.06	-150.485	68.555	-81.930
183B	14.21	90.85	588.06	-150.485	68.589	-81.896
184A	9.50	98.53	588.26	-167.607	68.639	-98.968
184B	9.46	100.98	588.40	-167.607	68.656	-98.951
185A	14.11	100.09	577.11	-152.516	68.706	-83.810
185B, 185C	14.34	99.76	577.27	-154.922	68.883	-86.039
186A	14.66	101.11	630.40	-127.471	68.975	-58.496
186B, 186C	14.51	99.02	630.11	-128.795	69.009	-59.786
187A, 187B	14.84	75.46	630.10	-126.209	69.118	-57.091
188A	14.62	84.55	630.09	-127.645	69.186	-58.459
188B	14.65	84.64	630.12	-127.645	69.219	-58.426
189A	14.86	85.17	630.28	-126.783	69.270	-57.513
189B	14.84	85.12	630.31	-126.783	69.413	-57.370
190A	14.81	66.75	630.04	-125.348	69.488	-55.860
190B, 190C	14.93	67.40	630.12	-125.062	69.648	-55.414
191A, 191B	14.83	67.22	636.17	-122.199	69.698	-52.501
192A	14.80	66.99	641.08	-119.917	69.757	-50.160
192B, 192C	14.78	67.18	640.82	-120.287	69.816	-50.471

Step	Power (%)	Primary Flow (%)	Core Inlet Temperature (°F)	Reactivity Change (cents) from Step 2B		
				Change due to Rod Movement	Change due to Burnup	Total Change
193A, 193B	18.01	82.86	640.55	-111.120	69.993	-41.127
194A	21.39	99.58	640.76	-101.505	70.203	-31.302
194B, 194C	21.38	99.56	640.58	-101.409	70.304	-31.105
195A, 195B	21.16	99.05	619.87	-112.184	70.430	-41.754
196A, 196B	21.74	90.69	640.83	-99.445	70.606	-28.839
197A	16.80	98.46	640.49	-115.046	70.741	-44.305
197B	16.83	98.25	640.42	-115.046	70.749	-44.297
198A	21.33	100.55	640.56	-101.128	70.867	-30.261

Nuclear Science and Engineering Division
Argonne National Laboratory
9700 South Cass Avenue
Lemont, IL 60439-4842

www.anl.gov

Argonne National Laboratory is a U.S. Department of Energy laboratory managed by UChicago Argonne, LLC